Understanding Nanoscale Magnetization Reversal and Spin Dynamics by Using Advanced Transmission Electron Microscopy

A Dissertation Presented
by

Lei Huang

to
The Graduate School
in Partial Fulfillment of the Requirements
for the Degree of
Doctor of Philosophy
in
Physics

Stony Brook University
August 2010

Stony Brook University

The Graduate School

Lei Huang

We, the dissertation committee for the above candidate for the Doctor of Philosophy degree, hereby recommend acceptance of this dissertation.

Yimei Zhu – Dissertation Advisor
Senior Physicist, CMPMSD, Brookhaven National Laboratory
Adjunct Professor, Department of Physics and Astronomy

Thomas C. Weinacht - Chairperson of Defense
Associate Professor, Department of Physics and Astronomy

Thomas T. S. Kuo
Professor, Department of Physics and Astronomy

Miriam H. Rafailovich - Outside Member
Distinguished Professor, Department of Materials Science and Engineering

Dario A. Arena - Outside Member
Associate Physicist, NSLS, Brookhaven National Laboratory

This dissertation is accepted by the Graduate School.

Lawrence Martin
Dean of the Graduate School

Abstract of the Dissertation

Understanding Nanoscale Magnetization Reversal and Spin Dynamics by Using Advanced Transmission Electron Microscopy

by

Lei Huang

Doctor of Philosophy

in

Physics

Stony Brook University

2010

In the forefront of spintronics research, transmission electron microscopy (TEM) is not only an essential tool for examining matter with high spatial resolution, but also associated with it is a rich variety of *in-situ* capabilities making quantitative investigation of the intriguing microscopic magnetic phenomena possible. This dissertation covers TEM studies of nanoscale magnetization reversal and high frequency spin dynamics of patterned magnetic elements, which hold great promise for the development of next generation recording/memory technologies.

We first focus on the static spin configurations and magnetization reversal processes of patterned soft magnetic thin films. Using *in-situ* Lorentz microscopy and off-axis electron holography, we find patterning the same magnetic material with different geometries can create sharply distinct domain structures and switching properties, which can be effectively explained by shape anisotropy and interlayer stray field coupling. We then exploit these effects by designing shape-engineered trilayer nanomagnets, of which the magnetization reversal process can be precisely controlled to achieve specific remanent states.

We also study the magnetic behavior of nanomagnets in the high frequency regime, where spin torque transfer between current and magnetization represents a radically new data-writing concept. Here, we design and construct a novel TEM stage to apply microwave excitation stimulus to the patterned nanomagets, and directly observe the current-induced resonant precession of the vortex core with unprecedented spatial resolution. We measure the precession orbits as a function of both frequency and current density, and succeed in quantifying the resonant frequency and damping coefficient. For the first time we obtain experimental proof with nanometer resolution that the vortex precession orbit is elliptical when it's off-resonance.

TABLE OF CONTENTS

List of Figures

List of Tables

Acknowledgements

I would like to thank my advisor, Prof. Yimei Zhu, for his generous support which enabled me to finish my research projects at Brookhaven National Lab. Yimei not only tried very hard to find the funds to buy us so many cool instruments, but more importantly, he undertook a lot of outside pressure so that the rest of us could concentrate on science itself. Over the years, I have been deeply impressed and inspired by his dedication to work, genuine passion for science, and attentiveness to others. In all sincerity, working for Yimei has been a privilege and real pleasure.

I would like to thank Dr. June W. Lau. She gave me wonderful initial training during the early days of my graduate studies. Even after she took position in NIST, she continued helping me in many ways. June informed me of important learning opportunities, introduced me to other professors and researchers during conferences, and called up from time to time to make sure I was happy and doing ok. More than a senior student, June has become an elder sister and dear friend to me.

I thank Dr. Marvin A. Schofield, Dr. Steve Volkov, Dr. Marco Beleggia, Dr. Jiaqing He, Dr. Lijun Wu, Dr. Lihua Zhang, Dr. Jincheng Zheng, Dr. Tobias Beetz, Dr. Robert Klie, Dr. Mirko Milas, Dr. Petr Oleynikov, Dr. Jing Tao, Dr. Dong Su, Dr. M-G. Han, Dr. Feng Wang, Dr. James Ciston, Kim Kissinger, Dr. Chao Ma and Prof. Qingping Meng for sharing with me their extensive knowledge and keen insights on microscopy, magnetism, and other random topics. I thank Dr. Anthony T. Bollinger, Dr. Aaron Stein, and Dr. Fernando Camino, for their help on sample bonding and clean room training. I thank Shawn Pollard for proof-reading this dissertation and wish him all the best for his graduate adventures.

Last but not least, I want to thank my Mom, Dad, and Ying, for their trust, encouragement, and unconditional love.

Publications

1. J. W. Lau, P. Morrow, J. C. Read, V. Hoink, W. F. Egelhoff, L. Huang, and Y. Zhu, *Appl. Phys. Lett.,* **96**, 262508, (2010)
2. L. Huang, M. A. Schofield, and Y. Zhu, *Adv. Mater.,* **22**, 492, (2010)
3. L. Huang and Y. Zhu, *Appl. Phys. Lett.,* **95**, 222502, (2009)
4. L. Huang, M. A. Schofield, and Y. Zhu, *Appl. Phys. Lett.*, **95**, 042501, (2009)
5. H. Zhong, L. Huang, D. Wei, S. Wang, Y. Zhu, and J. Yuan, *J. Mag. Mag. Mater.*, **321**, L37-L40, (2009)
6. J. E. Villegas, K. D. Smith, L. Huang, Y. Zhu, R. Morales, and I. K. Schuller, *Phys. Rev. B*, **77**, 134510, (2008)

Chapter 1. Introduction

1.1 The Context of Present Work

As one of the most exciting and rapidly developing areas in condensed matter physics, magnetism has provided astonishing scientific discoveries combined with vast technological benefits. Recent years have seen considerable advances of magneto-electronics and spintronics, fields in which magnetism and solid state electronics merged together to exploit spin dependent transport phenomena [1-3]. These created novel electronic functionalities that in part already have entered the market, for example in hard disk read heads and non-volatile magnetic random access memories (MRAMs). Meanwhile, the continuing increase of areal density of magnetic storage devices (as described by Moore's empirical law, Figure 1.1) has stimulated intense research interest in patterned media, in which the magnetic layer is created as an ordered array of highly uniform islands [Figure 1.2]. Being a single domain particle, each isolated island is capable of storing an individual bit of information. During data writing, the islands must switch as coherent units and not break up into multiple domains [4]. How to design and optimize the system so that all trillions of nanosized islands can function properly in a well-controlled fashion is still a longstanding challenge.

The spin configuration (or domain structure) of any magnet is fundamentally determined by the interplay and competition among multiple energy contributions: the exchange energy of interaction among atomic moments, the magnetostatic energy between the moments and the magnetic field itself, and the magnetocrystalline anisotropy energy. The exchange interaction is what causes magnetic ordering in the first place. It is of quantum mechanical origin, and is commonly described by the Heisenberg interaction of $-\sum J_{ij} S_i S_j$, a sum of interactions with strength J_{ij} between neighboring moments S on sites i and j. The minus sign ensures that when $J_{ij} < 0$, the lowest energy state corresponds to ferromagnetic ordering, with all the moments aligned in the same direction. The magnetostatic energy is associated with the demagnetizing fields generated by any magnetized body and is proportional to the squared field integrated over all space. The magnetocrystalline energy originates from spin-orbital coupling, which describes the interaction between atomic moments and the local crystal fields. In hard magnetic materials, such as magnetite and high-carbon steel, the strong magnetocrystalline anisotropy energy overwhelms all the other energy terms. In contrast, for soft magnetic materials, such as nickel, cobalt, and nickel-iron alloys known as Permalloy (Py), the magnetocrystalline anisotropy is much weaker. The interplay between exchange energy and the magnetostatic energy thus makes a dominant influence in such systems.

Recently, scientists discovered that the soft magnetic materials demonstrate promising technological potentials when they are patterned with well defined shapes in the submicron size range [5]. For such patterned nanomagnets, their magnetic properties are extrinsic rather than intrinsic to the materials themselves, due to two reasons.

First is the “size effect”. The phenomena governing physical properties of materials are characterized by length-scales, for example, the wavelength of light for optics, or the electron mean free path for transport process. A size effect is manifest when the physical dimensions of an object are smaller or comparable to these defining length scales. For ferromagnetism, the exchange and magnetostatic energies in submicron meter regime are of very similar magnitude, so small variations in size can significantly shift the delicate balance between exchange energy, which favors parallel alignment of the magnetic moments, and the magnetostatic energy, which favors domain division and magnetic flux closure structures with minimal stray field. Emerging properties can thus be obtained by simply controlling object size. For example, in very small particles, one often finds a single domain state where the magnetization is homogeneously oriented along one direction, creating a sizable magnetic stray field outside the particle. In larger particles, the stray field increases up to the point where the total energy of the system may be reduced at the expense of the exchange energy by the spontaneous formation of domains, domain walls, and non-collinear magnetization distributions.

Second, the shape of the elements can strongly influence spin configurations due to demagnetization effect. The influence of shape can be quantified by an additional anisotropy term (so-called configurational anisotropy) along the symmetric axis of the geometric shape. This is quite different compared with the magnetocrystalline anisotropy in conventional magnetic material, which arises from spin-orbital coupling. Magnetocrystalline anisotropy is intrinsic to the particular element or alloy and cannot be easily tailored. Configurational anisotropy, on the other hand, is an extrinsic property and thus provides an important means of designing new nanostructured magnetic materials where the magnetic properties can be controllably engineered with high precision [6].

In order to fully understand these various effects, it is crucial to observe phenomena at the same length scale – hence the need for local characterization techniques. The current boom of nanomagnetism was made possible by the remarkable progress in three different but interconnected disciplines: nanofabrication, characterization and computation. The exponential shrinking in size of the integrated circuit transistor has lead to enormous investment in development of advanced nanofabrication techniques, such as optical and electron beam lithography. As a result, patterned devices with feature size of tens of nanometers can nowadays be readily produced with very high quality on a routine basis. On another hand, the mathematical equations governing magnetic behavior on the nanometer scale are highly nonlinear and can generally only be studied theoretically using computer-intensive numerical algorithms. The recent availability of low-cost, high-speed processors has now enabled nanomagnetism to become a widely studied branch of condensed matter theory. Compared with these two areas, the magnetic characterization techniques was relatively underdeveloped [7-8]. Although conventional techniques such as Scanning Quantum Interference Devices (SQUIDs) and Vibrating Sample Magnetometers (VSM) do provide very accurate quantitative information in the magnetic behavior of a specimen, they have in common the problem that a rather big volume of the material has to be investigated in order to collect detectable signals. For patterned nanomagnets, this involves using a large ensemble of nominally identical elements. The macroscopic measurement techniques therefore can only yield a weighted average over all the various single element behaviors.

In this regard, the modern transmission electron microscope (TEM) is an instrument of choice for the characterization of magnetic materials and spin configurations at nanoscale [9]. Compared with other characterization techniques, TEM-based approach is unique in numerous perspectives. First of all, TEM stands out in its spatial resolution among all the microscopy tools known to exist. Under specific operational modes, such as Lorentz microscopy and electron holography, it can be used to directly reveal magnetic microstructures in real space. Second, due to the transmission nature of TEM technique, the recorded electron micrograph contains information across the entire sample thickness. This is important because most of the widely adopted domain imaging techniques, such as Magnetic Force Microscopy (MFM), Scanning Electron Microscopy with Polarization Analyzer (SEMPA), and Kerr Microscopy, can only access surface domains, which in many cases are quite different from domains inside the sample region. Third, in addition to the high intrinsic spatial resolution, TEM offers a number of signals which can be exploited to obtain chemical and structural information from a very local area of the specimen. Last but not least, with the help of specially designed sample holders, the magnetic nanostructures can be subjected to a wide range of external excitations, and their physical responses can be quantitatively investigated in controlled circumstances [10]. Up until now, scientists have succeeded in changing the temperature, stain, magnetic field, and electrical bias applied to the sample region. Armed with all these capabilities, the TEM is no longer a single-purpose imaging tool, but rather a full-fledged research platform where structure-property correlations can now be studied *in-situ* and in real time, at the near atomic scale.

All the various aspects discussed so far contribute to the context of the present dissertation: the understanding, using TEM-based magnetic imaging methods, of the magnetization mechanisms leading to the controlled manipulation of spin degree of freedom in magnetic nanoelements.

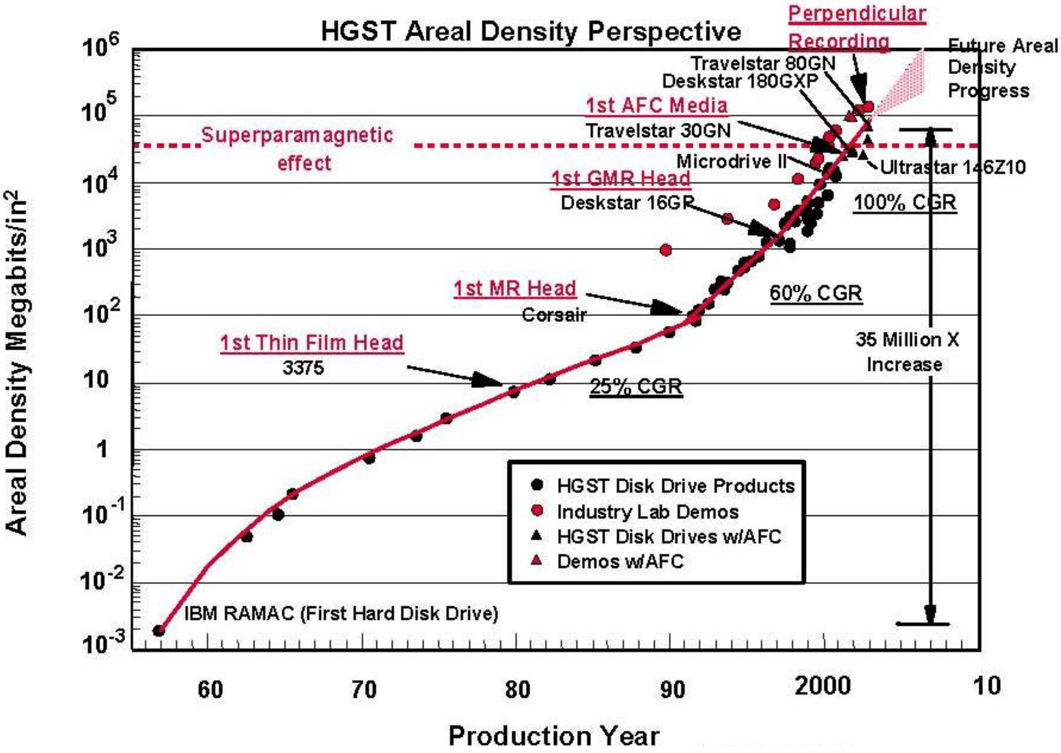

Figure 1.1 Areal density of magnetic hard disk drives as a function of the year of shipment (Hitachi Global Storage Technologies).
CGR stands for Compounded Growth Rate.

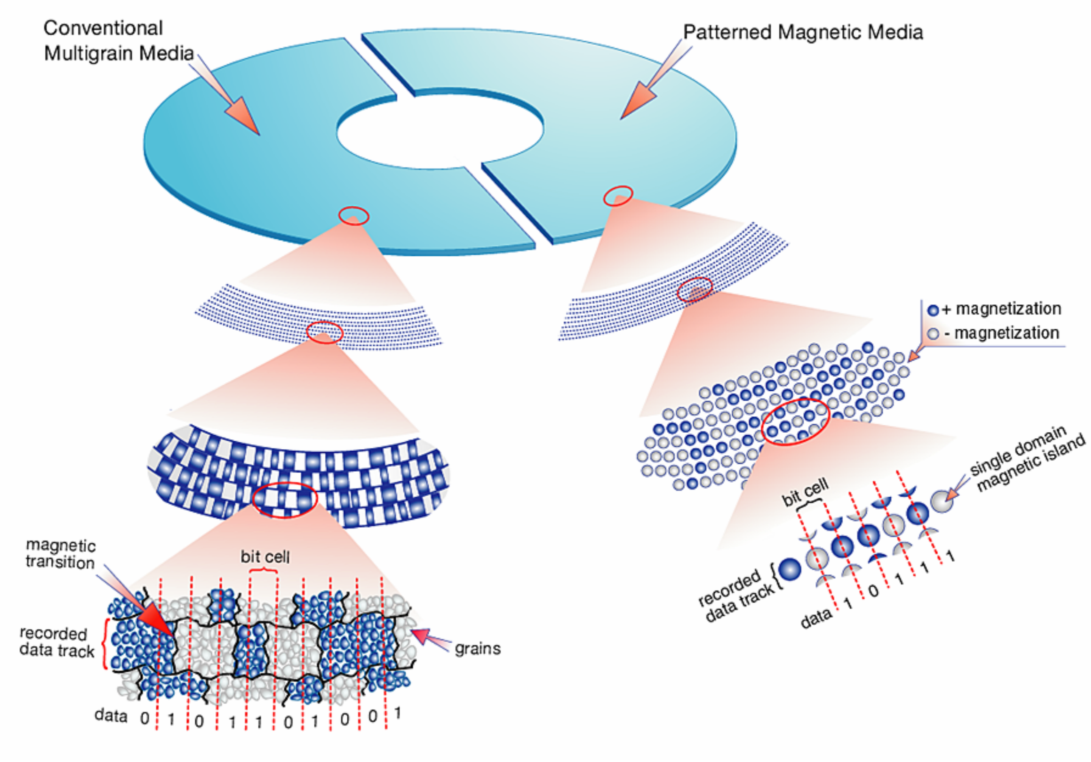

Figure 1.2 Conventional media vs. bit patterned media (Hitachi Global Storage Technologies)

1.2 Outline of this Dissertation

This dissertation is structured as follows.

Chapter 2 introduces the device fabrication process (including thin film growth and electron beam lithography procedures), magnetic imaging basics using TEM (including fundamentals of Lorentz microscopy and off-axis electron holography, and Brookhaven's TEM instrumentation), and theories and algorithms concerning micromagnetic modeling. These different aspects constitute the basic ingredients underlying all the research work covered in this dissertation.

Chapter 3 presents the Lorentz microscopy studies of three different types of Py geometries: thin film, discrete disk, and disk/film coupled structure. We show that although being the same material, the spin configurations and reversal characteristics can be significantly modified by simply changing the geometry of the structure. The observed domain configurations are well reproduced by micromagnetic simulations, and the underlying mechanism will be explained in the framework of energy minimization.

In Chapter 4, we explored further the shape-engineering properties by studying three technologically important ferromagnetic/nonmagnetic/ferromagnetic (F/N/F) trilayers: asymmetric rings (section 4.1), elongated ellipses (section 4.2), and combined square-disk elements (section 4.3). These structures are the key to practical device applications such as spin valves (SVs) and magnetic tunneling junctions (MTJs). However, due to the overlapped signals contributing from all the magnetic layers, investigating the discrete magnetic process within each magnetic layer presents a major challenge for conventional characterization techniques. Here, by combining quantitative off-axis electron holography and analytical phase calculation, we succeeded in identifying and measuring the detailed reversal processes and domain wall movements confined within these intriguing structures in a layer-resolved fashion.

Chapter 5 concerns the fast dynamic properties of magnetic vortex structures.

Recent discovery of spin toque transfer (STT) offers a new route of writing magnetic information by direct exchange of spin angular momentum from a polarized current. This novel concept could potentially solve the longstanding writing dilemma in magnetic data storage devices. A particularly interesting system to explore the STT effect is current driven vortex precession. In this chapter, we designed and constructed a special high frequency TEM stage and observed for the first time precession trace of vortex core with nanometer resolution. We systematically mapped the steady state precession orbits as a function of both frequency and current density, and succeeded in quantifying the resonant frequency and damping coefficient that governs the vortex dynamic motion.

Finally, Chapter 6 concludes the dissertation by providing a brief outlook for future research perspectives. We will discuss the fundamental limitations inherent to the TEM technique, and highlight several latest progresses of instrumental development that may inspire further research efforts.

Chapter 2. Fundamentals of the Experimental and Theoretical Methods

2.1 Magnetic Imaging

2.1.1 Basics of TEM

Inside a transmission electron microscope, the incident electrons are provided by an electron gun. Presently, both thermal and field emission emitters are in use. In a thermal emitter, the filament consists of a tungsten or LaB_6 crystal, and is resistively heated to emit electrons. In a field emission gun (FEG), electrons are extracted by the electric field from a finely pointed cathode. The sharp tip creates a strong electric field at its very end, so that electrons are emitted from a very limited area. This design provides an excellent spatial coherence of the electron wave.

The emitted electrons are then accelerated in a multistage process to reach their final highly relativistic energy of several hundred keV. Leaving the gun area, the electron beam is modified by a condenser lens system consisting of at least two lenses and one aperture. These lenses define the illuminated area on the specimen. The conventional transmission electron microscope (CTEM) uses a broad circular beam with a diameter of about 0.5 to 1.0 microns at sample plane, which is then transmitted through a suitably thinned specimen.

The specimen itself is inserted into the electron microscope column by using the specimen holder. The planar dimension of the sample is restricted to approximately 3 mm. The specimen holder is vacuum locked and mechanically controlled by the side-entry goniometer, which can tilt the holder with high precision to bring specimen into a convenient imaging orientation.

Once the holder is fully inserted, the sample is situated inside the objective lens, which often acts as a combination of a further condenser lens and an imaging lens. The magnetic field in the fully excited objective lens exceeds 2 Tesla for a 200 keV TEM, and would severely influence the micromagnetic configuration of the specimen. Therefore, it can not be directly used for magnetic imaging operations. A different approach uses a special Lorentz lens, which allows investigation with virtually zero magnetic fields in the sample region. The details of Lorentz microscopy will be discussed in later sections.

Several lenses (intermediate and projection lenses) follow, which magnify the TEM image even further.

A fluorescent screen allows the quick visual inspection of image during operation. CTEM images have historically been recorded on photographic film, but digital recording with charge coupled device (CCD) cameras facilitates quantitative analysis, and has become widespread.

2.1.2 TEM-based magnetic imaging methods

As in neutron and x-ray scattering studies, electron microscopy detectors can only record the intensity (amplitude squared) of the wave function of the transmitted electron beam. However, the imaging electrons can be treated as waves, and as such they carry both amplitude and phase. The mechanism of imaging magnetic domains in magnetic materials relies on the Aharonov-Bohm effect [11], which describes the relative phase shift of two electron waves traveling from a point along two routes enclosing a zone with magnetic field distribution to the same point:

$$\Delta\phi = \frac{2\pi e}{h}\int \vec{B}\cdot d\vec{S} \tag{2-1}$$

where $d\vec{S}$ is a surface integral over the surface area enclosed by the two routes. Considering the transmission geometry, and by integrating along the beam trajectory (z direction), a further modification of equation (2.1) gives:

$$\Delta\phi = \frac{2\pi e}{h}\iint B_{\perp}\cdot dz\cdot dx \tag{2-2}$$

where $\int B_{\perp}\cdot dz$ describes the collected phase shift along the electron trajectories.

This notation also emphasizes that only the component of $B_{\perp}$ perpendicular to the electron beam's trajectory contributes to phase shift. In a further assumption, the induction is considered to be constant over the thickness z of the specimen. Therefore, the total flux contained within a rectangular section of the specimen $dx \cdot dz$ leads to the observable phase shift.

Thus, recovering the phase of the electron wave is the key to obtain the electric and magnetic information of the sample. A variety of special techniques have been developed for this purpose. [Table 2.1]. For the work described in this dissertation, we primarily rely on using two classic methods: Fresnel mode Lorentz microscopy and off-axis electron holography.

Lorentz Microscopy

The domain structure of a magnetic specimen is not readily visible under conventional imaging conditions. In particular, the strong magnetic field (about 2 Tesla) generated by the objective lens modifies or even completely wipes off (by saturation) any intrinsic magnetic microstructure inside a TEM specimen. Such severe restrictions for studying magnetic materials using the TEM have led to the development of several alternative imaging modes. These are collectively known as Lorentz microscopy, because they are all based on, in a non-quantum mechanical point of view, the sideways deflection of the charged high energy electron inside magnetic specimen by the Lorentz force [Figure 2.1]. Since the objective lens is usually switched off for Lorentz imaging, the spatial resolution of the magnetic detail revealed in Lorentz micrographs is substantially degraded when compared with conventional TEM imaging. However, this loss of resolution is not normally considered as a serious drawback since magnetic fields only rarely change abruptly on a sub-nanometer scale [12].

The simplest and classical technique for imaging magnetic domain structures is the so-called Fresnel, or defocus, mode of Lorentz microscopy [9]. Owing to the Lorentz force, the electrons traversing domains with different magnetization orientations are deflected in different angles, creating regions that have either an excess or a deficit of electrons immediately below the sample. By imaging in an under- or over- focus condition, a higher (or lower) intensity is recorded owing to the converging (or diverging) beams. Thus, in Fresnel imaging it is the change of the magnetic induction $\Delta\vec{B}$ which is imaged rather than the induction $\vec{B}$ itself. Domain walls appear as bright or dark lines, depending on the relative orientation of the magnetization in the two adjacent domains. It should be noted, however, that due to the necessary defocusing to be able to see contrast, one does unavoidably get Fresnel fringes, especially at the borders of the specimen. This is mainly due to electrostatic phase shifts.

Another alternative is so-called Foucault mode of Lorentz microscopy. It is equivalent to dark-field imaging, involving the use of a small aperture in the diffraction plane to select for imaging only those electrons that have been deflected in a specific angle (deflection angles are usually 10^3 times smaller than the Bragg angles) due to the magnetic structure in the specimen. An image which is obtained in the back focal plane shows dark domains, if the corresponding magnetic induction is blocked by the aperture, otherwise the domains appear bright, with gradual shades in the boundary region. As pointed out in the preceding text, the angles between magnetically deflected beams and the central beam are very small. This makes the accurate positioning of the aperture a very tedious task.

Despite inherent spatial resolution limitations of Fresnel or Foucault imaging, either technique allows useful real-time viewing of dynamic processes. By taking Lorentz micrographs at different defocus conditions, phase information can be quantitatively reconstructed using the transport of intensity (TIE) equation [13].

Electron Holography

The technique of electron holography permits retrieval and quantification of both amplitude and the phase shift of the electron beam that has traversed through a TEM specimen, unlike the situation for normal imaging where all phase information is lost. Since the phase shift of the electrons which have passed through the sample can be directly related to magnetic (and electric) fields, electron holography provides a powerful way to probe magnetic microstructure on a quantitative level.

There are many variations of electron holography, and the most widely used form is known as off-axis or sideband electron holography [14] [Figure 2.2]. A FEG, which combines excellent temporal coherence with high brightness, is used as the electron source. The high energy electron beam is split in two coherent waves with the aid of a positively charged wire (bi-prism), one passing through the specimen (object wave) and the other through the vacuum (reference wave). The resulting interference pattern (or hologram) is digitally acquired by a slow-scan CCD camera. Subsequent image processing algorithm allows both the amplitude and phase shift of the high energy electrons to be retrieved.

During phase reconstruction, the hologram is first Fourier transformed to obtain the corresponding power spectrum, which contains an auto-correlation component and two sideband components that carry the desired phase information about the object. One of these first-order sidebands is selected for reconstruction, and a digital filter can be employed to correct the aberration. The filtered sideband is then inverse Fourier transformed to obtain the complex object wave function. Once the phase shift of the electron wave has been reconstructed, quantitative information with high spatial resolution about the magnetic (and electric) fields in a sample can be easily extracted. These mathematical protocols can be processed by commercially available software packages, e.g., HoloWorks.

A technical difficulty is that, in addition to the magnetic fields, the phase shift may also be caused by the mean inner potential of the material, which is not necessarily of interest for magnetic imaging. Various schemes have been developed to separate the magnetic phase shift from the electrostatic phase shift. The first option exploits the fact that the magnetostatic phase shifts will be inverted after a rotation of the specimen around a horizontal axis by 180°, while this is not the case for pure electrostatic phase shifts. Therefore, if two images are taken with the specimen rotated by 0° and 180° respectively, the magnetic and electrostatic phase shifts can be separated by addition or subtraction of the two images. Another option is to separate the two component by magnetic saturation [15]. It utilizes the fact that a magnetic particle saturated in two antiparallel directions reverses its magnetic contributions to the phase shift. Thus, the electric phase shift can be extracted from two images in antiparallel saturation simply by adding both phases, while the magnetic phases will cancel out. Once the electric phase is known, it can be then subtracted from images of the same particle recorded at arbitrary external field values.

Application of magnetic fields

To investigate the dynamic magnetization processes, it is necessary to generate a well-defined magnetic field in the specimen area. For thin film samples, in-plane magnetic fields are of particular interest.

One method utilizes the vertical magnetic field generated by the electromagnetic lens of the TEM itself. Usually one tries to minimize these fields by using a special low-field Lorentz lens. However, moderate vertical fields and specimen tilting can be used to generate the magnetic in-plane fields needed in the specimen plane. Usually, a fixed vertical field is applied and the strength of the specimen's in-plane field is regulated by changing the tilting angle.

Another method is to implement small electromagnetic coils on the specimen holder in order to generate pure in-plane magnetic fields. The current of these coils can be controlled and monitored by an external source-meter. However, due to the limited space on the specimen holder, only small coils can be implemented which in turn limits the maximal achievable magnetic field. Meanwhile, due to the high vacuum condition inside TEM column, the specimen holder is subject to severe heating once a current is passing through the coil wires. This places an upper limit for maximum current (corresponding to field of about 1kOe) that can be applied.

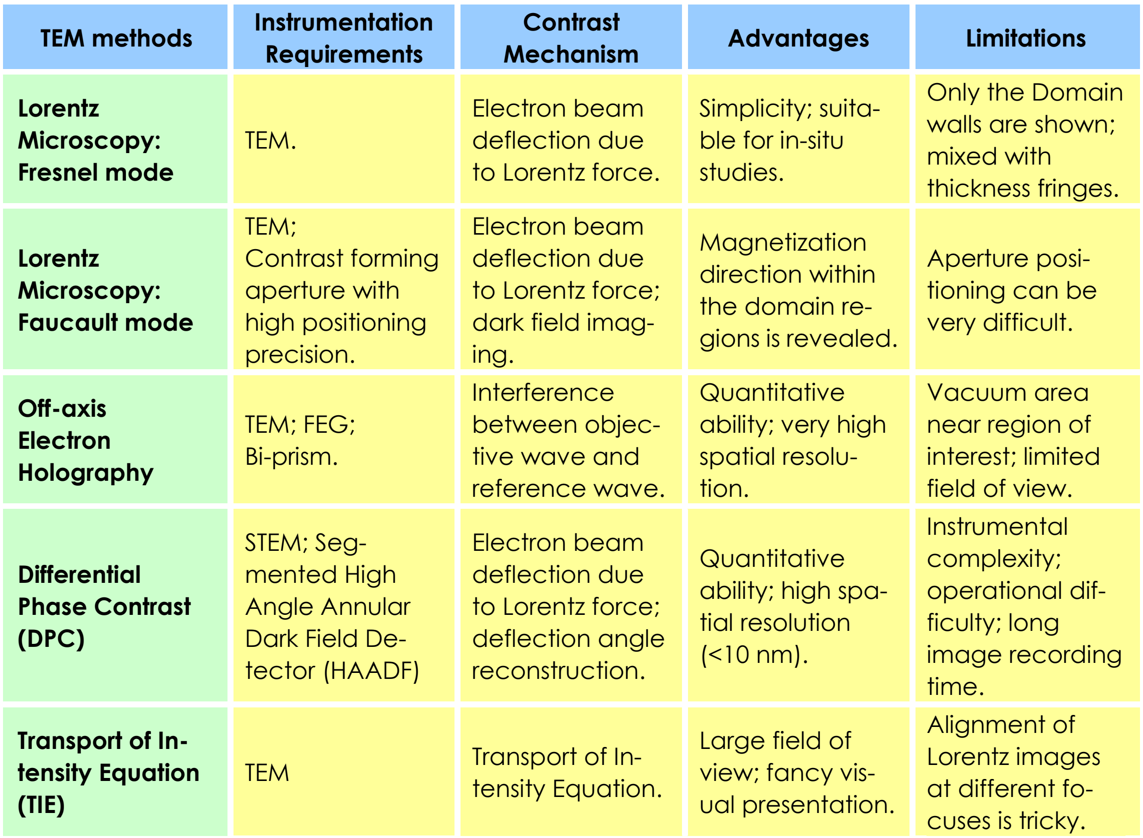

TEM methods	Instrumentation Requirements	Contrast Mechanism	Advantages	Limitations
Lorentz Microscopy: Fresnel mode	TEM.	Electron beam deflection due to Lorentz force.	Simplicity; suitable for in-situ studies.	Only the Domain walls are shown; mixed with thickness fringes.
Lorentz Microscopy: Faucault mode	TEM; Contrast forming aperture with high positioning precision.	Electron beam deflection due to Lorentz force; dark field imaging.	Magnetization direction within the domain regions is revealed.	Aperture positioning can be very difficult.
Off-axis Electron Holography	TEM; FEG; Bi-prism.	Interference between objective wave and reference wave.	Quantitative ability; very high spatial resolution.	Vacuum area near region of interest; limited field of view.
Differential Phase Contrast (DPC)	STEM; Segmented High Angle Annular Dark Field Detector (HAADF)	Electron beam deflection due to Lorentz force; deflection angle reconstruction.	Quantitative ability; high spatial resolution (<10 nm).	Instrumental complexity; operational difficulty; long image recording time.
Transport of Intensity Equation (TIE)	TEM	Transport of Intensity Equation.	Large field of view; fancy visual presentation.	Alignment of Lorentz images at different focuses is tricky.

Table 2.1 Comparison of different TEM-based magnetic imaging techniques.

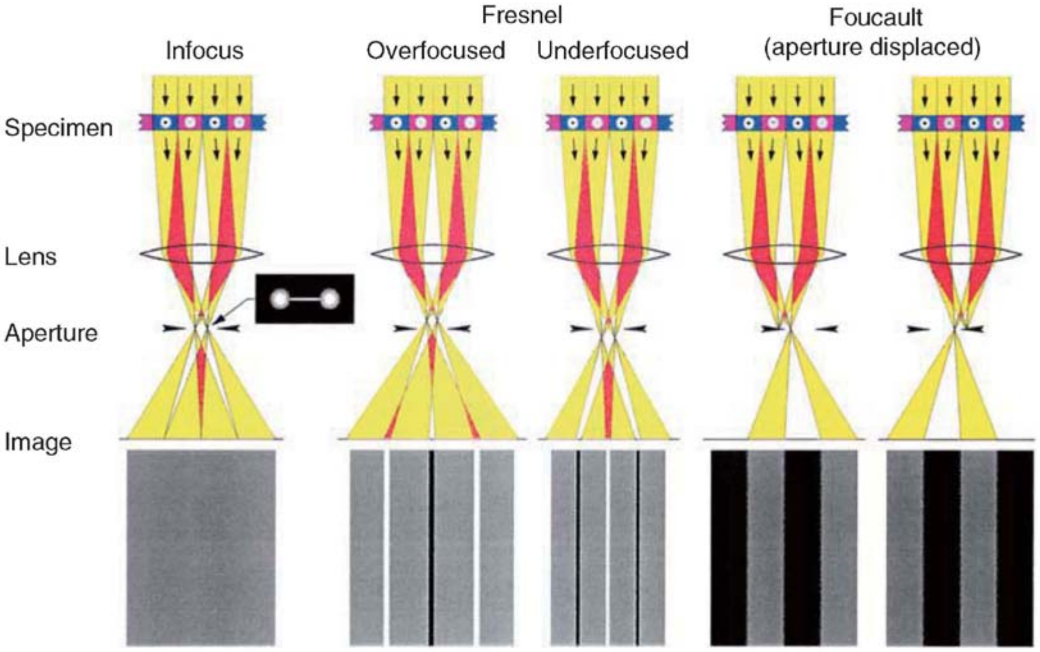

Figure 2.1 A schematic diagram of the Fresnel and Foucault modes of Lorentz microscopy (adopted from reference [10]).

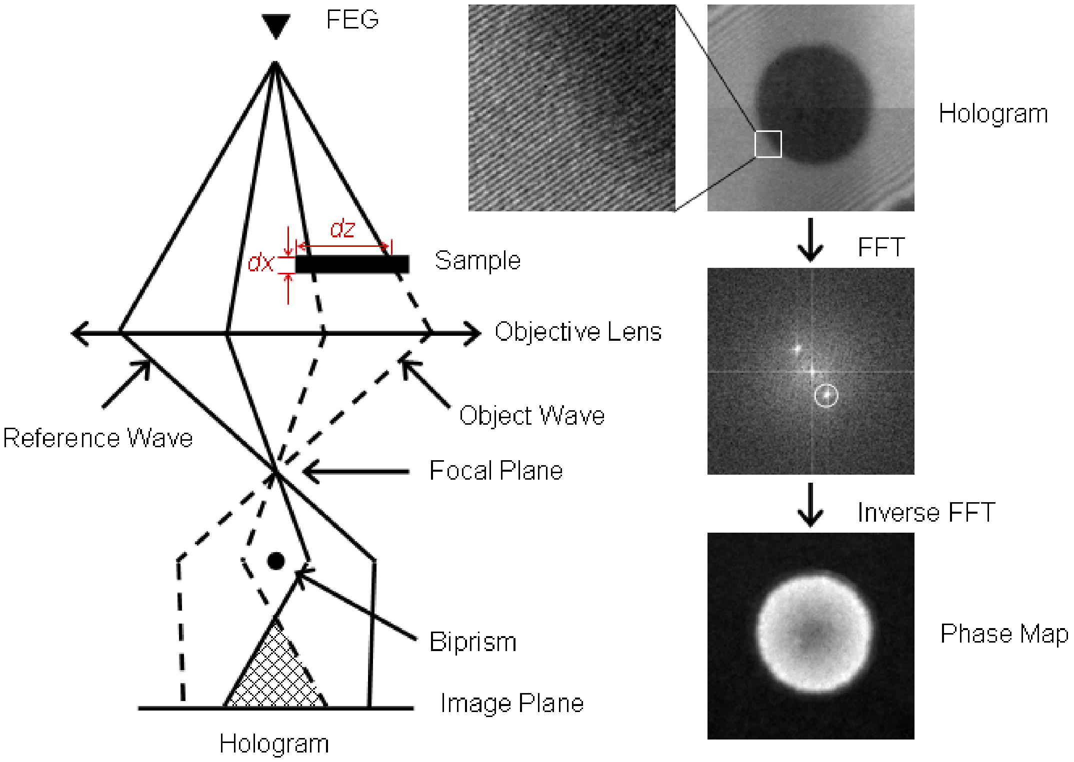

Figure 2.2 Left panel: A schematic diagram of off-axis electron holography. Right panel: phase reconstruction procedures.

2.1.3 TEM Instrumentation and Calibration

Here in Brookhaven, we used two TEMs for conducting *in-situ* experiments and analysis: the JEOL 3000F high resolution microscope and the JEOL 2100F-LM Lorentz microscope dedicated to magnetic imaging.

JEOL 3000F

The JEOL 3000F is a 300 kV field-emission microscope equipped with a variety of attachments to make it a powerful analytical instrument. In addition to the base configurations, it is also equipped with a scanning transmission electron microscopy (STEM) unit, a high angle annular dark field (HAADF) detector, a TV-rate camera, an X-ray energy dispersive spectrometer (EDS), a post-column Gatan image filter (GIF), and an electron energy loss spectrometer (EELS). As a workhorse microscope, the JEOL 3000F provides the general flexibility to carry out conventional high resolution imaging, electron diffraction, and chemical analysis.

The high-resolution capability of the microscope is achieved by the ultra-high resolution objective pole-piece (URP), with a 2 mm gap for specimen holder insertion from the side. The spherical aberration coefficient (C_S) of the objective lens, important for determining the limits of image interpretation, is 0.55 mm, yielding 1.6 Å point resolution.

While the JEOL 3000F is certainly not dedicated to magnetic applications, a Lorentz mode is available with the main objective lens switched off and the objective mini-lens used for imaging. During *in-situ* magnetization experiments, the objective lens is slightly excited to generate a controlled magnetic field along column direction, and the sample tilt is varied to acquire desired in-plane field component. The detailed calibration of magnetic field as a function of objective lens excitation will be discussed in later sections. Moreover, a bi-prism is also installed which enables electron holography to be carried out at low, medium and high magnifications.

The column diagram and lens locations of JEOL 3000F is listed in Appendix A.

JEOL 2100F-LM

The JEOL 2100F-LM is a state-of-art field-emission microscope dedicated to magnetic imaging and electron holography applications. The objective lens pole-piece has been redesigned to be different than most conventional microscopes. Instead of concentrating the field of the objective lens in the narrowly confined gap, the upper pole-piece of the JEOL 2100F-LM consists of a mu-metal cage with a specimen entry port of 8 mm tall [Figure 2.3]. The specimen is situated above the pole piece gap; fields produced by the objective lens are routed through the mu-metal cage, leaving the specimen region virtually field-free. Such design provides the unique ability to observe magnetic specimens in a low field environment while retaining 7.5 Å resolution (with C_s of 109 mm).

In addition, the objective lens has an unusually long focal length of 17 mm which provides far-field diffraction capabilities. For most conventional microscopes, including the JEOL 3000F, the objective lens has to be switched off during magnetic imaging. Switching off the objective lens, however, prohibits the formation of the diffraction pattern at the normal back focal plane. To accommodate this change, the objective mini-lens, the intermediate lens, and the projector lens must be independently excited in the free-lens control mode. The selected area electron diffraction (SAED) pattern recorded in this manner suffers from severe distortion. For JEOL 2100F-LM, however, the low-field environment can be sustained even with the objective lens normally excited, and therefore, field-free SAED can be readily obtained in an undistorted fashion.

The detailed column diagram and lens locations of JEOL 2100F-LM can be viewed in Appendix A.

Magnetic Field Calibration

In studies of magnetic materials using a TEM, important information of magnetic structure and domain configuration down to the nanometer scale can be obtained through the Lorentz mode as discussed in the previous chapter. Typically, the main objective lens of the microscope is switched off during these studies, and imaging is performed with a secondary Lorentz lens. The reason for this is to avoid saturating sample with the strong field (30 kOe) of the main objective lens. Nevertheless, the remanent field from the objective lens, even while switched off, can produce fields at the sample region on the order of a few hundred Oersted. Indeed, this fact has been exploited to carry out *in-situ* magnetization experiments by tilting the sample in this remnant field. Regardless of the experiment, however, it is important to characterize the field generated by the microscope itself in the region of the sample.

The magnetic field characteristics of both JEOL microscopes have been measured, by using a modified TEM holder adapted with a micro hall probe [16]. The field was characterized along two orthogonal directions, one perpendicular to the specimen plane and the other along the axis of the holder.

At default sample position, out-of-plane field was first measured as a function of the objective lens (OL) excitation [Figure 2.4]. This calibration is very important for tilting-based *in-situ* experiments, where proper excitation level of OL can be used to generate magnetic field of desired strength. For JEOL 3000F, the out-of-plane field increases monotonically with the OL excitation, and the dependence is almost linear below 1 V. The wide range of attainable magnetic fields enables us to perform *in-situ* experiment at relatively small tilting angles. In contrast, JEOL 2100F-LM shows very different behavior due to its redesigned low-field pole piece. Below 0.85 V, the field is virtually absent (less than 4 Oe), and a “field free” operational condition can therefore be expected at the specimen region. Above 0.85 V, which is higher than the OL excitation for standard operating conditions (0.76 V), we measured a linear increase of the magnetic field as a function of OL excitation. Considering the mu-metal cage design, the strong field generated by OL must be fully saturating the cage material such that it can not effectively shield magnetic flux anymore.

We then measured the magnetic fields at various positions during the sample insertion process. In the case of 2100F-LM, we made measurements with the OL on and off. For the 3000F, we only made measurements with the OL off since we are primarily interested in the Lorentz mode for that microscope. The results are shown in Figure 2.5, for out-of-plane and in-plane direction, respectively. It is evident from the top figure that there is a significant difference for JEOL 2100F-LM depending upon whether OL is switched on or off. When the lens is excited, the sample is subjected to about 350 Oe field during insertion, with the strongest field experienced as it traverses the gap in the mu-metal shielding. With OL off, however, the sample is subjected to a significantly reduced field of 18 Oe. When fully inserted, the measured field is 4 Oe and 0 Oe for OL on and off, respectively. On the other hand, for JEOL 3000F with OL off, the field is continuously increasing as sample is approaching the center of column. With sample fully inserted, the measured field is 290 to 315 Oe. This suggested that in conventional TEM, where the pole pieces are specifically designed to generate a localized strong magnetic-lensing effect, the remnant field remains high even with lens completely switched off.

The bottom part of Figure 2.5 shows the in-plane field measurement. This field is generally quite small (less than 8 Oe) for the JEOL 3000F, even at the center of the pole piece (l.8 Oe). Compared with the out-of-plane measurement, clearly the OL remanent field for the 3000F is predominantly aligned perpendicular to the plane of the sample. In the case of JEOL 2100F-LM, there is again a significant difference depending on whether OL is on or off. When OL is on, the in-plane field is quite large on average. When OL is off, the field is significantly smaller (less than 18 Oe). These measurements strongly suggest that OL lens should be turned off before and during sample insertion in order to avoid undesired magnetizing effect.

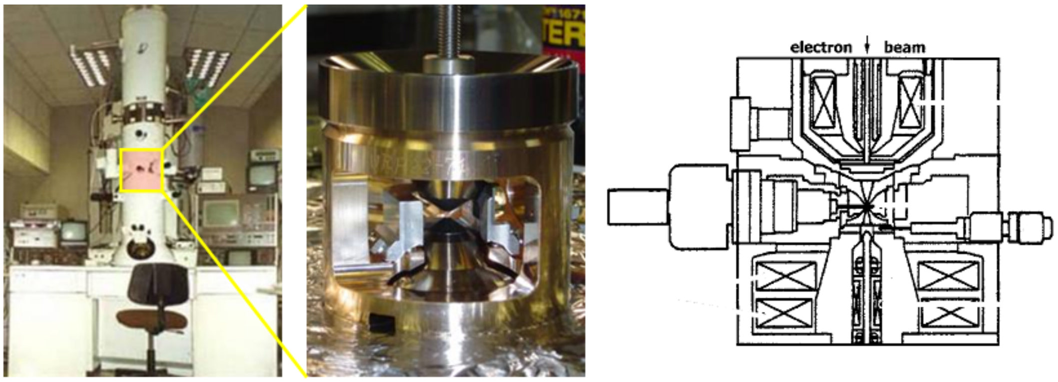

JEOL 3000F

Regular Pole Piece

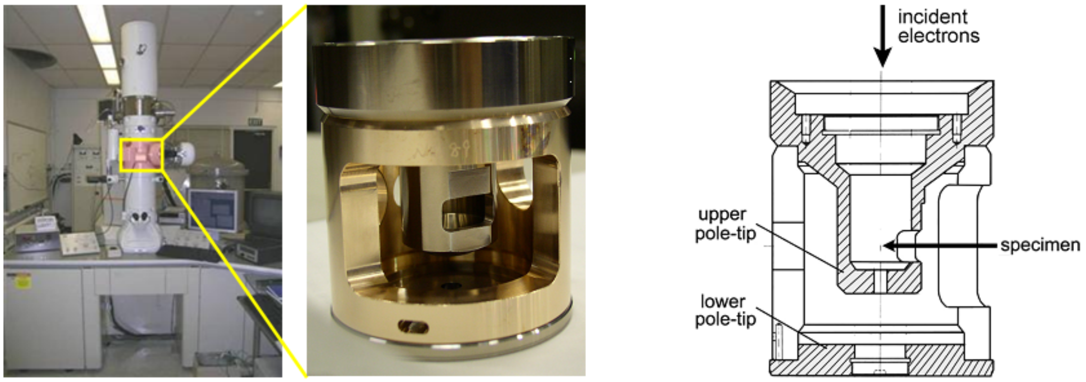

JEOL 2100F-LM

Lorentz Pole Piece

Figure 2.3 Comparison between JEOL 3000F regular TEM and JEOL 2100F-LM “field free” Lorentz TEM.

In JEOL 3000F, the pole piece features a symmetric design, with specimen sitting in between upper and lower part. In JEOL 2100F-LM, a mu-metal cage with a side entry port create a field-free specimen environment.

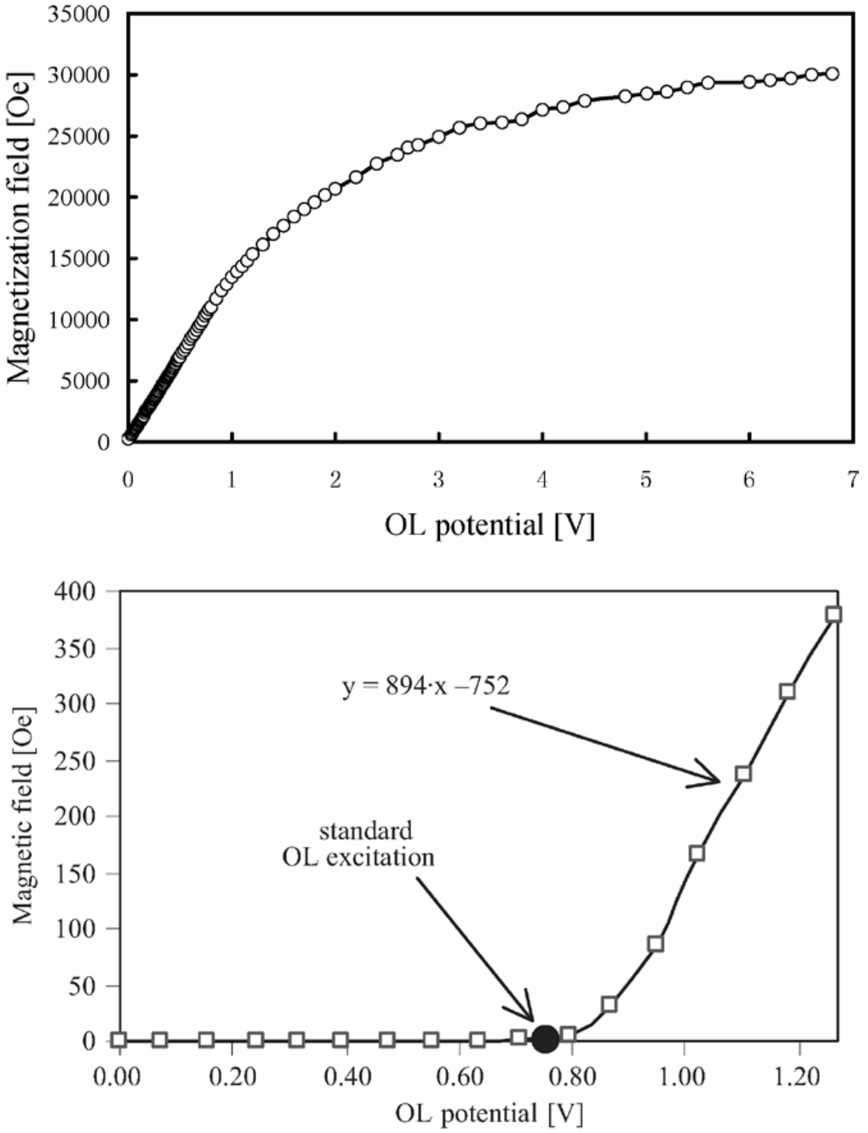

Figure 2.4 Field measured along the optical axis (or out-of-plane) as a function of OL excitation.

Top and bottom plot corresponds to field measurement for JEOL 3000F and JEOL 2100F-LM, respectively.

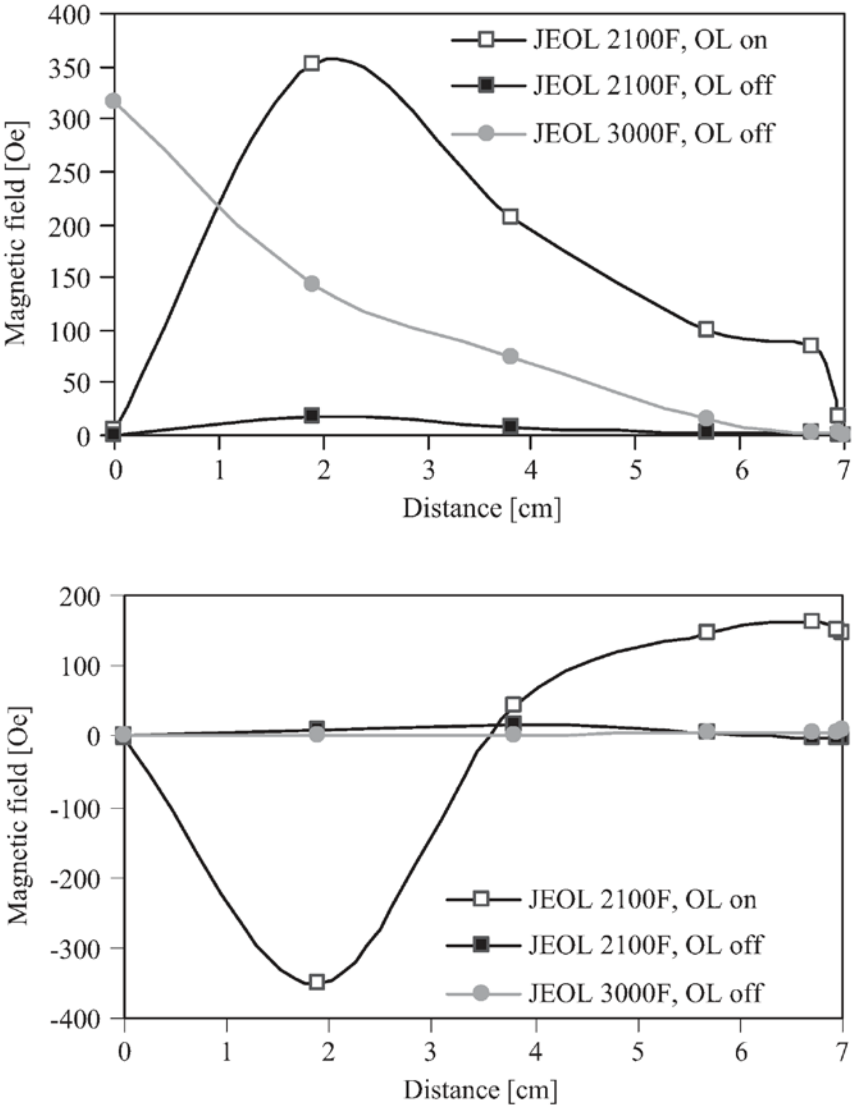

Figure 2.5 Magnetic field as a function of distance from the center of the TEM column for the JEOL 2100F-LM and 3000F.

Top plot corresponds to field measurement along optic axis (or out-of-plane). Bottom plot corresponds to field measurement along the holder axis (or in-plane). Independent measurement for the JEOL 2100F-LM were made with OL on and off. “7” and “0” cm corresponds to the specimen position at the load-lock and the center of the microscope column, respectively.

2.2 Sample Growth and Patterning

2.2.1 General Considerations

Any specimens suitable for TEM studies must meet several basic criteria:

1. Less than 3 mm in planar size (to fit regular TEM sample holder);
2. Thin enough to be electron transparent;
3. Stable under the electron beam irradiation (without charging or vacuum outgassing).

We used silicon nitride (Si_3N_4) self-supporting membranes as substrates to prepare our TEM specimens. These membranes are commercially available, having a single square (0.5 mm×0.5 mm) window centered on a 200 μm thick silicon frame. The TEM window frames are octagon shaped and can fit inside the 3 mm diameter circle typical of a TEM specimen holder [Figure 2.6]. The silicon nitride membrane is ultra flat, low stress and reasonably robust against thermal or mechanical agitations. The membranes are provided with different thicknesses, including 50 nm, 100 nm, and 200 nm, and can be selected depending on specific applications.

A critical point in specimen preparation for TEM investigations are charge effects. For example, silicon nitride is an insulating material and therefore is subject to electron beam charging during observation. This causes deflections and/or instabilities of the electron beam and can in severe cases prevent proper investigation of the specimen. To avoid this, it is helpful to coat the entire sample, including the membrane, with a very thin (less than 5 nm) layer of conductive material such as Cr. In practice, this is usually done on the back surface of the membrane in order to avoid shorting the microstrip circuits on the top surface.

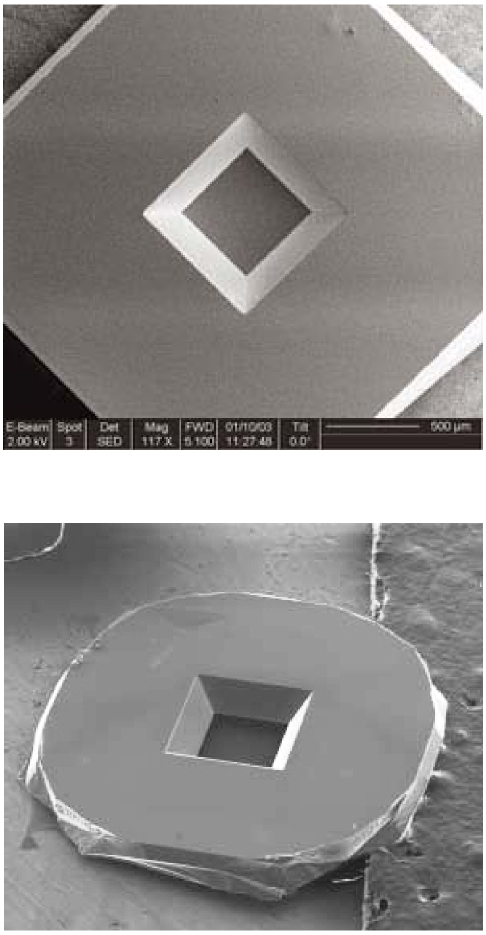

Figure 2.6 SEM images (top: top-view, bottom: tilted-view) of the silicon nitride window.

2.2.2 Thin Film Deposition

We designed and built an ultra high vacuum (UHV) electron beam evaporator system to suit our thin film deposition needs, as shown in Figure 2.7. This is a home-assembled dual-gun (3 kW), six-target (3×2) system. The vacuum system consists of two chambers (Kurt J. Lesker Co.): sample load lock and main deposition chamber.

The load lock provides a small volume for sample transfer; it may be vented and evacuated quickly and frequently without causing pressure degradation in the main deposition chamber. It is pumped by a turbo-molecular-drag pump (BOC Edwards, EXT 255H), which is backed by a Varian TriScroll 300 dry roughing pump. The load lock is routinely maintained at 10^{-7} Torr range.

The main deposition chamber is pumped by a large ion and titanium sublimation (TSP) combo pump (Varian Vaclon Plus 500 Starcell), and is routinely maintained in the low 10^{-10} Torr range. The vacuum environment, including species and amount of residue gases, is monitored by a Residual Gas Analyzer (Kurt J. Lesker AccuQuad). During evaporation process, film thickness is measured by one of the two quartz crystal thickness monitors (McVac).

Figure 2.8 is a close-up view of the electron gun assembly. Each 3 kW gun has three crucibles containing source material and a beam-sweep (Thermionics, model 100-0030). The operating voltage on each of these guns is 4 kV. Current required to melt magnetic sources is typically between 40 and 80 mA. A pair of permanent magnets creates a magnetic field which can shape and direct the path of the electron beam.

During the evaporation process, a tungsten filament inside the electron gun is heated. The gun assembly is located outside the evaporation zone to avoid contamination by evaporant. When the filament becomes hot enough, it begins to thermionically emit electrons. These electrons form a beam which is deflected and accelerated toward the material to be evaporated by means of the magnetic field. As the electron beam strikes the target surface, the kinetic energy of motion is transformed by the impact into thermal energy (heat). A pair of beam sweeper assembly confines the electron beam spot in circular or figure-eight pattern to enable uniform heating of the target material. The crucible liners are use for most target materials, and are combined with water cooling in order to reduce the intensive heat generated by the electron beam.

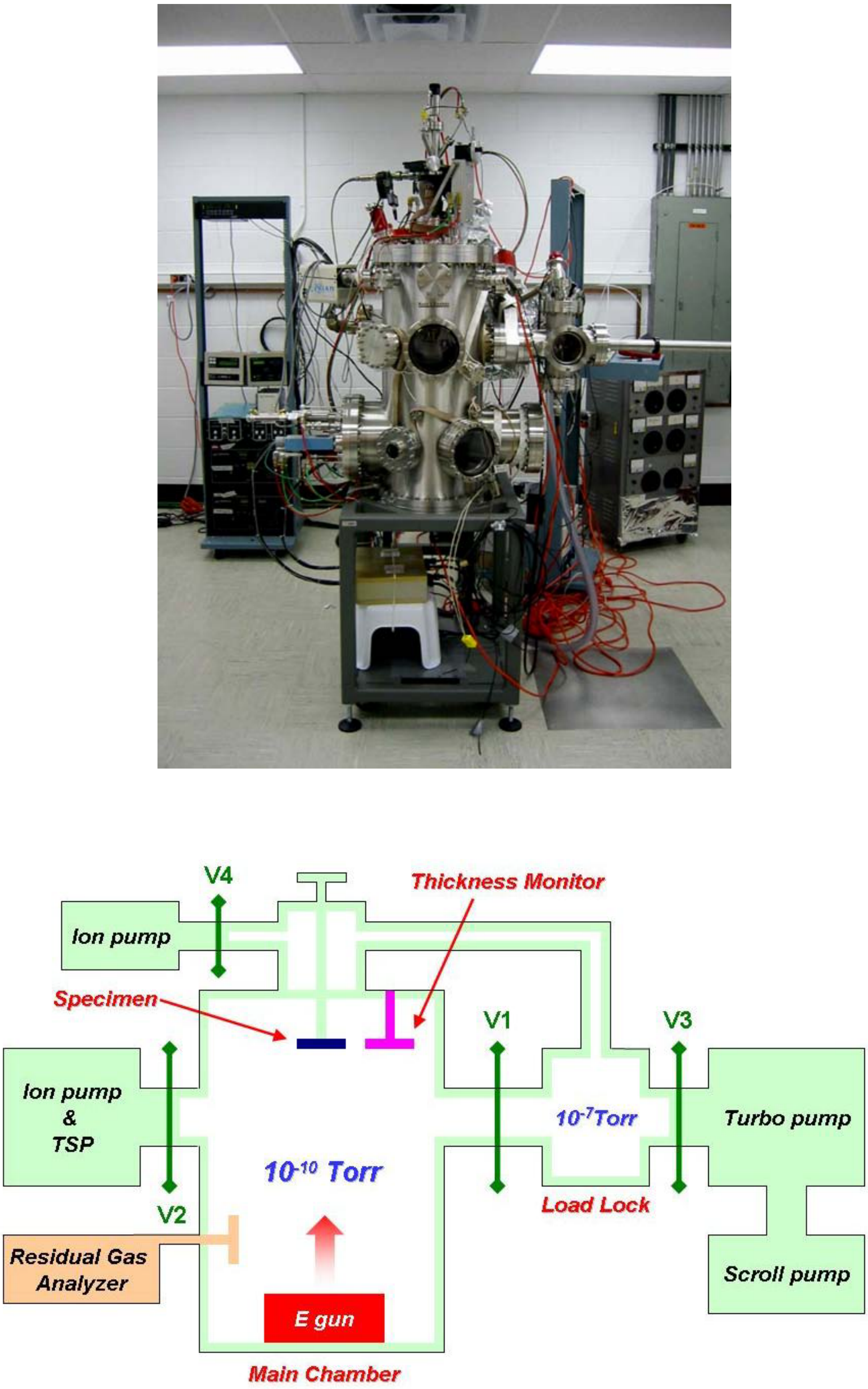

Figure 2.7 Picture and vacuum logic of the UHV electron beam evaporator.

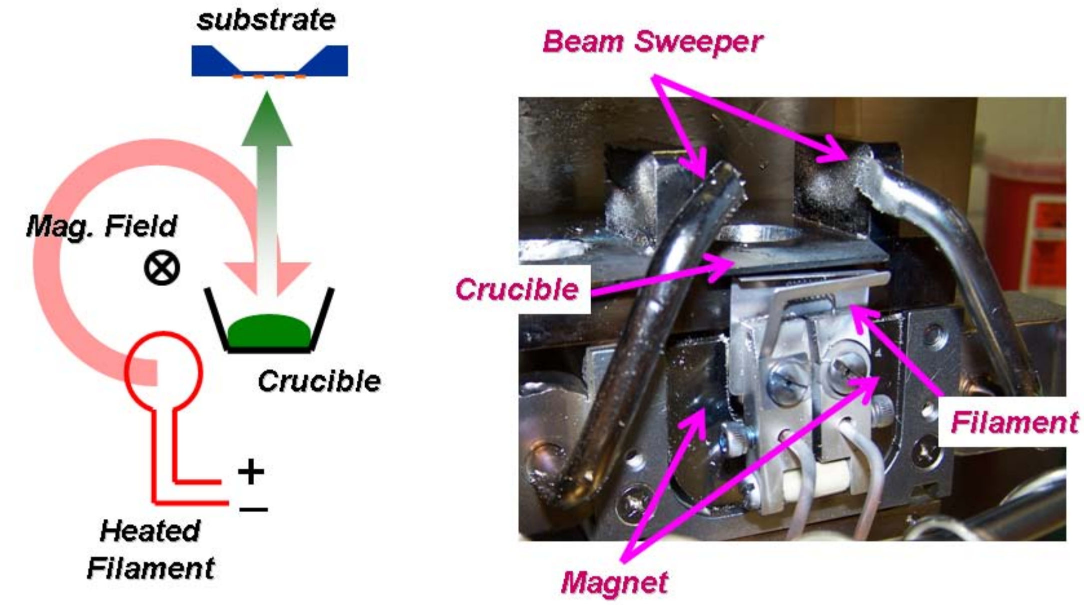

Figure 2.8 Schematic and image of the electron gun assembly.

2.2.3 Electron Beam Lithography and Lift-off

A metallic thin film can be patterned into discrete structures by two distinct routes: additive or subtractive processes. In additive process, a lithographic method is used to define the required pattern in a resist on the substrate of interest, followed by film deposition and lift off. In contrast, the subtractive process involves lithographically patterning the resist spun onto an already deposited film, after which etching is used to transfer the pattern to the film. For the submicron structures of interest here, electron beam lithography is the natural choice for pattern definition. Throughout this dissertation, we use the additive approach to fabricate the magnetic nanostructures. This route is convenient and simple, involving less processing steps that may increase the risk of accidental membrane damage. Our nanofabrication work was primarily done using the clean room facilities in the Center for Functional Nanomaterials (CFN) at Brookhaven National Laboratory.

The principle of electron beam lithography goes as follows [17]. Electron beam resists are the recording and transfer media for the lithography process, which are usually in the form of polymers dissolved in a liquid solvent. Liquid resist is first dropped onto the flat surface of substrate, which is then spun at high rotational speed to form a uniform coating. After baking out the casting solvent, electron exposure breaks polymer backbone bonds, leaving fragments of lower molecular weight. A solvent developer then selectively washes away the lower molecular weight fragments, thus forming a positive tone pattern in the resist film. After evaporation of desired thin films, this pattern is transferred to the substrate by “liftoff” of excessive material.

A general sample production session includes six steps, which are discussed in detail as follows [Figure 2.9].

Step 1: Pattern Design

During this step, patterns are created using DesignCAD, a computer aided vector drawing program. Different drawing elements may be used: lines, circles, circular arcs of arbitrary orientation and width, and filled polygons. Patterned elements that are to have different exposure parameters are labeled by different graphic layers and/or different colors. Once a pattern is designed, it is converted to a file format that is directly recognizable by the electron beam writer, using a separate interfacing program called Nanometer Pattern Generation System (NPGS).

Step 2: Resist Coating

During this step, electron beam resist is spin coated onto silicon nitride membrane and baked for polymer cross-linking. A bi-layer resist system consisting of polymethyl methacrylate (PMMA) and copolymer of methyl methacrylate and methacrylic acid [P(MMA-MMA)] is used. The reason to use two layers is that the copolymer has a higher sensitivity than the PMMA, and therefore under the same electron beam irradiation dose, the bottom copolymer layer is essentially overexposed and forms a wider mask than the upper layer. This forms a large ‘undercut’ profile. When the material is then deposited into the pattern, the upper (narrower) mask of PMMA defines the overall dimensions of the structure deposited. Since the underlying (wider) mask of copolymer is hardly in contact with the deposited patterned material, the subsequent lift-off process of the resist is largely facilitated.

A typical resist coating session includes following steps::

1. Copolymer (MMA (8.5) MMA) with 9% solids in ethyl lactate is spun coated on membrane substrate with 3000 rpm for 40 s.
2. The coated sample is baked on hotplate at 170 °C for 90 s.
3. PMMA (950 k molecular weight) with 4% solids in chlorobenzene is spun coated onto the sample with 3000 rpm for 40 s.
4. The coated sample is baked on hotplate at 170 °C for 90 s.

Step 3: Electron Beam Exposure

During this step, the sample is loaded into an electron beam writer so that the polymer resist can be exposed according to the design pattern defined in step one. We used a FEI Helios Dual-beam system operated at 20 kV accelerating voltage. The fast beam blanking system is externally controlled by the NPGS program while electron beam is scanned across the sample surface, so that pre-defined exposure dose (or dwell time of electron beam) can be sequentially applied. The polymers in the exposed areas are broken into low-weight molecules and fragments, which make them soluble in developer. We used an area dose of 600 μC/cm^2 for the bi-layer system.

Step 4: Developing the Resist

During this step, exposed resist is removed from sample surface so that the designed pattern opens up. Specifically, the sample is first developed in 3:1 isopropyl alcohol (IPA) : methyl isobutyl ketone (MIBK) for 60 s. Immediately after that, the sample is rinsed in IPA for 30 s, followed by de-ionized (DI) water for 20 s, and then blow dried with a clean nitrogen gas. This terminates the develop process and prevents scumming. Subsequently, the sample is post-baked on hotplate at 100 °C for 60 s to remove residual developer, rinse solvent, and excessive moisture from resist image.

Step 5: Thin Film Deposition

During this step, desired thin film material is evaporated onto samples. This can be done using different methods, such as thermal evaporation, electron beam evaporation, and sputtering. Each evaporation method has its own pros and cons. For example, thermal evaporation, although simple to carry out, usually is done with very poor vacuum condition, and consumes excessive amount of source material during each operational session. Sputtering, although widely used in thin film growth, is problematic for lithography applications due to its isotropic nature and sidewall deposition. In comparison, electron beam evaporation provides very high quality film at a reasonable material/time cost, and is therefore the preferred method.

Special attention must be paid on substrate temperature during evaporation process. If the temperature is too high, it can potentially melt the polymer resist to change its profile, causing undesired distortion and edge-rounding. This is usually less severe for regular metallic materials involved in our study, including Cr, Au, Al, Ti, and Py. However, the resist can be badly damaged during the evaporation of certain high melting point refractory materials such as graphite (C).

As another general precaution, many ferromagnetic materials suffer from oxidation. It is therefore necessary to cap the magnetic structures with a protective layer. Commonly used elements for this purpose are Al, Cr or Ti due to their fine grain size.

Step 6: Lift off

During this last step, the sample is soaked in a polar solvent until the remaining resist dissolves and the evaporated metal on top of the resist floats away. For large features with thick resist, this step is usually very straightforward, however, for small features where the resist undercutting may be marginal, successful lift-off can be difficult and tricky.

We usually perform the lift-off step by soaking the sample in Remover PG, an N-Methylpyrrolidone (NMP) based solvent, at elevated temperature of 80 °C for at least 2 hours. After material is removed, the sample is further rinsed in IPA for 30 s, followed by DI water for 20 s, and then blow dried with a clean gas.

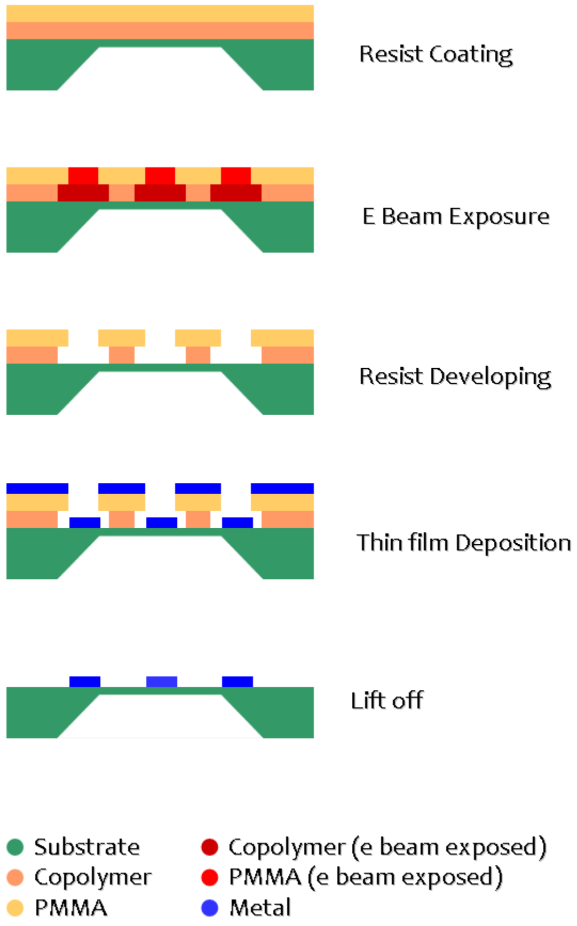

Figure 2.9 Schematic flow chart of the electron beam lithography and lift off process.

2.3 Micromagnetic Simulation

2.3.1 Energy Terms of an Ideal Ferromagnetic System

The continuum theory of micromagnetism, which was developed in the 1930s and 1940s, was intended to bridge the gap between the phenomenological Maxell's theory of electromagnetic fields and quantum theory based on atomic spins. In Maxwell's theory, material properties are described by global permeabilities and susceptibilities valid for macroscopic dimensions. On the other hand quantum theory allows a description of magnetic properties on the atomic level. Both theories are not suitable to describe cooperative and interactive phenomena such as macroscopic domain structure or magnetization processes of ordered spin structures.

The theory of micromagnetism focuses on the minimization of the total Gibbs free energy involved in a homogeneous ferromagnetic object. Fundamental to the solution of the energy minimization problem is the assumption that the vector of spontaneous magnetization $\vec{M}(\vec{r})$ has a constant magnitude but variable direction. The magnitude M_s corresponds to the saturated magnetic moments per unit volume. $\vec{M}(\vec{r})$ can therefore be expressed as:

$$\vec{M}(\vec{r}) = (M_x(\vec{r}), M_y(\vec{r}), M_z(\vec{r})) = M_s \cdot (\alpha(\vec{r}), \beta(\vec{r}), \gamma(\vec{r})) \tag{2-3}$$

where $\alpha(\vec{r})$, $\beta(\vec{r})$, and $\gamma(\vec{r})$ are the directional cosines of the magnetization vector with respect to Cartesian coordinates. In an ideal magnetic system, the total Gibbs free energy can be calculated as the sum of four principal terms (exchange energy, magneto-crystalline anisotropy energy, Zeeman energy and demagnetization dipolar energy):

$$E_{total} = E_{ex} + E_{an} + E_H + E_{dipole} \tag{2-4}$$

The exchange energy E_{ex} describes the energy penalty associated with non-uniform magnetization distributions in ferromagnetic materials. Phenomenologically, this energy can be written in the form of:

$$E_{ex} = A\int_V dV[(\nabla\alpha)^2 + (\nabla\beta)^2 + (\nabla\gamma)^2] \tag{2-5}$$

where A is the exchange stiffness constant. The exchange interaction is strong in magnitude while local in range. Therefore, it only enforces small angles between neighboring moments, while has virtually no effect on moments that are sufficiently far apart.

The magneto-crystalline anisotropy energy E_{an} originates from the coupling between spin and orbital moments (L-S coupling). Each type of crystal symmetry has its own preferred magnetization direction, or easy axis, for examples, the c-axis for hexagonally closed packed (hcp) lattice (such as Co), and $<111>$ axis for cubic lattices (such as Ni and Py). Different elements also vary in the strength of the coupling. In 3d transition metals the orbital moments are nearly completely quenched and consequently the coupling between the orbital moments and the crystal field remains small, leading to moderate magnetocrystalline energies. In contrast, in the case of intermetallic compounds, where rare-earth metals are involved, the 4f electrons are characterized by strong L-S coupling where Hund's rules are valid, and the anisotropic charge cloud of 4f electrons interacts strongly with the crystal field resulting in large anisotropies.

The magnetostatic energy of the external field, often labeled as Zeeman energy or external energy, can be written as the sum of the interaction energies of local moments with the external magnetic fields. It is given by:

$$E_H = -\int_V dV[\vec{M}(\vec{r})\cdot\vec{H}_{ex}(\vec{r})] = -\vec{H}_{ex}(\vec{r})\cdot\int_V dV\cdot[\vec{M}(\vec{r})] \tag{2-6}$$

where $\vec{H}_{ex}(\vec{r})$ is the external magnetic field.

The dipole energy E_{dipole}, also known as demagnetization energy, arises from the interaction of the magnetic moments with the magnetic fields created by discontinuous magnetization distributions both in the bulk and at the surface. The surface charge density is given by:

$$\sigma(\vec{r}) = \vec{M}(\vec{r})\cdot\vec{n} \tag{2-7}$$

while the volume charge density is given by:

$$\rho(\vec{r}) = -\nabla \cdot \vec{M}(\vec{r}) \tag{2-8}$$

the scalar potential $U(\vec{r})$ is related to both charge contributions:

$$U(\vec{r}) = \frac{1}{4\pi}\int_{V_0} \frac{\rho(\vec{r}\,')}{|\vec{r}-\vec{r}\,'|} \cdot dV' + \frac{1}{4\pi}\int_{S} \frac{\sigma(\vec{r}\,')}{|\vec{r}-\vec{r}\,'|} \cdot dS' \tag{2-9}$$

and the demagnetization field can be derived from the scalar potential:

$$\vec{H}_m(\vec{r}) = -\nabla U(\vec{r}) \tag{2-10}$$

Knowing the demagnetization field, the dipole energy is given by:

$$E_{dipole} = -\frac{1}{2}\int_V dV[\vec{M}(\vec{r}) \cdot \vec{H}_m(\vec{r})] \tag{2-11}$$

Dipole energy is non-local in nature, and is highly sensitive to the boundary condition of a finite sample. It is the driving force that governs the formation of magnetic domains.

In many cases not all of these energy terms have to be explicitly included. For example, in non-textured polycrystalline films, random grain orientations largely cancel out the effect of magneto-crystalline anisotropy, so this energy term is usually ignored.

Micromagnetic equilibrium conditions are derived with respect to the orientation of the vector of spontaneous magnetization. Accordingly, the static equilibrium equations can be written as a torque equation:

$$\vec{L} = \vec{M}(\vec{r}) \times \vec{H}_{eff}(\vec{r}) = 0 \tag{2-12}$$

Here, $\vec{H}_{eff}(\vec{r})$ denotes the so-called effective field, which can be defined from the total system energy as:

$$\vec{H}_{eff} = -\frac{\partial}{\partial \vec{M}(\vec{r})} E_{total} \tag{2-13}$$

Therefore, the effective field incorporates all the effects of exchange, anisotropy, external fields and demagnetization fields.

2.3.2 Landau-Liftshitz-Gilbert (LLG) Equation

The micromagnetic theory of dynamic magnetization processes deals with the problems of reducing energy losses, achieving small switching times in demagnetization processes of small particles and thin films and the calculation of resonance frequencies and spin-wave spectra.

Starting from the classical equation for the rotational motion of a rigid body, $\frac{d\vec{P}}{dt} = \vec{L}$, where $\vec{P}$ is the angular momentum and $\vec{L}$ the torque acting on the body, the equation of motion of the magnetic moments is obtained by using the magneto-mechanical analogue $\vec{M}_s = \gamma \vec{P}$ and inserting the magnetic torque $\vec{L} = -\vec{M}_s \times \vec{H}_{eff}$, which gives for the undamped rotational motion:

$$\frac{d\vec{M}}{dt} = -\gamma \vec{M} \times \vec{H}_{eff} \tag{2-14}$$

Here γ denotes the gyromagnetic ratio, $\gamma = -\frac{g\,|e|}{2m} = -1.1051\, g(sA/m)^{-1}$. Landau and Lifshitz have expanded equation (2.14) by introducing a damping term:

$$\frac{d\vec{M}}{dt} = -\frac{\gamma}{1+\alpha^2}\vec{M} \times \vec{H}_{eff} - \frac{\gamma\,\alpha}{(1+\alpha^2)M_S}\vec{M} \times (\vec{M} \times \vec{H}_{eff}) \tag{2-15}$$

An equivalent expression of LLG equation is given by:

$$\frac{d\vec{M}}{dt} = -\gamma[\vec{M} \times \vec{H}_{eff}] + \frac{\alpha}{M_S}\vec{M} \times \frac{d\vec{M}}{dt} \tag{2-16}$$

where the first term on the right hand side describes a precessional rotation of $\vec{M}_s$ with frequency $\omega = \gamma \left|\vec{H}_{eff}\right|$, and the second term describes the relaxation and rotational damping of $\vec{M}_s$ toward the direction of the effective field, with α being the damping constant [Figure 2.10]. The damping constant is a phenomenological parameter, which depends strongly on the local geometry, anisotropy and morphology.

The mechanisms governing the relaxation processes are only poorly understood so far, but they seem to offer a key to manipulating spin dynamics on the nanoscale. Typical precession frequencies for micro-sized elements are in the GHz regime, while the relaxation time can extend into several 100 ps.

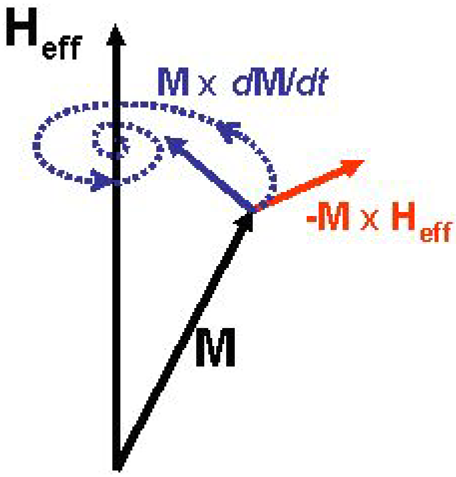

Figure 2.10 Geometry of the precession force (blue arrow) and dissipation force (red arrow) described by Landau-Liftshitz-Gilbert Equation.

2.3.3 Micromagnetics Simulation Using Finite Difference Methods

This section considers the finite difference approach in solving the sets of equations involved in the micromagnetics theory, of which the basic objectives are the calculation of bulk magnetic properties or the simulation of dynamic magnetization processes [18].

As discussed in the preceding sections, both static and dynamic micromagnetic simulations start from the total Gibbs free energy of the magnetic system. For the calculation of static hysteresis properties, the total Gibbs' free energy is minimized with respect to the direction cosines of the magnetization for subsequently changing external field. For the simulation of dynamic magnetization processes, the equation of motion is solved for the magnetization vector.

Numerically, the continuous magnetization distribution of a ferromagnet can be approximated by a discrete magnetization distribution consisting of three dimensional rectangular mesh at points ($x_0 + n\Delta_x$, $y_0 + n\Delta_y$, $z_0 + n\Delta_z$). The computational cell, interior to the array, is centered about the sample point with dimensions $\Delta_x \times \Delta_y \times \Delta_z$. The main advantages of the finite difference approach are ease of implementation, simplicity of meshing, efficient evaluation of the demagnetization energy (via, e.g., fast Fourier transform (FFT) methods), and the accessibility of higher-order methods.

For the analysis of the equilibrium micromagnetic structure, the LLG differential equation need not be integrated directly. Instead, notice that, for an equilibrium magnetization distribution, $\frac{d\vec{M}}{dt} = 0$, which implies that the effective field, $\vec{H}_{eff}$, must be parallel to the magnetization $\vec{M}$. The magnetization configuration can be relaxed iteratively by positioning each magnetization vector (almost) along the effective field vector direction throughout the mesh. The initial condition can be selected to provide a head start for the iteration procedure. When the largest residual of a single value of

$\dfrac{\vec{M} \times \vec{H}_{eff}}{M_S \cdot \left| H_{eff} \right|}$ decreases below a pre-defined convergence minimum, the iteration process is stopped.

Chapter 3. Switching behavior of permalloy continuous film, discrete disk, and disk/film coupled structures

3.1 Introduction

The configuration of magnetization (M) distribution in any magnet is achieved by minimizing total energy originating from several competing origins: exchange energy, magnetostatic energy, magnetocrystalline anisotropy energy, Zeeman energy, etc [19-20]. The relative importance of each energy term depends on the size, shape, and material properties of the magnet. In the submicron size regime, each energy contribution is of comparable magnitude. Therefore, small variations in geometry can shift the energy balance remarkably, leading to a great variety of interesting configurations with distinct reversal properties [12]. This chapter focuses on the reversal behavior of Permalloy (Py) ($Ni_{80}Fe_{20}$), a soft magnetic material with negligible magnetocrystalline anisotropy. With three geometries of increasing complexity, from continuous thin film to discrete disks to disk/film sandwiched structure, the same material can be engineered to display completely different switching characteristics upon field reversal.

3.2 Experiments

Schematics of sample geometries are shown in Figure 3.1. The substrate is 50 nm thick low-stress amorphous silicon nitride membrane, which is strong and electron transparent, and ideal for transmission electron microscopy study. Specimen materials are deposited by the home-assembled UHV electron beam evaporation system (base pressure 10^{-10} Torr, deposition rate 1 Å/s for Py, 0.2 Å/s for C), in the form of polycrystalline thin film. A shadow mask is employed for disk array fabrication. During the final step, all the specimens are covered with 1 nm of C cap layer to prevent oxidation.

Magnetic imaging was performed using *in-situ* Lorentz transmission electron microscopy technique (L-TEM). In-plane magnetic field is generated by two methods: exciting coils in a custom-made magnetization stage, or tilting the sample in the vertical field of the objective lens. The first method is performed in JEOL 2100F-LM dedicated field-free Lorentz Microscope, with in-plane field up to 90 Oe generated by the magnetization holder. The second method is performed in JEOL 3000F standard TEM with objective lens turned on, of which the magnetic field is along the TEM column and pre-calibrated as a function of lens excitation. With different combinations of lens voltage (or excitation) and tilting angle, the maximum field available is much stronger than the first method. Accuracy of attainable field values is largely limited by the step size of TEM goniometer (0.1 degree).

Bulk magnetic moments and hysteresis curves of the same samples are also measured with SQUID magnetometer for comparison.

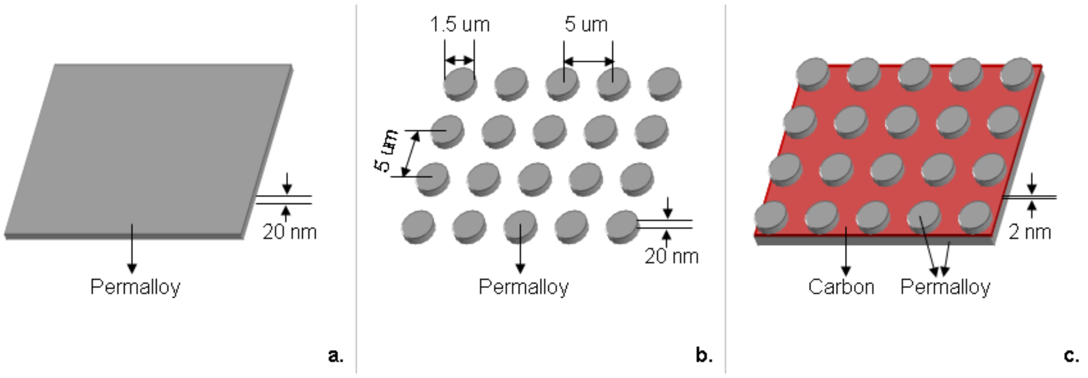

Figure 3.1 Geometries for three kinds of samples
Sample a is continuous Py film with thickness of 20 nm. Sample b is Py disk array. Each disk has diameter of 1500 nm, thickness of 20 nm, and is arranged in a square array with center-to-center separation of 5000 nm. Sample c is a Py-C-Py sandwiched structure, a combination of the two. The top layer is same as sample b, while the bottom layer is same as sample a. They are separated by the C spacer layer in the form of continuous film with thickness of 2 nm.

3.3 Results and Discussion

3.3.1 Continuous Permalloy film

For 20 nm thick continuous Py thin film, reversal is achieved by magnetization rotation and domain wall (DW) propagation process.

In Fresnel mode Lorentz images, local orientation of $\vec{M}$ distribution can be derived with the help of DWs [21]. However, this method fails if magnetic field is so strong that all DW features are wiped out. In this case, ripple contrast will provide very useful clue [22-24]. The origin of ripple can be attributed to magneto-crystalline anisotropy forces, which vary randomly in direction from grain to grain in a polycrystalline thin film. The magnetization does not follow these local wanderings of the direction of minimum anisotropy energy, but because of exchange coupling, which tends to straighten the path of $\vec{M}$, follows the mean easy axis averaged over a number of crystallites. There are two basic ripple components: longitudinal, in which the wavefronts of the fluctuations of the magnetization direction are perpendicular to the mean magnetization M_0, and lateral or transverse, in which the wavefrounts are parallel to M_0. A schematic illustration of these two ripple components is given in Figure 3.2. Since the volume pole density is very small for longitudinal ripple but not for transverse ripple, and since the two are equivalent with respect to exchange, random local anisotropy, and uniform forces, the dominant contribution to the magnetization ripple should be longitudinal. Therefore, for Lorentz microscopy, local direction of $\vec{M}$ can be derived to be perpendicularly oriented with respect to the direction of ripple contrast.

An experimental example is shown in Figure 3.3, where each sub-area of the specimen is imaged at higher magnification to reveal the ripple contrast. Although we can determine the direction of average magnetization to be perpendicular to ripple direction, there are still two possible orientations for the $\vec{M}$ vector in each direction. This uncertainty can be further removed by considering the initial saturation direction and preceding moments during reversal sequences. In the bottom left image, it is clear that DW here is 90 degree Neel wall, which is typical for thin film with such thickness [12].

Using the aforementioned method, we can follow the $\vec{M}$ distribution successively at each field value during a field-reversal process. One set of such observations, in comparison with SQUID measurement, is shown in Figure 3.4. Starting from saturation at 25.2 Oe, $\vec{M}$ is oriented along the field direction all over the sample. As the field decreases in magnitude and then reversed to -1.3 Oe, $\vec{M}$ rotates collectively and coherently, leading to the monotonous decreasing of bulk moment along the field direction. The speed of magnetization rotation is non-uniform over the sample area, because of local structural inhomogeneities such as different types of defects. As this speed difference grows, single domain will finally break up into several smaller domains separated with DW, when magnetic field reaches the nucleation point. Comparing the images of -1.3 Oe and -6.3 Oe, it is evident that a new domain was formed in bottom right corner of the specimen, with the magnetization 90 degree oriented relative to previous direction. Thereafter, the field continues to increase in the opposite direction, and magnetic reversal is achieved by both $\vec{M}$ rotation and DW propagation mechanisms. DW propagation is more sensitive to the field change than rotation process. This effect is evident in images from -6.3 Oe to -8.8 Oe, when the domain pattern changes dramatically while M direction in each domain is just slightly varied. Finally, at -25.2 Oe, all the magnetization is again aligned parallel to the external field, as a single domain, and the reversal is complete.

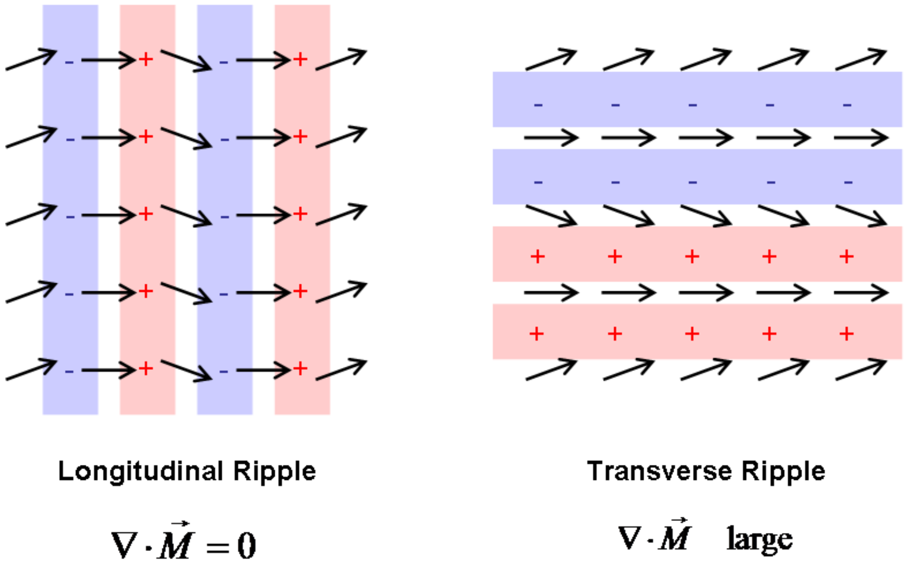

Figure 3.2 Schematic illustration of longitudinal and transverse ripple configurations and their volume poles

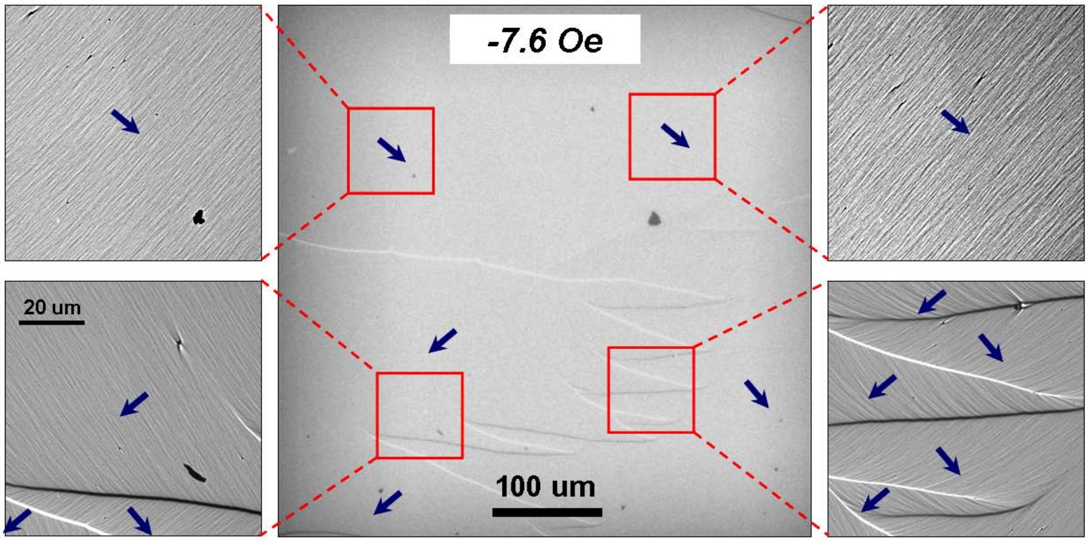

Figure 3.3 Determination of local magnetization direction in different areas by ripple contrast in higher magnification Lorentz image.

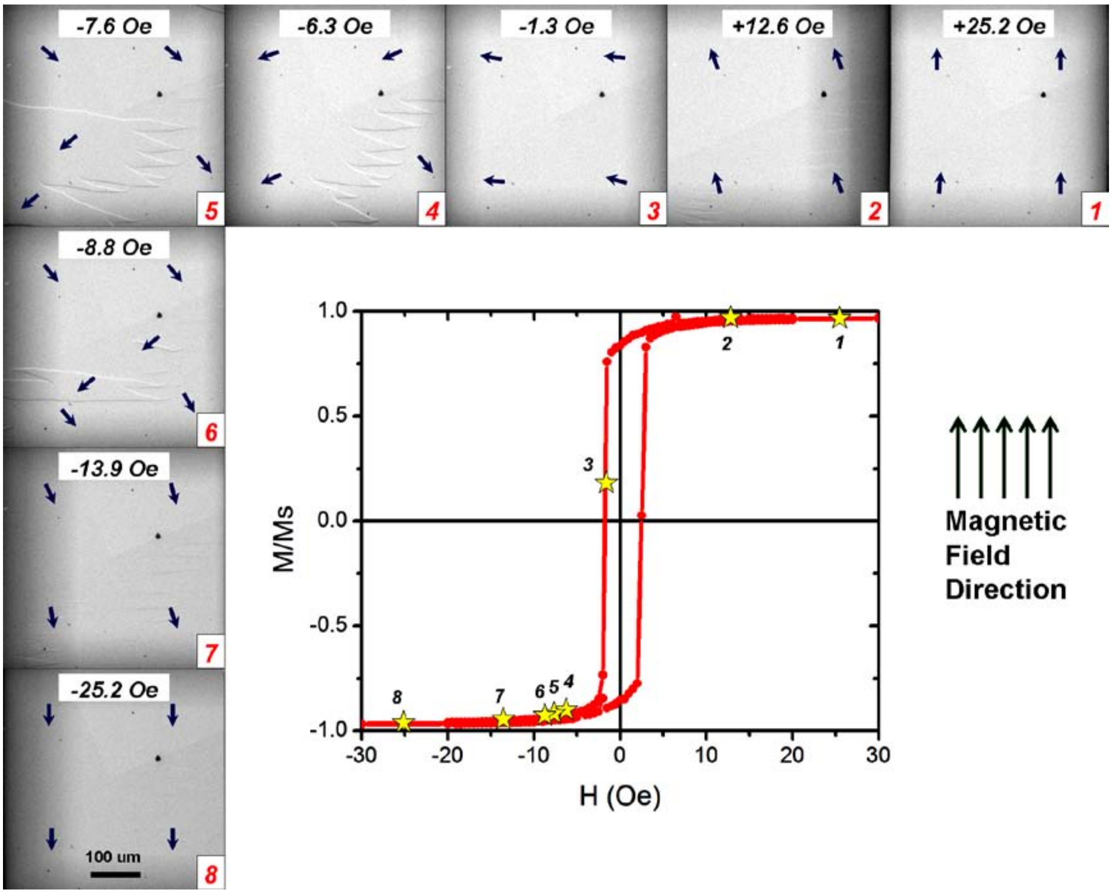

Figure 3.4 PY thin film dynamics in response to an applied in-plane field
Hysteresis curve is measured by SQUID. Magnetic field is applied along sample plane in the direction as shown on the right side. Top and left side pictures are low magnification Lorentz images showing the magnetization distribution at various applied field, corresponding to different stages during the field reversal process, successively from image 1 to image 8.

3.3.2 Patterned Permalloy disk array

For 20 nm thick Py disk array of 1500 nm diameter and 5000 nm separation, the reversal mechanism is dominated by vortex nucleation, propagation and annihilation processes [20].

Here geometric confinements from the disk shape play a leading role in determining its unique domain configurations. When disk size is relatively large (more than tens of micronmeters), the demagnetization energy dominates, and the elements show multi-domain configurations. When disk size is very small (less than 100 nanometers), the exchange interaction dominates, and the elements assume a single-domain state where all the spins are directed in the same orientation. In between these two extreme cases, one can usually find the element in so-called magnetic vortex states [25-26]. Inside such a vortex structure, $\vec{M}$ is arranged in closed loops with a core area in the center where $\vec{M}$ is tilted out of plane. No free poles exist in the disk boundary and stray field is thus reduced. But compared to single domain state, exchange energy is increased, notably in the core area. The exchange energy of the vortex state has a weaker dependence on disk diameter than does the magnetostatic energy of the single-domain state. Therefore a sufficiently large disk favors vortex state as in our case. In Lorentz images, one can always find two kinds of vortex states, with bright or dark center spots, corresponding to the two possible circulation directions (chiralities) of magnetization relative to the center [Figure 3.5].

Figure 3.6 depicts the response of a Py circular disk to an applied magnetic field. Starting from step 1, the Py disk is saturated and in single-domain state. As field is decreasing, the magnetization is slowly curved, and the single-domain state evolves into so-called S state, with $\vec{M}$ strongly curved at two edges (step 2). When field reaches a nucleation point, the magnetization in some area along the boundary is curved so much that a vortex is created (step 3). This vortex can be formed on either side of the disk where there’s maximum curving. Once one vortex is formed, the chance for the formation of the other one is greatly suppressed. In our experiment, the case when two vortices coexist inside single disk is never observed. Relating to the hysteresis curve, this nucleation event corresponds to a sudden jump in the magnitude of the overall magnetization. From step 3 and later, the vortex core is propagating as the field is changing. The portion of the vortex with spins parallel to the field expands, and so the vortex is moving perpendicular to the field direction. The overall magnetization is changing continuously along with this vortex movement, from step 3 to step 6. In step 7, the vortex is annihilated at the disk side, and the disk returns to single domain state again with M pointing to the opposite direction.

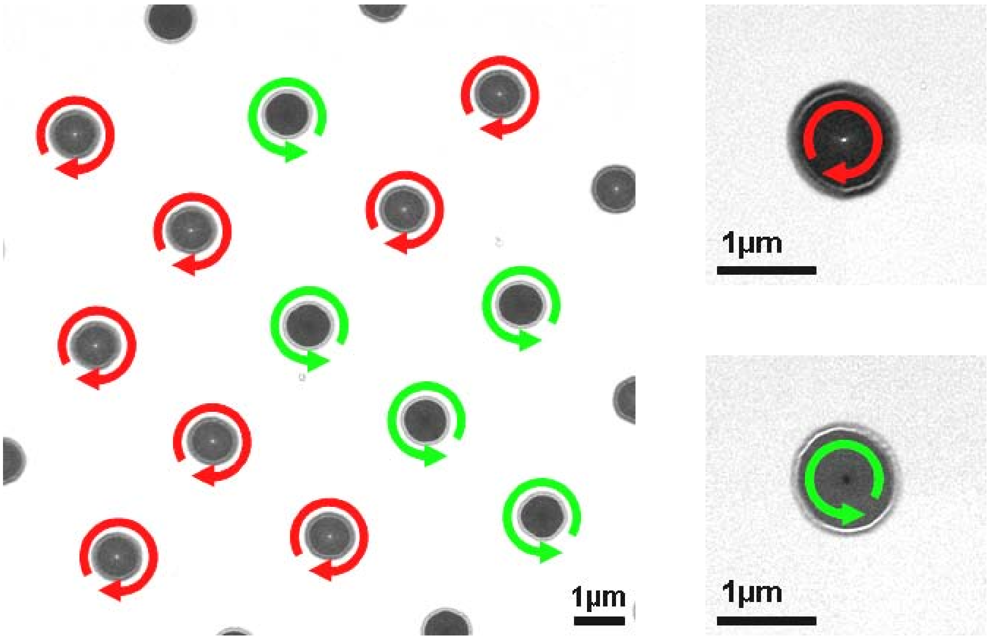

Figure 3.5 Lorentz micrographs of the remanent state of a Py disk array with 1 micron diameter and 20 nm thickness.

The red/green arrow indicates chirality, or in-plane magnetization circulating direction, as also shown in the blowup images on the right side.

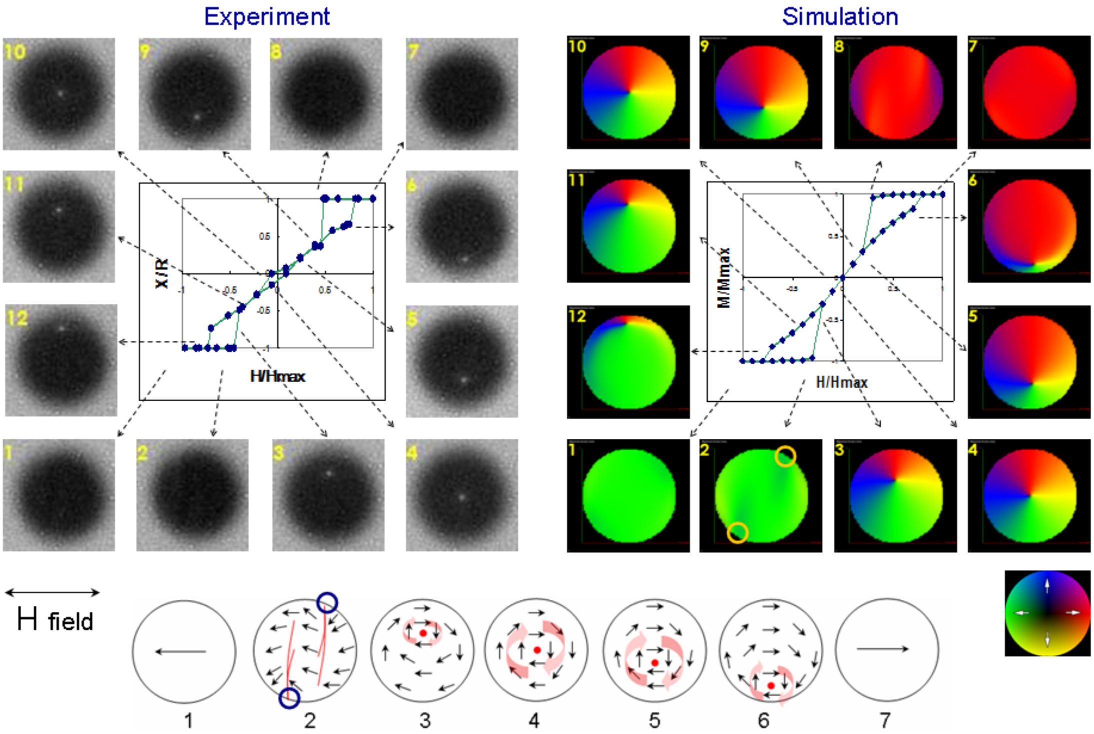

Figure 3.6 Py thin film disk dynamics in response to an applied in-plane field
Magnetic field is applied along sample plane in the direction as shown on the bottom left corner. Left side pictures are Lorentz images of different stages during the hysteresis cycle. Right side pictures are obtained from LLG micromagnetic simulation for the same sample parameter and field conditions. The color wheel represents the relation between color and magnetization direction. The quantization is set to be 512×512×1 to accommodate the computing capability. Bottom cartoons represent the evolution of M distribution.

3.3.3 Permalloy disk/film sandwiched structure

For Py disk/film sandwiched structure, reversal is driven by continues rotation of the sharp magnetic spikes in the film near the disk edge.

Figure 3.7 shows the remnant state domain structure, where a unique “spike-type” domain wall structure is observed. This feature exists in the bottom continuous Py thin film layer, of several micron meters in size, and the bright and dark wing is always arranged in the same orientation for each disk. These uniformities were preserved all over observable sample area.

The origin of the formation of this spike-type domain wall, as we believe, is due to roughness-induced ferromagnetic coupling (the so-called “orange peel effect”) [27]. As shown in Figure 3.8, when the spacer layer is thin compared to the amplitude of the surface corrugations of the magnetic films, the roughness of the two magnetic layers are strongly correlated. Along the interface, the magnetic dipole interaction will favor the alignment of $\vec{M}$ in a peak of one layer with $\vec{M}$ in an adjacent trough in the other layer. The resulting magnetostatic coupling is analogous to permanent magnets in a line favoring an arrangement wherein opposite poles are next to each other and the $\vec{M}$ ’s are all parallel.

For disk/film coupled system, the strong ferromagnetic interlayer coupling can lead to complex domain configurations. We first assume vortex domain is preserved in top disk layer. If the magnetization $\vec{M}$ at bottom layer strictly follows that of the top disk, a “mirror” vortex would be induced in the bottom thin film. This is however an unrealistic scenario because of two reasons. First, inside the continuous thin film, a vortex can extend infinite far and cost enormous energy. Second, if multiple vortices are arranged in a two dimensional array, it would create a frustrated system because boundary condition requirements between neighboring vortices are impossible to be fulfilled consistently.

Our model (Figure 3.9) is that the top disk layer will take a curved single domain structure, in which majority of magnetization will point to one direction, except that the magnetization near the boundary will be tilted along the periphery to minimize demagnetization field. This curved single domain will accumulate magnetic free poles at two ends of the disk. This pole accumulation can be compensated by free poles of opposite sign induced in the bottom layer, via the formation of observed spike-type domain wall. In addition, when the size of the spikes is comparable with the inter-disk spacing, neighboring entities will interact strongly to achieve observed uniformity.

To test the validity of this model, the ground state magnetization distribution for the composite system is calculated by LLG micromagnetic simulator. The structure follows the actual dimensions of our sample, and is relaxed from saturation along $+x$ direction under zero field. Results for separate layers are shown in Figure 3.10 (a) and (b). The calculated magnetization distribution confirms our former speculation that vortex state is not present here, whereas a quasi single domain (SD) state is favored instead inside the disk. This domain structure is very similar to SD configuration, except that the magnetization close to the edge is curved along the boundary. Note that SD configuration is never stable in isolated disks within micron meter size regime, because strong stray field generated from the two end of the disk dramatically increases demagnetization energy. However, it can be stabilized in our system by inducing proper magnetization curving in bottom Py layer, effectively creates a “closed loop” to decrease demagnetization energy of the composite system. This mechanism is even more clear if magnetic volume charge ($q_m = -\nabla \cdot \vec{M}$) distribution for both layers is calculated, as shown in Figure 3.10 (c) and (d), where we find that opposite sign of charges is accumulated in the almost same x-y positions, and stray field can therefore be effectively suppressed. Furthermore, we can simulate the corresponding Fresnel contrast originating from the magnetic potential and compare it with experimental image [13, 28-30]. As a first order approximation, disregarding the microscope parameters such as defocus and aberration, the Fresnel contrast can be qualitatively interpreted as out of plane component of the curl of magnetization along the electron trajectory, i.e., $(\nabla \times \vec{M}) \cdot \vec{e}_z$. The result is shown in

Figure 3.10 (e), and is in good agreement with the experimental image Figure 3.10 (f), with most of the key features nicely reproduced. Note that the experimental image has a darker disk region compared with simulation, and this is due to enhanced scattering from electric inner potential in thicker sample region [29]. We did not take into account this effect in our image simulation.

The dynamic magnetic reversal process is shown in Figure 3.11. Upon field sweeping, the reversal is dominated by rotational switching. The spike-pair domain wall is oriented perpendicular to the field direction when field is strongest. It then rotates continuously during switching, and there's a 180 degree flipping when field changes from one maximum to other maximum in opposite direction. At certain field ranges, we also find cross-tie type domain wall presented in the sample, which propagate very rapidly and cause fast rotation of the spike-pairs.

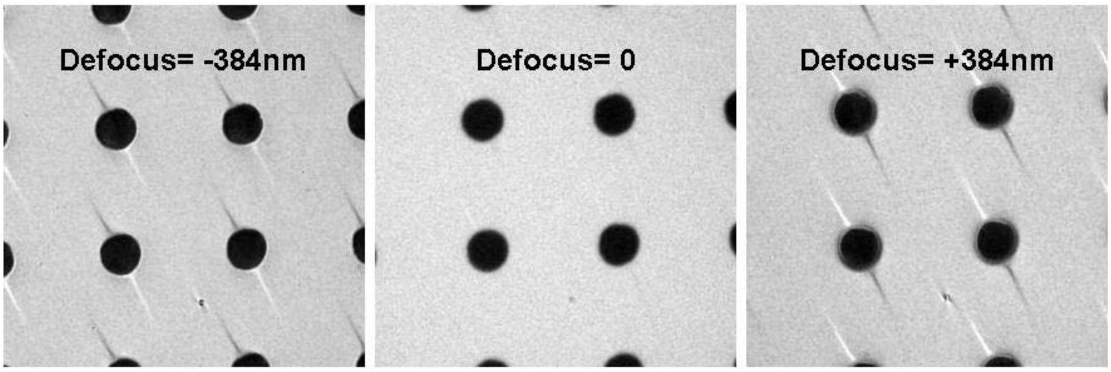

Figure 3.7 Lorentz micrograph of the remanent state of Py disk/film hybrid system. Disks are 1500 nm in diameter and 5000 nm separated from their neighbors. Bright and Dark contrast flips for opposite defocus value, while disappear at in-focus position, confirming its magnetic phase contrast origin.

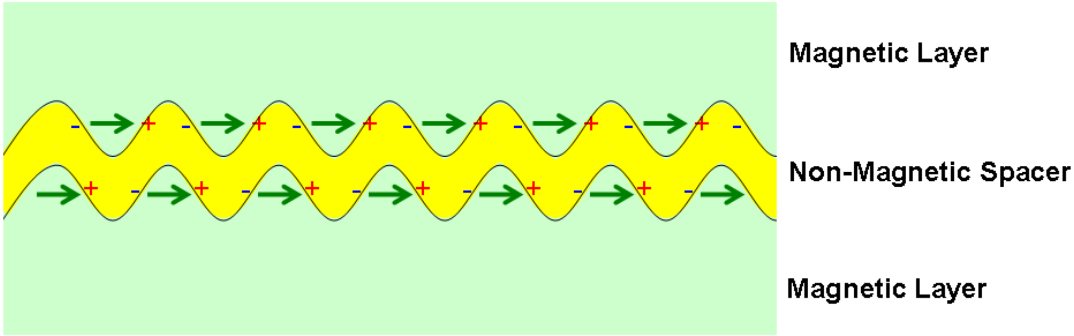

Figure 3.8 Schematic illustration of the “orange-peer effect”: ferromagnetic coupling arises from correlated roughness between two magnetic layers.
The green arrow indicates magnetization vector at the interface, while the +/- signs correspond to magnetic free poles.

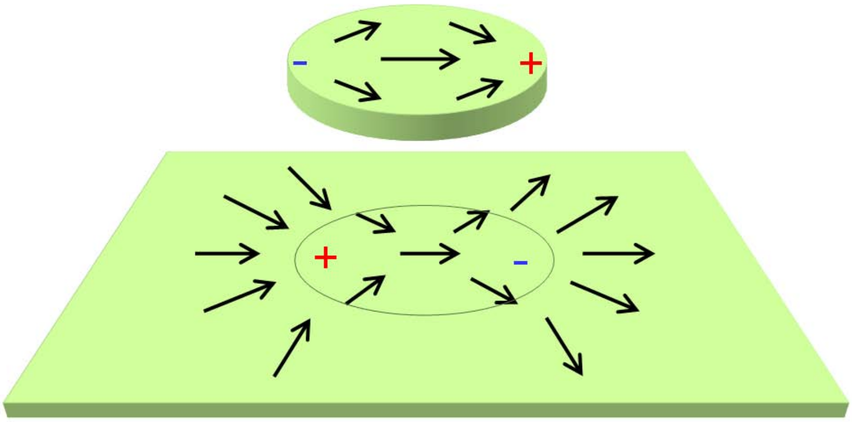

Figure 3.9 Schematics of the model of magnetization configurations within disk and film layer in a disk/film coupled system.

The black arrow indicates magnetization vectors, while the +/- signs correspond to magnetic free poles.

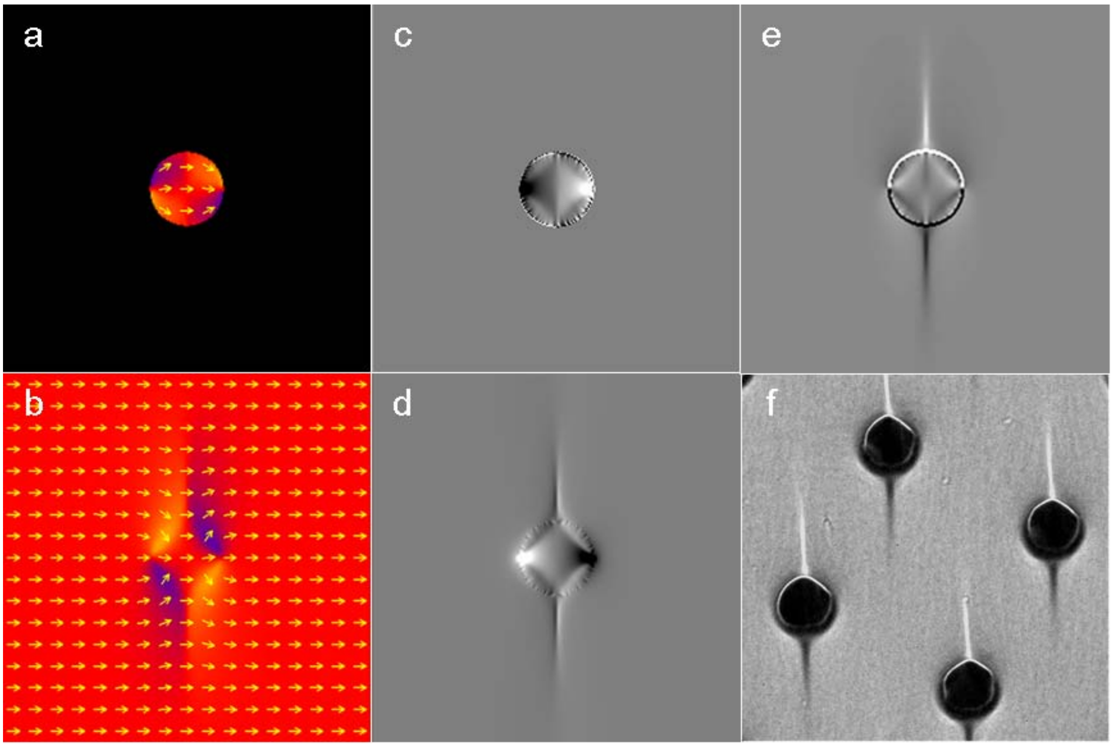

Figure 3.10 Micromagnetic calculation and Lorentz contrast simulation of the disk/film hybrid system

Vector presentation of magnetization distribution is shown for disk (a) and thin film (b) layer at remnant states. Gray scale graph of calculated magnetic volume charge ($-\nabla \cdot \vec{M}$) distribution is shown for disk (c) and thin film (d) layer. White and black contrast corresponds to positive and negative volume charge respectively, and intensity is proportional to charge density. Gray scale graph of calculated $(\nabla \times \vec{M}) \cdot \vec{e}_z$ is shown in (e), and contrasts from both layers are added together. Experimental Lorentz images of remnant states is shown in (f).

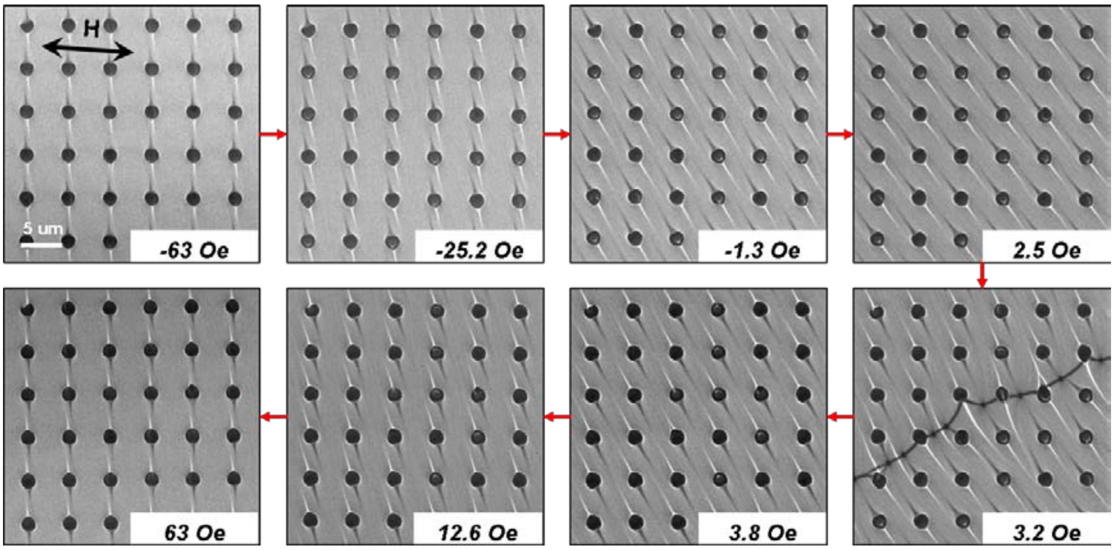

Figure 3.11 Lorentz images at different applied fields during one hysteresis cycle, recorded consecutively as indicated along red arrow direction. Magnetic field is applied along horizontal direction.

3.4 Summary

In conclusion, we have used *in-situ* Lorentz microscopy technique assisted by bulk measurement to investigate the microscopic magnetic reversal process of thin film Py samples with three distinct geometries, namely, continuous thin film, patterned disk array, and disk and film sandwiched with a nonmagnetic carbon spacer layer. We find that different geometric structures of the same material result in completely different reversal mechanisms. For the continuous film, when field is reduced from saturation, the switching behavior consists of coherent magnetization rotation and domain wall propagation. In contrast, for the patterned disk array, it is dominated by magnetic vortex nucleation, propagation and annihilation. The switching behavior of the sandwiched Py is most intriguing with continuous rotation of the sharp magnetic spikes in the film near the disk edge when the field amplitude is altered while its direction remains the same. We provide our explanation based on interlayer magnetic dipole coupling and a model that is qualitatively verified by micromagnetic simulation. Our studies clearly confirm the feasibility of tailoring magnetic switching properties by making use of geometric confinement and interlayer coupling.

Chapter 4. Controlled Magnetization Reversal in Shape-Engineered F/N/F trilayers

4.1 Asymmetric Ring

4.1.1 Introduction

Recently, intense research efforts have been devoted to the study of ring shaped pseudospin valve (PSV) elements, which hold great promise for the development of next generation magnetic memory devices [31-32]. With the removal of the high energy core in the central area, magnetic ring structures could stabilize a stray-field-free vortex state down to much smaller sizes than planar disk structures, enabling substantially increased data capacity [6, 33]. However, a magnetic ring does not always relax to a vortex state at remanence due to the fact that it can go through either vortex formation or bi-domain rotation processes upon magnetization reversal. This bimodal relaxation stability is intrinsically related to the geometric symmetry of the ring structure, and poses a severe problem for its practical application. As a possible solution, Zhu *et. al.* proposed using an asymmetric ring structure, which enables 100% vortex-based magnetization reversal probability if the external field was applied perpendicular to the structure's symmetry axis [34]. This is realized by using shape anisotropy to force two 180° head-on domain walls to move towards each other during the initial stage of reversal, with subsequent annihilation to form a vortex. Similarly, such an asymmetric design can also be used in layered PSV structures. If the vortex formation process can be effectively controlled individually within the two magnetic layers, distinct current-perpendicular-to-plane (CPP) resistances of the PSV cell may be achieved to directly encode bits of information. In this regard, dedicated studies of the magnetization reversal behavior of PSV structures with asymmetric ring design, specifically, knowledge of actual physical processes occurring within each magnetic layer, are of great importance.

Up to now, reversal studies of PSV ring elements have been primarily relying on indirect means, including hysteresis loop and Magneto-resistance measurements, while layer-resolved real space observation remains scarce [35-38]. This can be attributed to the fact that most magnetic imaging techniques either have only surface layer sensitivity, or cannot easily separate the contribution of different magnetic layers from an overlapped signal [7]. In this work, we report our *in-situ* observation of the magnetization reversal process for individual Py/Al/Py asymmetric ring PSV elements using off-axis electron holography. Detailed magnetization reversal behavior in the two magnetic layers was captured and identified with the help of micromagnetic simulations. At various stages during the hysteresis cycle, the phase shift measurements from electron holography experiments were quantitatively compared with analytical calculations[39] to verify the spin configuration.

4.1.2 Experiments

The specimen (Figure 4.1) consists of Py/Al/Py trilayer ring PSV elements. The cross section of the stack adopts the shape of an asymmetric ring with 1000 nm inner diameter and 1600 nm outer diameter. The maximum and minimum ring widths are 400 nm and 200 nm, respectively. Samples were patterned on 50 nm thick amorphous Si_3N_4 TEM supporting membranes using standard electron beam lithography with PMMA resist [40]. Ti/Py/Al/Py/Al (3 nm/20 nm/20 nm/10 nm/3 nm) was electron beam evaporated at a base pressure better than 5×10^{-7} Torr and evaporation rates of less than 1 Å/s. The 3 nm Ti seed layer was used to enhance surface adhesion to the Si_3N_4 substrate, while the 3 nm Al capping layer was used to protect the structure from oxidation. Electron holography experiments were carried out using a 300 kV JEOL 3000F TEM. The objective lens was slightly excited at a constant voltage, and in-plane magnetic fields between ±1200 Oe were generated by changing the specimen tilt [41-42]. With specific lens settings, nanometer-scale spatial resolution and up to 2.5 μm field of view can be routinely achieved in our electron holography experiments.

Details of electron holography techniques, especially its application to the study of magnetic nanostructures, can be found elsewhere [43]. After image-wave reconstruction from recorded holograms, the obtained electron-optical phase shift φ contains both electrostatic (φ_e) and magnetostatic (φ_m) components, and is expressed by the Aharonov-Bohm equation:

$$\varphi = \varphi_e + \varphi_m = C_E \int V dz - \frac{\pi}{\phi_0} \int A_z dz \qquad (4\text{-}1)$$

where $C_E = 6.25 \times 10^{-3}\ V^{-1}\ nm^{-1}$ for 300keV electrons, V is the electrostatic potential, $\phi_0 = \frac{h}{2e} = 2.07 \times 10^3\ T\ nm^2$, and A_z is the z component of the magnetic vector potential. The integral is performed along the incident electron beam direction. The electrostatic phase shift φ_e is determined by local variation in the mean inner potential and the thickness of the specimen, and is independent of the magnetostatic component of interest. Therefore, it was first extracted from a pair of oppositely saturated phase images, and then digitally removed from the overall phase shift obtained in subsequent electron holography experiments [15]. The remaining magnetostatic phase shift, φ_m, can be used to generate contour maps, where the spacing and distribution of the contour lines reveal the magnitude and distribution of the projected flux from the magnetic layers [Appendix B].

4.1.3 Results and Discussion

While dozens of rings were inspected, Figure 4.2 illustrates as an example the detailed magnetization reversal process of an individual element recorded from our experiments. The in-plane component of the magnetic field was applied perpendicular to the symmetric axis, as indicated by the arrows. The element was first saturated along one direction by tilting the specimen to 20º (equivalent to an applied field of 1206 Oe). Both Py layers were in bi-domain onion states when the field was reduced to 460 Oe [Figure 4.2 (A)], which was characterized by two uniform domains parallel to the field direction, separated by two 180º head-on domain walls. The dipolar stray field generation from the strongly magnetized element is clearly visible. From Figure 4.2 (A) to Figure 4.2 (C), as the field was reduced to 43 Oe, the double-onion domain combination was preserved across the element. The emergence of flux closure in the two domain wall regions, however, implied the local transformation of the wall structure from a transverse wall to a vortex domain wall [44]. A transverse wall, which was formed reversibly from saturation, was the first accessible energy minimum when field was relaxed. The subsequent formation of the vortex wall, which has lower total energy by reduction of the stray field, was activated by the nucleation of a vortex core from the outer edge of the element. Then, at 0 Oe [Figure 4.2 (D)], the domain wall regions disappeared and the element presented a flux-closure arrangement. At this point, both Py layers had evolved into vortex states with clockwise chirality. We observed that the domain walls of the onion state moved towards the thinner ring width, and subsequently annihilated to induce the onion-to-vortex transition. This relaxation behavior is explained by the fact that the domain wall free energy increases with the area of cross-section, so that the asymmetric ring presented a continuously varying shape anisotropy that drives both walls towards the narrowest part [34]. The difference between the critical transition fields of the two Py layers was found to be no more than 20 Oe. At -129 Oe [Figure 4.2 (E)], dramatic change was noticed for contour spacing in the wide arm of the ring, which was caused by the vortex-to-onion transition occurring in the 10 nm Py layer. For such an onion/vortex domain combination, the magnetizations in the two Py layers were oriented oppositely in the wide arm region, leading to 67% reduction in the magnitude of the projected flux. At -160 Oe [Figure 4.2 (F)], a vortex-to-onion transition in the 20 nm Py layer was activated, enabling a double-onion domain combination reversely oriented compared with Figure 4.2 (C). Thereafter, the element was further magnetized [Figure 4.2 (G)] until saturation. The same magnetization reversal sequences were also observed for the reverse branch of the hysteresis cycle [Figure 4.2 (H) to Figure 4.2 (N)].

To analyze the measured phase shifts quantitatively, analytical calculations were performed for four distinct domain configurations, i.e., double-onion [Figure 4.2 (C)], vortex-onion [Figure 4.2 (D)], double-vortex [Figure 4.2 (E)] and double-onion-reversed [Figure 4.2 (F)] configurations, where, first, Micromagnetic simulations were carried out for the PSV structure, as shown in Figure 4.3. The calculated hysteresis loop clearly shows three jumps in each branch. In the top branch for example, the 0 Oe jump is associated with the onion-to-vortex transition for both Py layers, while the -125 Oe and -200 Oe jumps are associated with the vortex-to-onion transition for 10 nm Py and 20 nm Py layers, respectively. Thus the four states corresponding to Figure 4.2 (C)-(F) were identified, from which the detailed spin configurations (including both Py layers) were extracted from the simulation results [Figure 4.3 (C’), (D’), (E’) and (F’)]. Based on this, the magnetic vector potential was calculated using a Fourier-transform-based approach [39], and the projected magnetostatic electron-optical phase shift was derived analytically using the Aharonov-Bohm equation. Note that no fitting parameters were used throughout our calculations, where the detailed comparison between experiments and calculation is illustrated in Figure 4.4. The excellent match obtained for all four studied domain configurations unambiguously demonstrates that the underlying spin configurations in the PSV multilayer structure have been quantitatively retrieved with high spatial resolution in our electron holography experiments.

4.1.4 Summary

To summarize, we have used an integrated approach including off-axis electron holography, micromagnetic simulation and analytical calculation to study the magnetization reversal process of asymmetric-ring shaped PSV structures. Previously suggested controlled domain wall motion in asymmetric ring structures were directly confirmed, and a double-vortex configuration was observed at remanence. The two Py layers with different thickness have similar onion-to-vortex transition fields, but very distinct vortex-to-onion transition fields. Our findings pave the road for further studies towards controlled magnetization reversal process using asymmetric ring shaped PSV designs to obtain specific remanent domain structures. Moreover, the experimental techniques and data analysis methods described in this work can also be applied to the characterization of other patterned multilayer structures to resolve the layer-by-layer magnetic behavior as a function of applied external field.

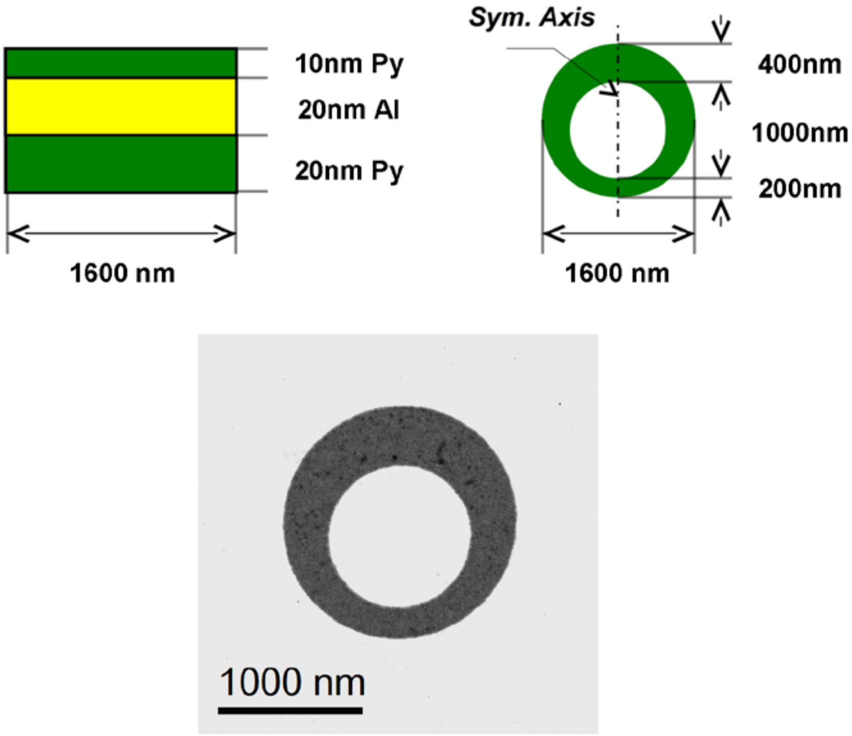

Figure 4.1 Schematic design and plan-view TEM bright field image of patterned Py/Al/Py PSV ring structure.

Top panel shows the side-view and top-view of specimen design, respectively. Bottom panel is a bright field TEM image.

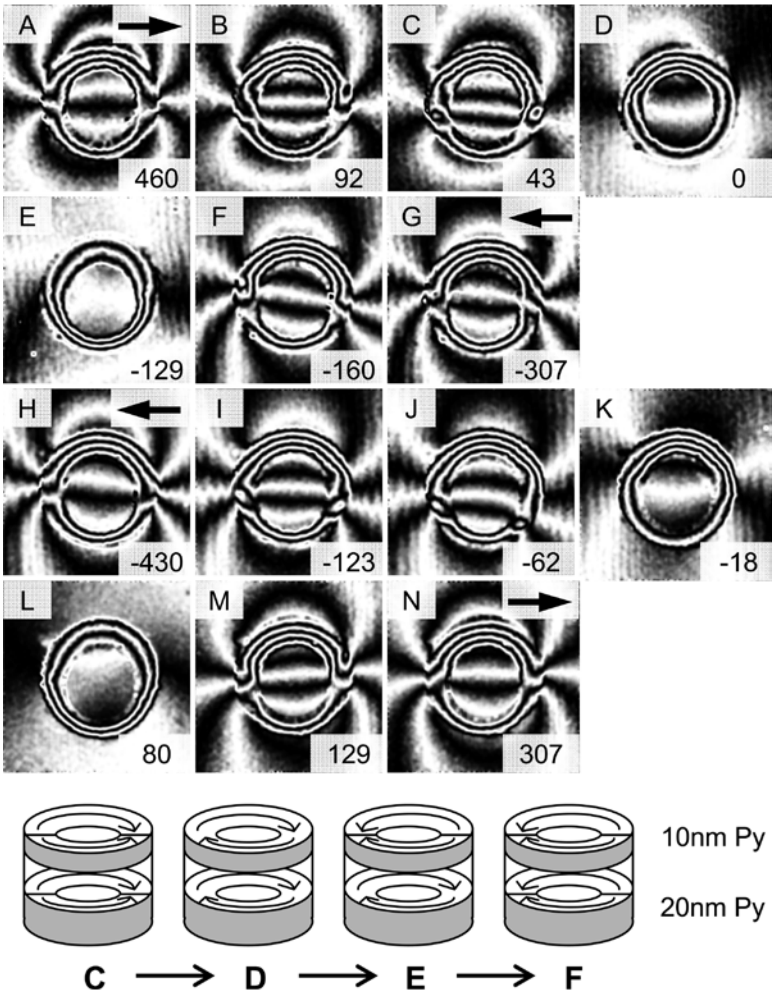

Figure 4.2 2× amplified phase contour images during a full hysteresis cycle.
In-plane field was applied perpendicular to the symmetric axis of the ring, as shown by the arrows in (A), (G), (H) and (N). Field values are indicated in Oersted. (A)-(G) and (H)-(N) correspond to the two branches of the hysteresis cycle. Schematic drawings of the detailed domain configurations in the two Py layers corresponding to (C), (D), (E), and (F) are shown in the bottom panel.

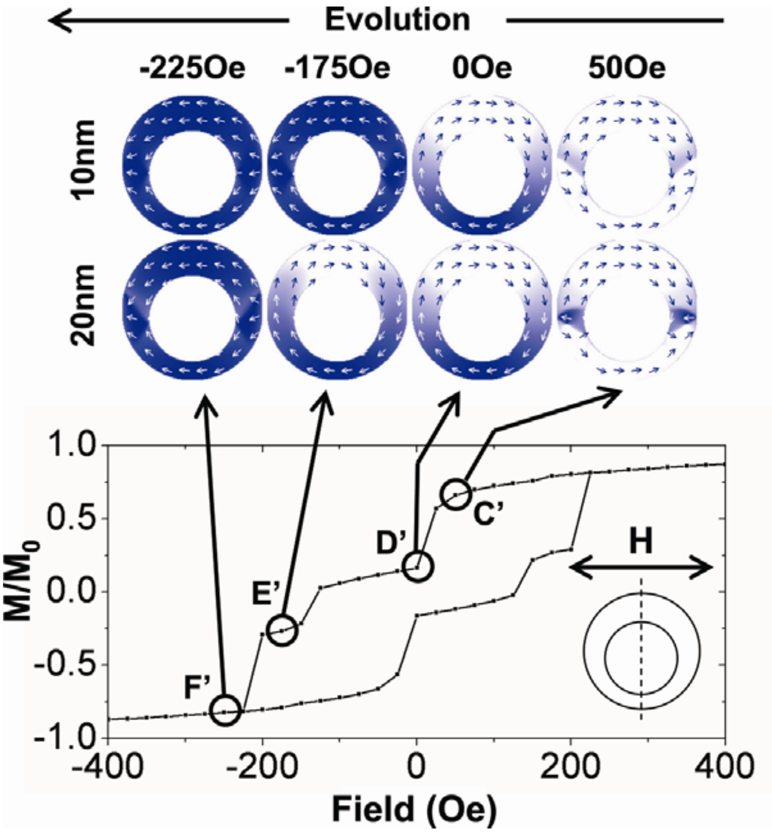

Figure 4.3 Simulated hysteresis loop of the asymmetric ring PSV structure.
LLG Micromagnetic simulator™ with default material parameters (saturation magnetization Ms= 8×10^5 A/m, exchange stiffness constant C=1.3×10^{-11} J/m, magnetocrystalline anisotropy coefficient=0) was employed, and cell size 10nm×10nm×thickness was used for each Py layer. Al spacer was modeled as vacuum. The corresponding magnetization configurations of the two Py layers are shown at four representative fields (C', D', E', F').

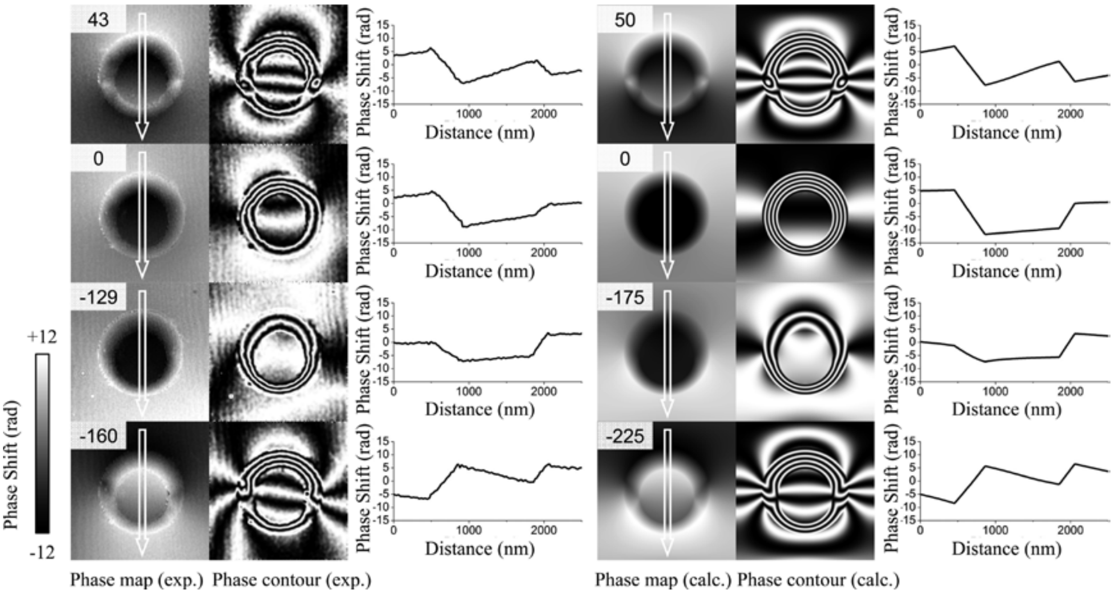

Figure 4.4 Comparison between experiments and calculations for four different types of domain configurations.

Experimental results correspond to Figure 4.2 (C), (D), (E), and (F), while calculations are derived from the simulated magnetization configurations [(C'), (D'), (E'), and (F') in Figure 4.3]. Columns from left to right correspond to: phase map (Exp.), 2× amplified phase contour (Exp.), phase shift line scan along symmetric axis (Exp.), phase map (Calc.), 2× amplified phase contour (Calc.) and phase shift line scan along symmetric axis (Calc.). The white boxed arrow inside each phase map indicates the sampling direction for the line scan.

4.2 Ellipses

4.2.1 Introduction

While studies of magnetization reversal usually focus on the magnetic domain structures, the switching of the spin configurations inside domain walls has recently attracted lots of attention [45-48]. In particular, Cheynis et. al. discovered that in elongated single-crystalline Fe(110) dots displaying a flux-closure state, the magnetization directions of the surface features of an asymmetric Bloch wall, known as Néel caps, can be controllably manipulated to achieve two possible antiparallel arrangements at remanence [45]. The reversal is driven by surface vortex translation upon application of an in-plane magnetic field which does not significantly alter the other two degrees of freedom found in the system: the perpendicular core magnetization of the Bloch wall, or the chirality of the in-plane flux-closure. Therefore, the Néel caps can be exploited as a new and unique degree of freedom to store bits of information, giving rise to an emerging class of domain-wall-based magnetoelectronic devices [49]. Although the epitaxial Fe dots of previous studies exhibit appealing properties, they are not suitable for practical device applications for two reasons. First, the symmetry breaking between the Néel caps at the top and bottom surfaces is induced by the inclined crystalline facets, which cannot be effectively modified during the fabrication process in order to control their switching characteristics. Secondly, these single-crystalline islands are grown by spontaneous self-assembly techniques, where it is impossible to prepare well-defined structures with uniform sizes and shapes [47]. With these issues in mind, it is technologically important to explore whether the aforementioned domain-wall reversal behavior can be realized in other types of device structures that have greater engineering flexibilities.

In this work we focus on patterned Py/Al/Py trilayer elements with in-plane elliptical shape. For single layer submicron Py ellipses, magnetization reversal occurs via nucleation and propagation of a single vortex when the magnetic field is applied along the short axis, where the critical switching fields for vortex nucleation and annihilation strongly depend on the geometric parameters, such as the ratio of major/minor axis and thickness of the patterned structure [19, 50-51]. At remanence, the elliptical element adopts flux-closure state, with two oppositely oriented Néel walls constrained along the long axis and connected by the vortex core. Therefore, by sandwiching two Py ellipses with a nonmagnetic Al spacer, the Néel walls in each magnetic layer can interact with each other through magnetostatic coupling, thus forming a composite wall system equivalent to the asymmetric Bloch wall of Fe (110) dots [Figure 4.5]. With such a design, the switching characteristics of the top and bottom Néel walls can be directly controlled by appropriately tuning the thickness of the individual Py layers. Moreover, such polycrystalline structures can also be easily prepared with high precision using standard thin film deposition and patterning techniques.

4.2.2 Experiments

The specimen consists of Py/Al/Py (15 nm/2 nm/30 nm) trilayer ellipses with major and minor axes of 4 μm and 1.28 μm, respectively. Samples were patterned on 100 nm thick amorphous Si_3N_4 membranes, standard support for transmission electron microscopy (TEM), using high resolution electron beam lithography with Polymethyl Methacrylate (PMMA) resist, followed by electron beam evaporation at a base pressure better than 5×10^{-7} Torr and evaporation rates of less than 1 Å/s. A 3 nm Ti seed layer was used to enhance surface adhesion onto the Si_3N_4 substrate, and a 3 nm Al capping layer was used to protect the structure against oxidation. Lorentz microscopy experiments were carried out using Brookhaven's 300 kV JEOL 3000F TEM in the Fresnel contrast mode [9, 51]. *In-situ* magnetization was performed by tilting the sample in a calibrated magnetic field of the objective lens [16]. Specifically, the objective lens excitation was fixed at 0.1 V, generating a 1480 Oe field along the optical axis, i.e., perpendicular to the sample. The tilt of the sample stage was varied between ±25° to change the in-plane component of the magnetic field.

4.2.3 Results and Discussion

Figure 4.6 shows a Fresnel image of an individual trilayer element at remanence, along with the simulated micromagnetic configurations for each Py layer. In the following discussions, subscript of “1” corresponds to the 15 nm Py layer (L1), and subscript of “2” corresponds to the 30 nm Py layer (L2). The image contrast of the Lorentz micrograph has been digitally inverted to improve visual quality. We find that the domain wall contrast consists of two dark spots (V1, V2) with a dark and straight line in between (W1+W2), and two bifurcated dark lines (W1’ and W2’). By comparison with micromagnetic simulations, V1 and V2 are identified as two vortices of the same chirality (counter-clockwise, CCW) formed in L1 and L2 respectively, with V2 darker than V1 due to thickness difference of the Py layers. The straight line which connects V1 and V2 corresponds to the overlapped Néel walls (W1+W2) of L1 and L2. Although W1 and W2 are magnetized in opposite directions (-y and +y direction, respectively), they both appear dark in the Lorentz image. This is because the contrast in a domain wall is due to the magnetization in the domains adjacent to a wall and not on the magnetization of the wall itself [9]. The bifurcated dark lines, on the other hand, correspond to two Néel walls of the same magnetization direction (-y direction). Again, due to the thickness difference of the Py layers, W2’ is darker than W1’.

There is, however, one problem associated with the above-mentioned calculations: here we used a cell size of 10 nm × 10 nm × thickness. As a rule of thumb, the cell size should be below the exchange length (for Py, this is about 7 or 8 nm.) in order for micromagnetics to paint an accurate picture. By using through-thickness cells in the simulation, we are forcing certain solutions along the Py-spacer interface that may or may not be realistic. To verify that these are exchange coupled Neel walls, more cells need to be considered along the thickness direction. We thus performed additional tests.

Because our sample is relatively large (4 μm × 1.28 μm × 47 nm), a full simulation using 7.5 nm × 7.5 nm × 7.5 nm cell size (or 7.5 nm × 7.5 nm × 2 nm for the spacer) would require at least 637200 cells in total, which exceeds the maximum memory capacity installed in our computing workstation. We therefore decided to fix the cell size (7.5 nm), thickness and element shape, and try the biggest element that can be handled by our computer: a 1.5 μm × 0.48 μm × 47 nm structure. The structure was divided in 7 layers along thickness direction, and the layer-resolved domain configuration for the remanent state was shown in Figure 4.7. Basically, for each of the Py layers, no significant rearrangement of domain structures at different thickness cross-sections was observed. Notebly, the domain configuration at the Py spacer interface appears the same as those located inside the Py layer. This test shows that using through-thickness cells does provide a reasonable approximation to the realistic spin configurations.

The above observations clearly suggest that two magnetostatically coupled Néel walls tend to trap each other if the wall magnetizations are aligned anti-parallel, and expel each other when aligned parallel. This phenomenon can be qualitatively understood by considering the interaction energetics of two magnetic dipoles. Analogous to two Néel walls in a trilayer structure, we assume two horizontally oriented magnetic dipoles, with one positioned at the origin and the other positioned at a fixed vertical height d but variable horizontal displacement y [Figure 4.8]. The total energy is thus given by:

$$E = \pm \frac{\mu_0 m^2 (d^2 - 2y^2)}{4\pi (y^2 + d^2)^{5/2}} \tag{4-2}$$

where μ_0 is the vacuum permeability, m is the magnetic moment of a single dipole, and ± sign correspond to parallel and anti-parallel arrangement of the two dipoles, respectively [52]. For anti-parallel arrangement, a symmetric potential well centered at zero displacement ($y = 0$) is formed, indicating that the lowest energy configuration is obtained by placing one dipole directly above another. For parallel arrangement, on the other hand, the shape of energy curve is inverted, and the lowest energy configuration is obtained by shearing the two dipoles horizontally, with respect to each other, to a lateral separation of $y = 1.22d$ (with $dE / dy = 0$). To calculate actual wall separation, on the order of a micron, rigorous energy calculation which includes all spin vectors presented in the system is required. The two-dipole model, on the other hand, only considers the magnetostatic interaction between the two Néel walls. It is worth noticing that this expelling behavior is strongly suppressed for Néel caps with parallel orientation in a single layer element, in which case they are brought together by the Bloch wall (white arrows in Figure 4.5).

Additionally, we directly observed the domain-wall switching process by application of *in-situ* fields directed along the short axis (y direction as defined in Figure 4.5) of the element, as shown in Figure 4.9. We begin by applying a field of 338 Oe. Due to the CCW flux closure in both layers (as shown in Figure 4.6), this field pushes both vortices to the left end of the element, which constitutes a single dark spot in the Fresnel image of the figure. The Néel wall magnetizations in both Py layers are aligned with the external field to form the (+, +) state, referring to the domain wall orientation in L1 and L2, respectively, relative to the +y direction. When the field is decreased to -18O e, one vortex moves to the right, while the other one remains in its initial position. The mobile vortex, having darker intensity, indicates that it corresponds to V2. This is consistent with previous findings that thicker elements have higher vortex nucleation critical field [19]. In addition to the vortex movement, a straight line (W1+W2 as defined in Figure 4.6) forms between the two vortices, induced by the strong trapping effect between the two anti-parallelly oriented Néel walls of two Py layers. Still referring to Figure 4.9, at about -72 Oe, the straight line is stretched to its longest length, constituting the (+, –) state. Further decrease of the applied field (to about -325 Oe) pushes both vortices to the right end of the element where the (–, –) state is obtained. Similarly, the reverse branch (from -325 Oe to 254 Oe) of the cycle shown in Figure 4.9, which can be analyzed and described in the same manner, shows that the V2 moves first, and that the (–, +) state is formed at about 83 Oe. The positions of the V1 and V2, as well as the length of W1+W2, were plotted as a function of applied field, as shown in Figure 4.9. The major features of our experimental observations, including details of the interesting domain switching behavior not reported before, were very well reproduced by micromagnetic simulations, as shown in Figure 4.10. Thus, we clearly confirm that the composite Néel wall structures supported in a trilayer element can be controllably switched to arrive at four different states of coupled Néel walls, without affecting the overall flux-closure domain configuration of the element.

4.2.4 Summary

In summary, we studied the detailed field-induced transformation of coupled Néel walls in micron-sized tri-layer elliptical elements for novel domain-wall-based device applications. Using *in-situ* Lorentz transmission electron microscopy and micromagnetic simulation, we demonstrate that the magnetostatically coupled composite wall structure can be switched controllably without affecting the overall flux-closure domain configuration via separate translation of vortex cores in the two magnetic layers. The top and bottom Néel walls either trap or expel each other depending on the relative orientation of their magnetization directions, leading to the interesting domain switching behavior observed during magnetization reversal.

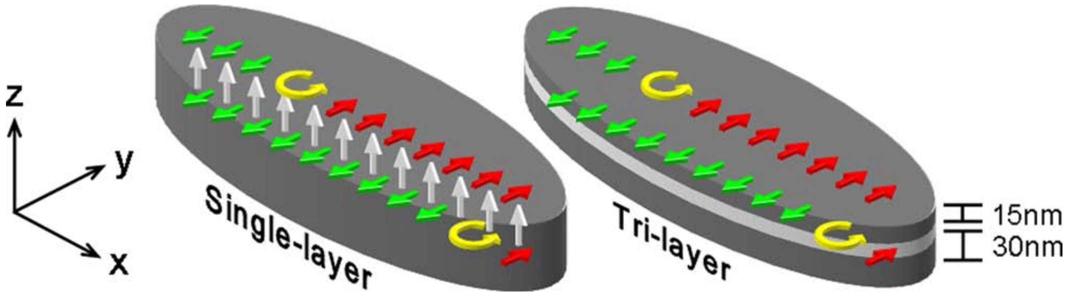

Figure 4.5 Schematic view of the spin configurations of an asymmetric Bloch wall with surface Néel caps within a single-layer elliptical element (Left), and of a composite Néel wall system within a Py/Al/Py tri-layer elliptical element (Right). Magnetization vectors are indicated by arrows with different colors, and vortex structures are indicated by circulating arrows. Only the spin configurations within the wall region are shown for clarity.

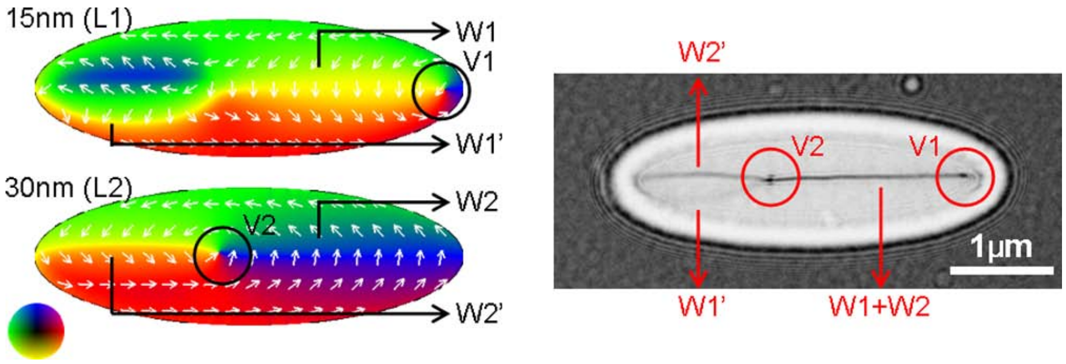

Figure 4.6 Simulated spin configuration of the two Py layers (Left) and experimental Fresnel image (Right) of a Py/Al/Py trilayer element at remanence.

LLG Micromagnetic simulator™ with default material parameters (saturation magnetization Ms=8×10^5 A/m, exchange stiffness constant C=1.3×10^{-11} J/m, magnetocrystalline anisotropy coefficient=0) was employed, and cell size 7.5 nm×7.5 nm×thickness was used for each Py layer. Al spacer was modeled as vacuum. The contrast of the Fresnel micrograph has been digitally inverted to improve visual quality.

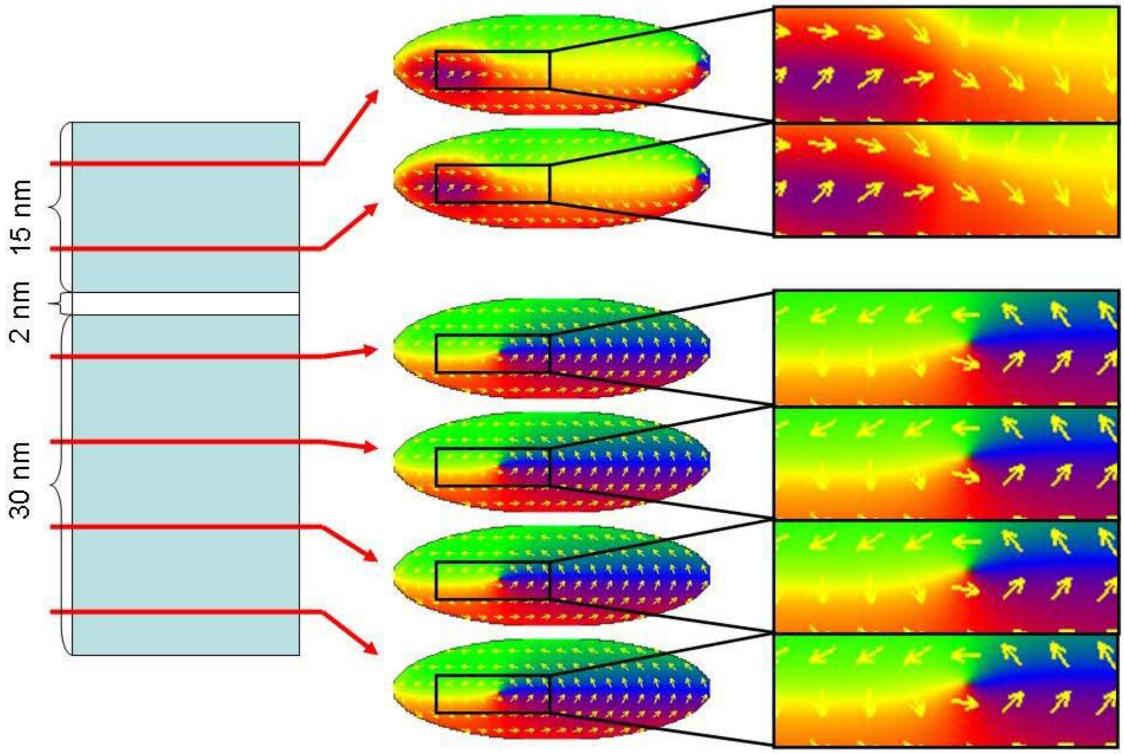

Figure 4.7 Layer-resolved domain configuration of a 1.5 µm × 0.48 µm × 47 nm F/N/F trilayer structure simulated by using 7.5 nm × 7.5 nm × 7.5 nm cell size (or 7.5 nm × 7.5 nm × 2 nm cell size for the spacer).

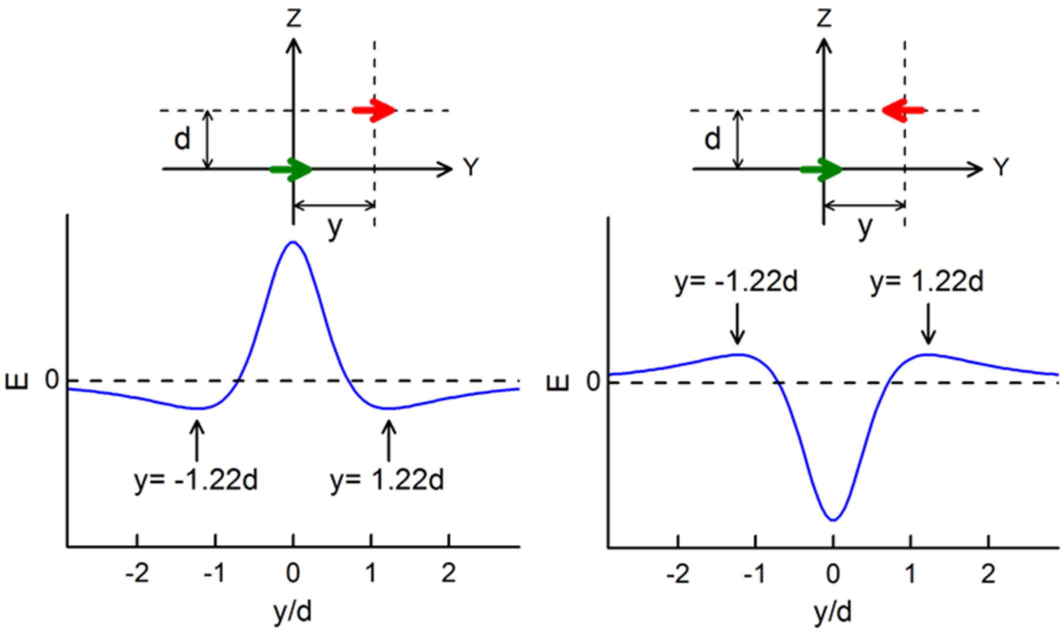

Figure 4.8 Total energy vs. lateral distance curves for two magnetic dipoles separated by a fixed vertical distance of d.

Left panel shows the energy landscape for two dipoles of parallel spin orientation (both in +y direction as defined in Figure 4.5). Right panel shows the energy landscape for two dipoles of anti-parallel spin orientation (one in +y and one in –y direction).

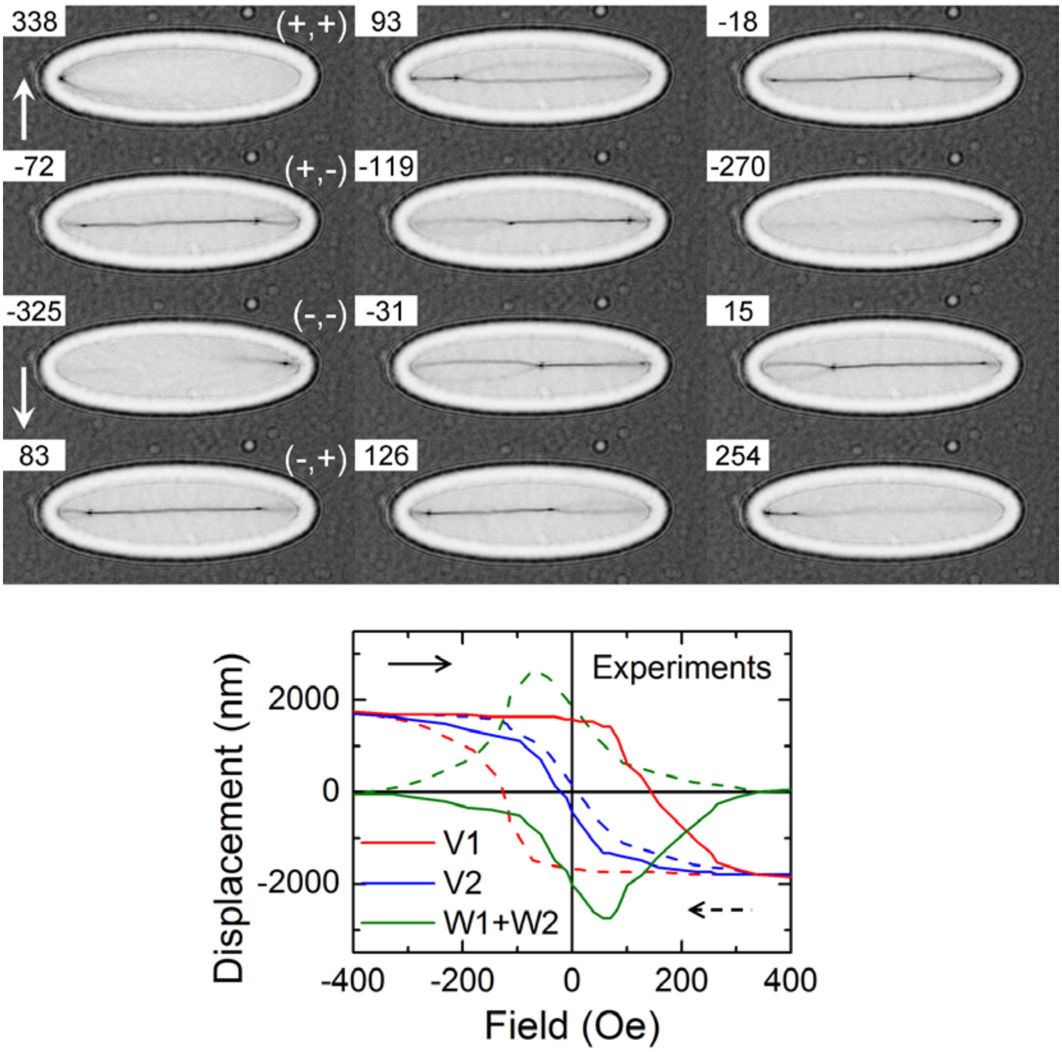

Figure 4.9 Top panel: Experimental Fresnel-mode Lorentz micrographs (contrast inverted) of an individual trilayer element for a complete domain-wall switching cycle. Bottom panel: experimentally measured Displacement vs. Field plots.

In the Lorentz micrographs, the in-plane component of the applied field is applied in the transverse direction to the element, as shown by the white arrows, and field values are indicated in Oersted. The (+, –) sign corresponds to domain wall orientation of L1 and L2, respectively, relative to +y direction defined in Figure 4.5. In the Displacement vs. Field plot, the solid and dashed arrows indicate different field evolution direction. The displacement of each vortex was measured relative to the geometric center of the element. W1+W2 corresponds to the distance between two vortices.

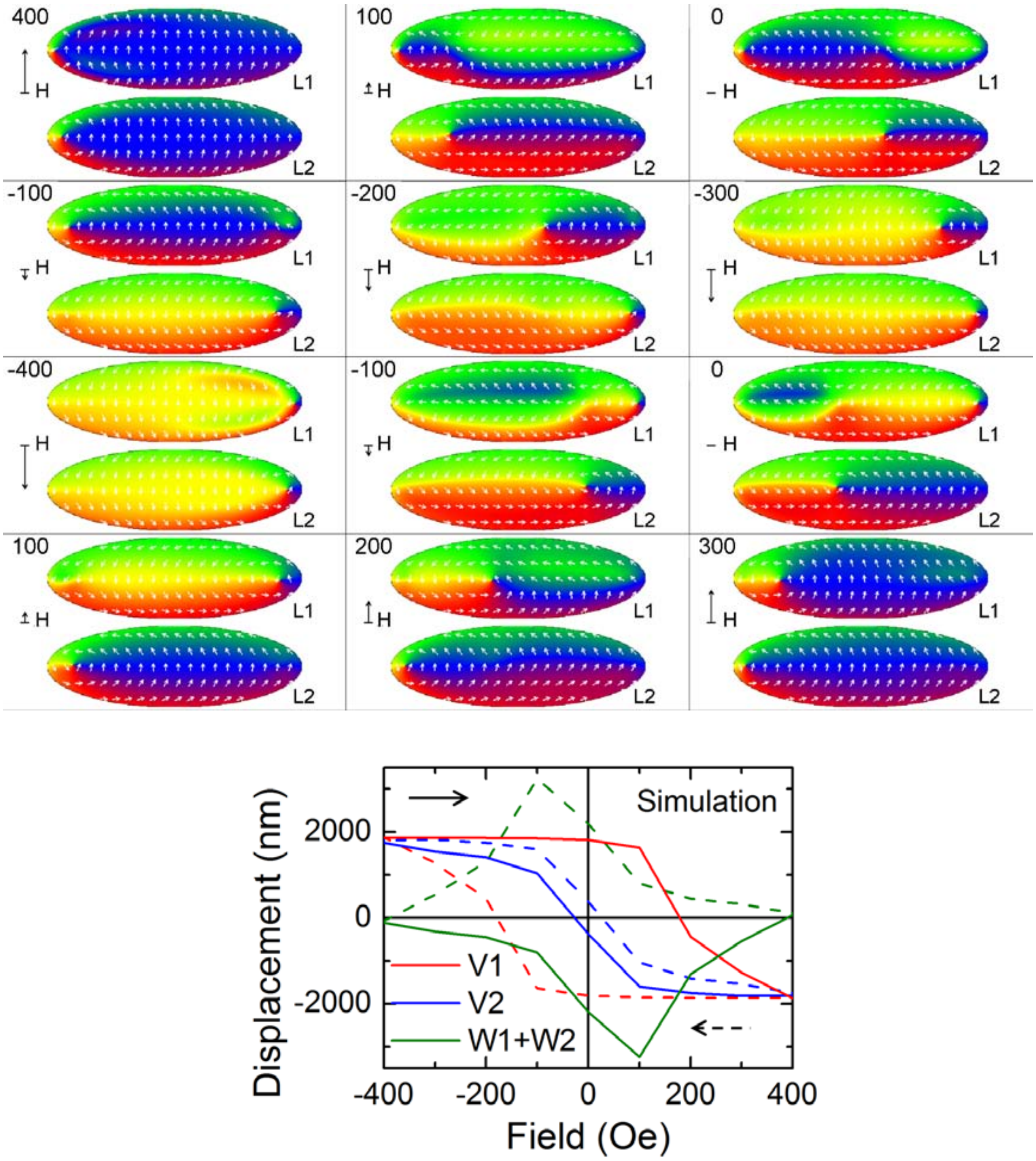

Figure 4.10 Top panel: simulated domain structure for each Py layer for a complete domain-wall switching cycle. Bottom panel: simulated Displacement vs. Field plots.

4.3 Combined Disk-Square Elements

4.3.1 Introduction

The magnetic vortex is one configuration with particular importance for both fundamental research and technological development [53]. This flux-closure structure can be self-stabilized at remanence [25], substantially suppresses stray field generation, and exhibits very well defined responses under various stimulus such as field [20], current [54], pulse [55-56], and high frequency excitations [57]. These properties of the vortex domain state bring together great promise for future non-volatile, high-density, and ultra-efficient spintronic applications [49].

Recently, several groups reported interesting results in patterned trilayer stacks consisting of two ferromagnetic (F) layers separated by a non-magnetic (N) spacer. For example, Buchanan *et. al.* systematically studied how the nonmagnetic spacer layer thickness would affect the coupling strength in patterned Py/Cu/Py cylinders [58]. They reported that cylinders with very thin (1 nm) Cu spacer support oppositely oriented vortices at remanence, while cylinders with thick (20 nm) Cu spacer favor more uniformly structured states such as single domain or off-centered vortices. On the other hand, Yang, et. al. fabricated Co/Cu/Co (10 nm/10 nm/3 nm) ring stacks with sub-micron Planar size, and measured their magneto-resistance in a current-perpendicular-to-plane geometry [59]. They found that such a structure exhibits double-vortex based switching, which could be effectively activated by a current induced annular Oersted field with a spin-torque transfer process. However, despite previous efforts, no direct characterization of the full spin configuration of individual multilayer elements, which is essential for bridging structure-property correlations, has yet been successfully conducted. Conventional magnetic imaging methods either have only surface layer sensitivity (such as Magnetic Force Microscopy and Scanning Electron Microscopy with Polarization Analysis), or lack the quantitative information needed to distinguish individual contributions from each magnetic layer (such as Lorentz Microscopy) [7]. In this section, we present our experimental observation of the switching process of 400 nm patterned F/N/F trilayer stacks using *in-situ* off-axis electron holography. By quantitatively measuring the electron phase shift and comparing it with numerical simulations, the switching behavior of the multi-layer system was unambiguously determined, including identification of the separate switching behavior in each ferromagnetic layer. Separating the contribution of individual magnetic layer is not a trivial matter for any experimental technique due to the stacked nature of the magnetic structure.

For the trilayer stack we studied, a combined square-disk cross section was used to control the vortex chirality upon nucleation. The detailed process was explained in Figure 4.11 (a) by example of a single layer structure. The element was first saturated along the straight edge. When the field was reduced, the spin would curl along the element edge to minimize stray field generation. Due to the asymmetric shape, the overall magnetization was forced to adopt a structure similar to the letter ‘C’, with the strongest curling region located close to the straight edge. This region served as the vortex nucleation site once the field was further reduced, which possessed the chirality directly determined by the C-curling profile, i.e., the initial orientation of the applied field. In the vertical direction of the stack, two magnetic layers of different thickness, separated by a thick non-magnetic spacer, switch at different stages during a hysteresis cycle due to the fact that the critical fields (nucleation and annihilation) for vortex switching are strongly dependent on the geometric aspect ratio (thickness/planar size) of the supporting structure [20]. Along with the chirality-control mechanism mentioned above, these well-separated switching fields enabled proper field recipes to be developed to generate remanent double-vortex states with specific chirality combinations across the whole structure.

4.3.2 Experiments

The trilayer elements consist of 20 nm/20 nm/10 nm thick Py/Al/Py with a planar size of 400 nm. Samples were grown on 50nm thick amorphous Si_3N_4 TEM supporting membrane. A 3nm Ti layer was pre-deposited to enhance surface adhesion to the silicon nitride substrate. Standard electron beam lithography (using PMMA resist), electron beam deposition and lift-off procedures were carried out successively to prepare the patterned elements. During the deposition step, a 3 nm Al capping layer was added to prevent oxidation. After lift-off, the whole specimen surface was coated with 1 nm C to reduce specimen charging during TEM observations. All the materials used were deposited at a base pressure better than 5×10^{-7} Torr and evaporation rates of less than 0.1 nm/s. Off-axis electron holography was performed using our specialized JEOL magnetic imaging microscopes, JEOL 3000F and 2100F-LM. The latter is equipped with a dedicated long-focal-length pole piece [60]. *In-situ* magnetization was carried out via tilting method [61]. The Objective Lens had a fixed excitation of 0.25 V, corresponding to 3528 Oe along the optic axis. Stage tilt was varied between ±25° to change in-plane fields between ±1491 Oe. The systematic error in field calibration is about 15 Oe. Figure 4.11 (b) shows our measurement of the phase shift, which can be converted to the local distribution of induction or magnetization after subtraction of the electrostatic potential, across the vortex core of a Py disk element. With the experimental method and phase reconstruction algorithms developed, we can routinely achieve up to 2.5 μm field of view with a spatial resolution better than 5 nm on the 2100F-LM and 20 nm on 3000 F [Appendix B].

4.3.3 Results and Discussion

While dozens of experiments were conducted, Figure 4.12 shows typical experimental measurements made during one hysteresis cycle with the field applied parallel to the straight edge of the element. Although the measured hysteresis loop appears less than ideal, compared with those derived from volume-averaged measurements such as SQUID (Superconducting Quantum Interference Device), it is in fact extremely useful since a one-to-one correspondence is made between the data points on the loop, and real-space visualization of the magnetic structure present in the element. This is a unique advantage of this technique and is a critical step forward in gaining a comprehensive understanding of magnetic switching processes in general.

Referring to Figure 4.12 and starting from saturation at 1490 Oe, the induction within the sample area was uniform except for slight deviations near the edge of the element due to demagnetization effects. Outside the element, the stray field distribution closely resembled that of a magnetic dipole. As the field was reduced to 430 Oe, both magnetic layers evolved into ‘C’ states. At 240 Oe, a counterclockwise (CCW) vortex (V1) was nucleated in the 10 nm Py layer, while the 20 nm Py layer remained in the ‘C’ state. The nucleation of V1 led to the formation of a closed flux loop within the sample region, which is clearly visible in the 209 Oe contours snapshot of Figure 4.12. This event also triggered a sudden decrease of overall induction, which appeared as a jump in the hysteresis loop. At 123 Oe, a second CCW vortex (V2) was nucleated, this time in the 20 nm Py layer. We attributed the nucleation of V1 to the 10 nm layer and that of V2 to the 20 nm layer by comparing the relative magnitudes of the two associated jumps in the hysteresis loop. Below 123 Oe, after the double-CCW-vortex configuration was obtained, the induction contours outside the sample area were virtually absent, indicating a flux-closure state and strongly suppressed stray field generation. With the field decreased to zero and then increased in the reverse direction, both V1 and V2 propagated toward the curved edge. V1 annihilated at around -215 Oe, followed by V2 at around -400 Oe. These two annihilation events also contributed to two jumps in the hysteresis loop as indicated in Figure 4.12. The sample subsequently adopted the C-state configuration and finally a uniformly aligned saturation state on further increase of the reversed field. The other branch of the hysteresis loop could be similarly analyzed, where a double-CW-vortex configuration is formed at remanence.

In comparison, Figure 4.13 shows the same switching sequence obtained by numerical simulation. Each induction contour was calculated by converting micromagnetically simulated spin configuration into a phase map (as would be obtained from a holography experiment) using the Fourier transform based method developed by Beleggia and Zhu [39]. The simulation suggested the same magnetic evolution process as shown in Figure 4.12, i.e., chirality-controlled nucleation and propagation and annihilation of the double-vortex domain configuration. The values of calculated annihilation fields agree well with experiments, however, values of the nucleation fields differ significantly. Specifically, in contrast to experiments, the simulation showed that the vortex in the 20 nm layer nucleated prior to that of the 10 nm layer, and that both nucleation events happened much later than what was experimentally observed. We believe the reason for the discrepancy is mainly attributed to the fact that vortex nucleation is in reality a very complex process, in contrast to the simplified scenario proposed by the model simulation data. Many factors not properly incorporated into simulation, such as edge roughness [62] or microstructural inhomogeneity [63], could lower the nucleation barrier substantially in certain local regions, and activate a nucleation event long before the global energy minimum was reached. The fact that the 10 nm layer nucleate first, as suggested by experiment, might be due to the reason that thin layer is more sensitive to the defect-activated nucleation process. However, the reconciliation between experiment and calculation requires a more detailed and dedicated structural study, as well as an improved theoretical approach that better models realistic experimental structures. The important implication of this point is that with accurate measurement on individual element, we could be able to quantitatively evaluate any given model simulation or calculation in determining material properties or structural behavior, which is invaluable from a theoretical standpoint.

With knowledge of the detailed switching behavior of our tri-layer stack, we further developed field recipes to prepare remanent double-vortex states with specific chirality combinations. There are in total four types of attainable remanent states, and each of them consists of two centered vortices arranged in the vertical direction, with chirality combination of CW/CW, CW/CCW, CCW/CCW, and CCW/CW for 10nm/20nm Py layers. In Figure 4.12, we already demonstrated the recipes to generate the two remanent states with same vortex chirality (CW/CW and CCW/CCW), i.e., by first saturating the trilayer structure along the straight edge (with correct direction) and then simply relaxing it to remanence. To generate the other two states with opposite chirality combinations, additional steps need to be carried out. Take the CW/CCW state for example as detailed in Figure 4.14 (a). We first generate the CCW/CCW state as described above. Then, we increase the field in the reverse direction, stopping between the two annihilation fields associated with each vortex. At this point, the 10nm layer with annihilated vortex is in the ‘C’ state, while the 20 nm layer still preserves the vortex, albeit with a shifted core position. Compared with the ‘C’ state prior to the nucleation of the CCW/CCW state, the new ‘C’ state in the 10nm layer is now oppositely oriented. Therefore, by relaxing the field back to remanence, a CW vortex is produced in the 10 nm layer. Meanwhile, the 20 nm layer CCW vortex has shifted back to the center of the element, leading to a CW/CCW (10 nm/20 nm) double-vortex remanent configuration. All four field recipes, along with the corresponding remanent states are summarized in Figure 4.14 (b). The figure also includes line-scan comparisons between the measured and calculated phase shift, where the differences among all four remanent states are clearly visible. Relative to the zero phase shift background, the phase shift peaks at 7.5(±0.5) rad, 3(±0.5) rad, -7.5(±0.5) rad, and -3 (±0.5) rad for the CCW/CCW, CW/CCW, CW/CW and CCW/CW (10nm/20nm) states, respectively. Our phase shift measurements agree quantitatively with each respective phase shift calculation, regarding both the distribution profile and signal amplitude. This consistency unambiguously confirmed the feasibility of using defined field sequences to generate specific double-vortex states in a fully controllable manner. The same principle could be potentially useful for the future development of high areal density GMR based magnetic memory devices, with virtually no remanent stray field generated between the closely-packed data bits.

4.3.4 Summary

In summary, we fabricated sub-micron patterned F/N/F trilayer structures as a model system to study double-vortex based switching. With quantitative phase shift measurements of off-axis electron holography, we examined the evolution of local magnetic structures and directly related it to the hysteresis loop of individual trilayer structures. We showed that the switching mechanism involved chirality controlled vortex nucleation, propagation and annihilation with well-separated critical fields for the two magnetic layers. We also demonstrated the feasibility of using controlled field stimulus to arrive at four well-defined remanent states. The ability of using programmed field sequences to uniquely generate various flux-closure remanent-states with different magnetoresistances opens the door to the development of new generation cell architectures by circumventing the cross-talking problem in ultra high density memory devices.

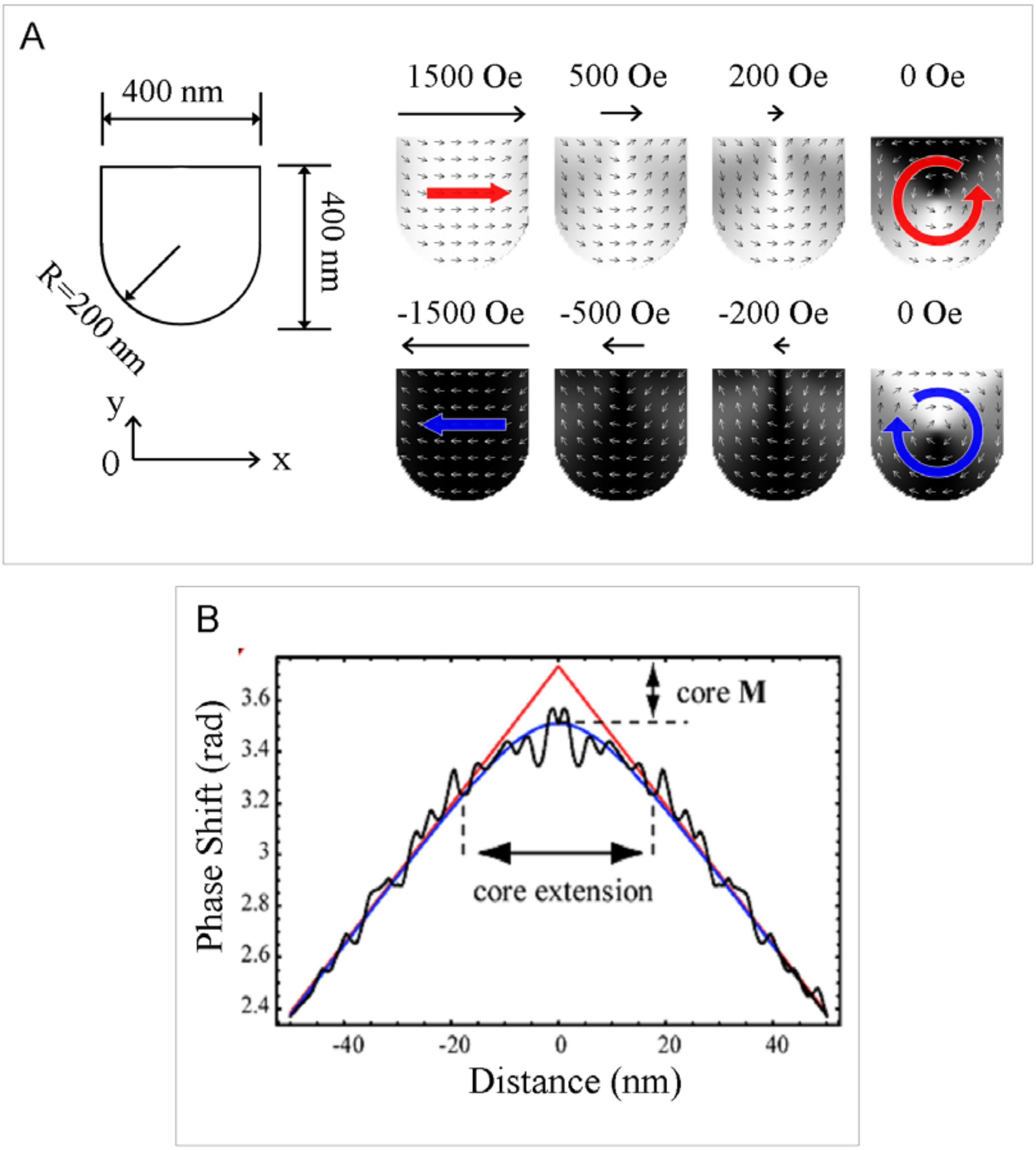

Figure 4.11 (a) Simulated chirality-controlled vortex nucleation process of a single layer element. The sample was a 400 nm wide, 20 nm thick Py element, discretized by 128×128×1 in the LLG micromagnetic simulator. (b) Experimental measured phase shift of a vortex core in a 20nm thick PY element using electron holography, suggesting a core radius of ~40nm.

In (a), a magnetic field was applied along the horizontal direction. Top row: The element was initially saturated (1500 Oe) in +x direction. After relaxation, a counterclockwise (CCW) vortex was nucleated. Bottom row: The element was initially saturated in the -x direction. After relaxation, a clockwise (CW) vortex was nucleated. In (b), opposite slopes at the two sides of the curve implicate reversed magnetization across the core center. The black line is the measurement, the blue line is the phase shift calculated by M. Beleggia, and the red line is the phase shift for a core of zero extension.

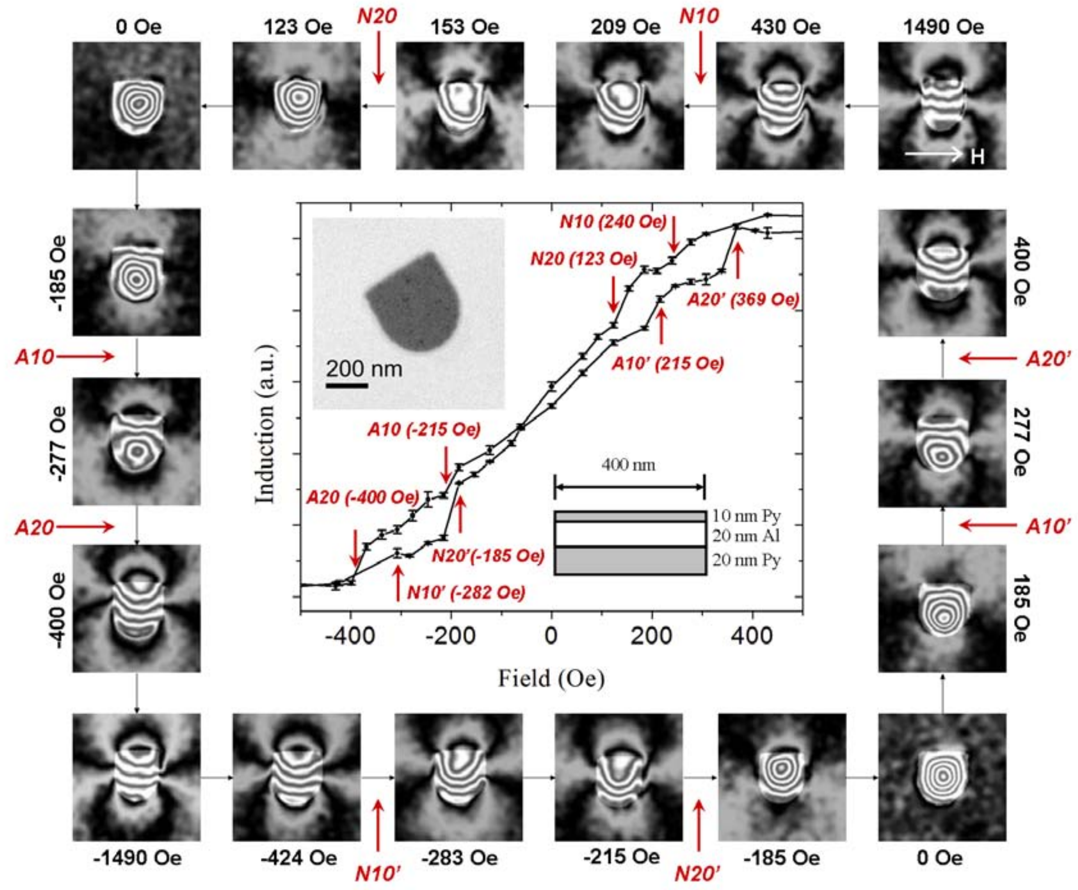

Figure 4.12 Experimentally measured hysteresis loop with corresponding induction contours snapshots at representative field stages.

Each point at the hysteresis loop was averaged from three trials, with the error bar showing standard deviation. Red arrows marked out nucleation fields (N) and annihilation fields (A), with layer thickness (20 or 10) and measured field values specified. Top-left inset was the bright field TEM image of the sample. Bottom-right inset showed the sample geometry. Each contour image was generated by performing cosine operation on 4 times amplified magnetic phase shift, and the contour lines correspond to projected magnetic induction distribution. Element region was slightly highlighted for visual guidance. Electrostatic inner potential induced phase shift, obtained by taking average of the saturation states at two opposite tilting angles, was always subtracted in this paper.

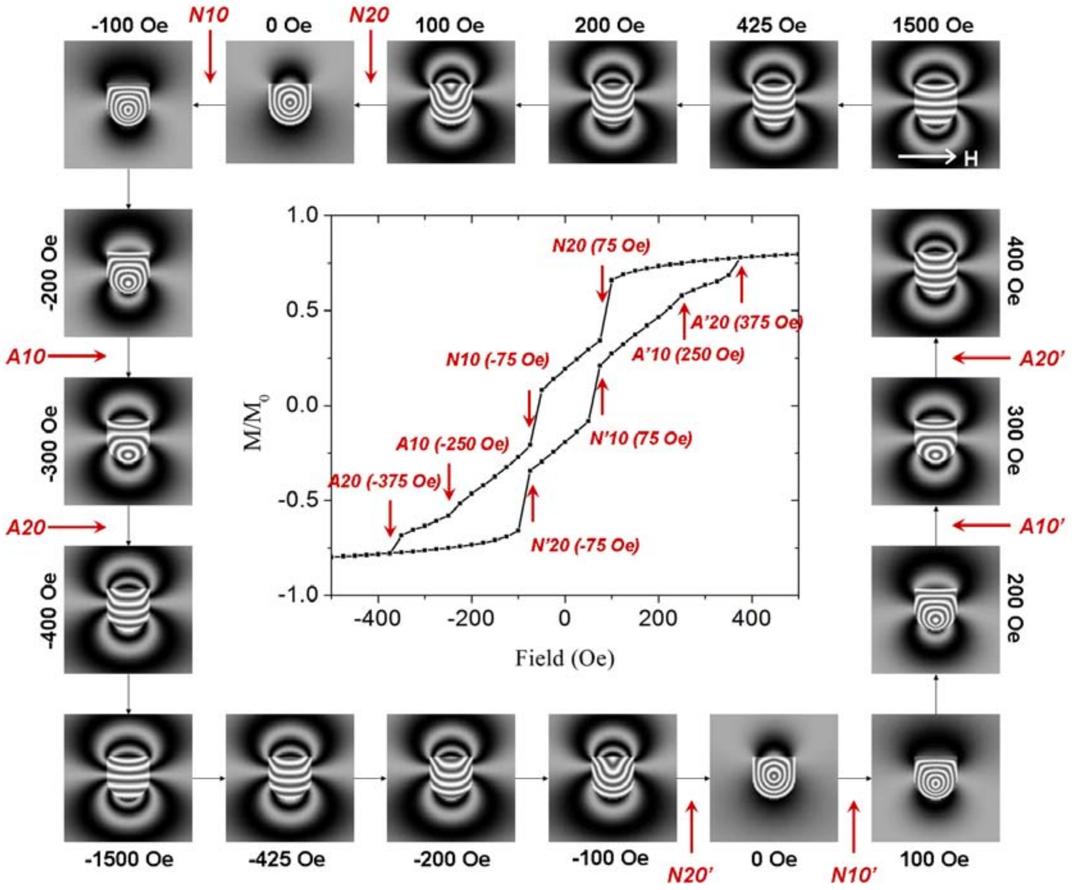

Figure 4.13 Simulated hysteresis loop with corresponding induction contours at representative field stages.

Micromagnetically simulated spin configurations were first converted to magnetic phase maps, and then induction contours were generated by performing cosine operation on 4 times amplified phase. A constant field (3000Oe) perpendicular to the plane was added to model realistic experimental setup. Note that a B-H loop was used in Figure 4.12, while a M-H loop was used here.

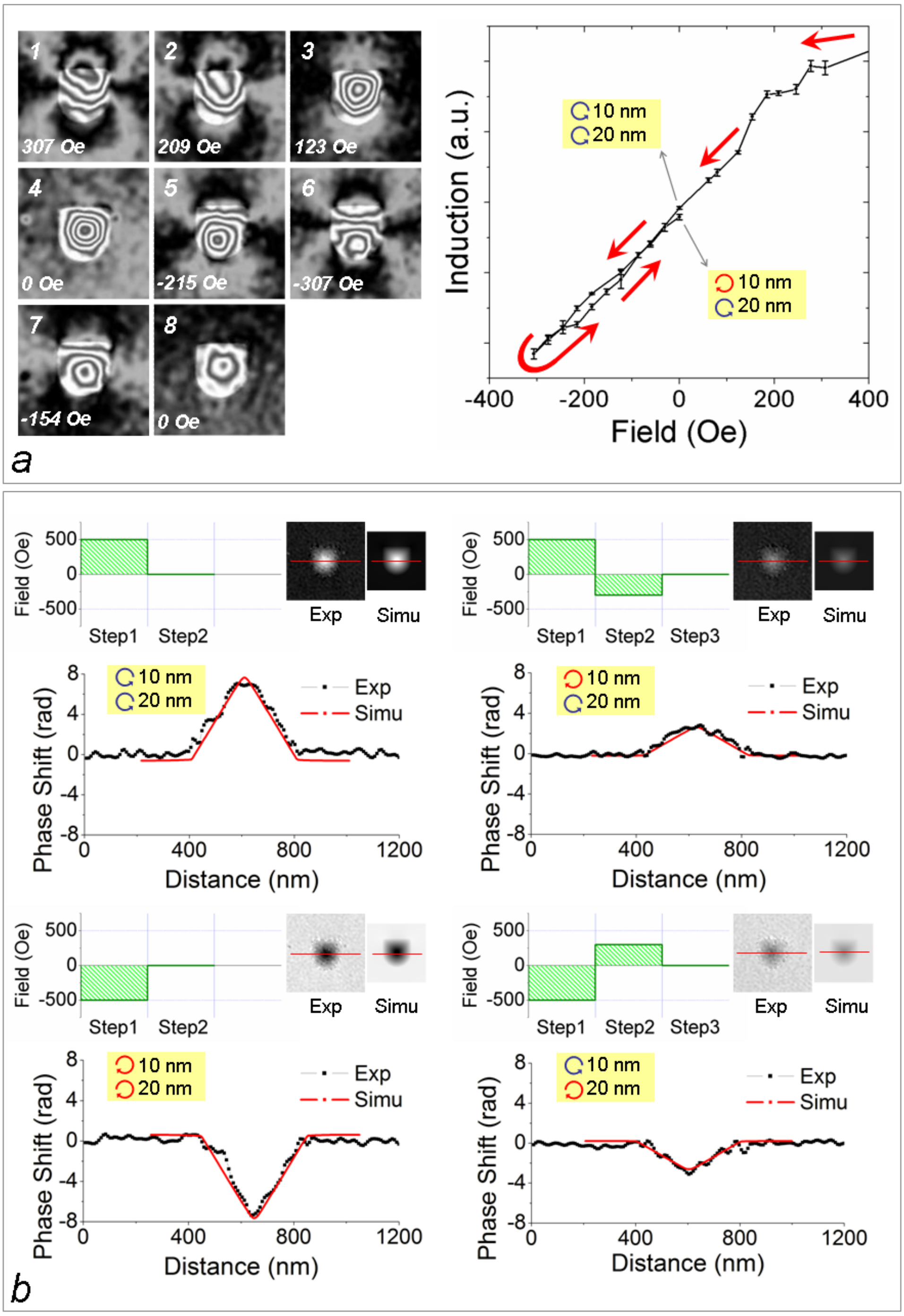

Figure 4.14 (a). Detail process of generating double-vortex remanent states with chirality combinations of CCW/CCW (inset a-4) and CW/CCW (inset a-8) in 10nm/20nm Py layers. (b). Summary of all four field recipes, along with the vortex chirality arrangement (for each Py layer), measured/simulated phase shift maps and corresponding line-scan comparison of the destination states.

For each line scan plot, the black dotted line indicates experimental data, while red line corresponds to simulated data.

Chapter 5. Current-induced Resonant Precession of Magnetic Vortex

5.1 Introduction

5.1.1 Motivation

Data writing will be severely problematic if the physical dimension of elementary magnetic storage unit continuous to shrink into nanometer regime. Conventionally, stray field generated by writing head has been employed as the primary means to control and toggle the magnetization orientation. However, as pointed out by Claude Chappert in a recent review article [49], the downscaling in magnetic storage unit will lead to increased coercivity, which requires corresponding increase in the writing field in order for the magnetic moment to switch. But this requirement can not be easily fulfilled, because attainable writing field actually decreases due to reduced sizes of conducting wires. As a result of this dilemma, random thermal excitation will eventually make the storage device no longer stable for any practical applications.

The discovery that spin-polarized electrons traveling through ferromagnets apply a torque on the local magnetization opened up a new field of research in solid state physics that could potentially address the aforementioned challenge [64]. Compared with field-driven reversal, current-driven reversal is fundamentally more advantageous due to the fact that the strength of the spin-transfer-torque depends only on current density. Therefore, the conducting wires can scale down together with the elementary data storage unit as long as the current density keeps unchanged.

A major problem associated to this current-based technology, however, is its low efficiency: an unusually high current density is required to induce significant change of local magnetization. The high current density may generate excessive heat and even induce electro-migration effect, which will adversely affect device durability.

One possible way to address this challenge is that instead of using direct current, we can use alternating current (AC) to activate a collective resonance to amplify the spin transfer effect. Previous studies have shown that the spin-torque switching proceeds via a process of magnetic precession with increasing precession amplitude [65-66]. The precession frequency depends on material properties and specific spin configurations, and remains almost constant during the switching process. Therefore, if the frequency of external AC driving stimuli is tuned to match precisely the natural precession frequency of the nanomagnet system, spin transfer efficiency can be significantly improved. This resonant switching concept has been successfully demonstrated for several model systems, such as depinning domain wall from a pinning notch of magnetic wire [67], and switching the multilayered nanopillar at low temperature [68].

A more elegant system to quantitatively investigate the resonant effect is the magnetic vortex confined in a patterned nanomagnet. For example, in micron-sized soft magnetic squares, due to negligible crystalline anisotropy, a Landau structure is formed with four quadratic domains circulating around the center. In the center region known as vortex core, spins are progressively tilted out of plane to avoid singularity. Similar to the intrinsic precession of a classic magnetic spin, the Landau structure is able to gyrate coherently. Previously, excitation of vortex domain by magnetic field has been extensively studied, both theoretically [69-73] and experimentally [74-76], and people found that the resonant frequency depend strongly on the thickness/width ratio of the square element. More recently, research interests have shifted towards directly exciting vortices by spin-polarized current [77-79]. X-ray based imaging techniques has been proved particularly useful in visualizing the vortex dynamics with nanosecond time resolution.

In this chapter, we show by *in-situ* Lorenz microscopy that the vortex core precession orbit of a Landau structure can be directly visualized and quantified with very high spatial resolution compared with X-ray based techniques.

5.1.2 Theory

Here, we consider both the current- and field- driven gyroscopic motion of magnetic vortices in square thin film elements of size l and thickness t [80]. In the presence of a spin-polarized current, the time evolution of the magnetization is given by the extended LLG equation:

$$\begin{aligned}\frac{d\vec{M}}{dt} &= -\gamma[\vec{M}\times\vec{H}_{eff}] + \frac{\alpha}{M_S}\vec{M}\times\frac{d\vec{M}}{dt} - \frac{b_j}{M_S^2}\vec{M}\times[\vec{M}\times(\vec{j}\cdot\nabla)\vec{M}] \\ &-\xi\frac{b_j}{M_S}\vec{M}\times(\vec{j}\cdot\nabla)\vec{M}\end{aligned} \tag{5-1}$$

with the coupling constant:

$$b_j = \frac{P\mu_B}{eM_S(1+\xi^2)} \tag{5-2}$$

between the current and the magnetization, where P is the spin polarization, M_S the saturation magnetization, and ξ the degree of nonadiabaticity. If the vortex keeps its static structure, its motion with the velocity $\vec{v}$ can be described using the Thiele equation. This equation was expanded by Thiaville *et.al.* [81] to include the action of a spin-polarized current:

$$\vec{F} - \vec{G}\times(\vec{v} + b_j\vec{j}) - D(\alpha\vec{v} + \xi b_j\vec{j}) = 0 \tag{5-3}$$

The Gyrovector

$$\vec{G} = \frac{2\pi M_S\mu_0 t}{\gamma}\vec{e}_z = G_0\vec{e}_z \tag{5-4}$$

indicates the axis of precession and points out of plane. The dissipation tensor is diagonal:

$$\begin{aligned}D_{xx} &= D_{yy} = D_0 \approx \frac{\pi M_S\mu_0 t\ln(l/a)}{\gamma} \\ D_{zz} &= 0\end{aligned} \tag{5-5}$$

The constant a is the lower bound of the integration, and can be approximated by the radius of the vortex core. As for any square-symmetric confining potential, the stray-field energy for small deflections can be modeled by a parabolic potential,

$$E_S = \frac{1}{2} m\omega_r^2 (X^2 + Y^2) \tag{5-6}$$

with the coordinates X and Y being the position of the vortex core.

In real samples, due to possible inhomogeneities, the current flow may vary in the out-of-plane direction. This results in an in-plane Oersted field, which is perpendicular to the direction of the current flow, but of the same frequency. In the following, this Oersted field is accounted for by a homogeneous magnetic field in the y direction. To estimate the Zeeman energy due to the Oersted field H, the magnetization pattern is divided into four triangles. Assuming that the magnetization is uniform in each of these triangles, the total Zeeman energy is given by:

$$E_z = \frac{\mu_0 M_S H l t}{2}[(\frac{l}{2} + X) - (\frac{l}{2} - X)] \tag{5-7}$$

This simple approximation describes the field-induced vortex motion sufficiently well. In this case, the force is given by:

$$F = -\nabla(E_S + E_Z) = -\mu_0 M_S H l t \vec{e}_x - m\omega_r^2 X \vec{e}_x - m\omega_r^2 Y \vec{e}_y \tag{5-8}$$

The equation of motion of the vortex can be written as:

$$\begin{pmatrix} \dot{X} \\ \dot{Y} \end{pmatrix} = \begin{pmatrix} -\Gamma & -\omega \\ \omega & -\Gamma \end{pmatrix} \begin{pmatrix} X \\ Y \end{pmatrix} + \begin{pmatrix} \frac{\omega\Gamma}{\omega^2 + \Gamma^2} \frac{\mu_0 M_S H l t}{G_0} - b_j j - \frac{\Gamma^2}{\omega^2 + \Gamma^2} \frac{\xi - \alpha}{\alpha} b_j j \\ \frac{-\omega^2}{\omega^2 + \Gamma^2} \frac{\mu_0 M_S H l t}{G_0} + \frac{\omega\Gamma}{\omega^2 + \Gamma^2} \frac{\xi - \alpha}{\alpha} b_j j \end{pmatrix} \tag{5-9}$$

In the following, we assume harmonic excitation; i.e., the magnetic field and the electrical current are of the form:

$$\begin{aligned} H(t) &= H_0 e^{i\Omega t} \\ j(t) &= j_0 e^{i\Omega t} \end{aligned} \tag{5-10}$$

where t is the time and Ω is the driving frequency. The magnetic field and the electrical current are in phase. Assuming that the squared Gilbert damping is small ($\alpha^2 << 1$), the damping constant of the vortex is small compared to its frequency ($\Gamma^2 << \omega^2$). Then, the solution is:

$$\begin{pmatrix} X \\ Y \end{pmatrix} = A\begin{pmatrix} i \\ 1 \end{pmatrix} e^{-\Gamma t + i\omega t} + B\begin{pmatrix} -i \\ 1 \end{pmatrix} e^{-\Gamma t - i\omega t}$$
$$- \frac{e^{i\Omega t}}{\omega^2 + (i\Omega + \Gamma)^2} \begin{pmatrix} \left(\widetilde{H} + \frac{\Gamma}{\omega}\frac{\xi}{\alpha}\widetilde{j} \right)\omega + \left(\frac{\Gamma}{\omega}\widetilde{H} + \widetilde{j} \right) i\Omega \\ \widetilde{j}\,\omega - \left(\widetilde{H} + \frac{\Gamma}{\omega}\frac{\xi - \alpha}{\alpha}\widetilde{j} \right) i\Omega \end{pmatrix} \tag{5-11}$$

with $\widetilde{H} = \frac{\gamma H_0 l}{2\pi}$, $\widetilde{j} = b_j j_0$, free frequency $\omega = -\frac{G_0 m \omega_r^2}{G_0^2 + D_0^2 \alpha^2}$, and damping constant $\Gamma = -\frac{D_0 \alpha m \omega_r^2}{G_0^2 + D_0^2 \alpha^2}$. The first two terms with prefactors A and B are exponentially damped and depend on the starting configuration. Considering $\frac{\Gamma}{\omega} << 1$, steady state solution is simplified as:

$$\begin{pmatrix} X \\ Y \end{pmatrix} = -\frac{e^{i\Omega t}\omega}{\omega^2 + (i\Omega + \Gamma)^2} \begin{pmatrix} \widetilde{H} \\ \widetilde{j} \end{pmatrix} - \frac{e^{i\Omega t} i\Omega}{\omega^2 + (i\Omega + \Gamma)^2} \begin{pmatrix} \widetilde{j} \\ -\widetilde{H} \end{pmatrix}$$
$$= -\frac{e^{i\Omega t}}{\omega^2 + (i\Omega + \Gamma)^2} \left(\frac{\gamma l}{2\pi} cH \begin{pmatrix} -\omega \\ i\Omega \end{pmatrix} - b_j j \begin{pmatrix} i\Omega \\ \omega \end{pmatrix} \right) \tag{5-12}$$

Based on equation (5.12), at resonance (when $\Omega = \omega$), the amplitude of the vortex core displacement in x and y directions is the same, and the vortex performs a circular rotation. A vortex that is excited with a nonresonant frequency has an elliptic trajectory. The ratio between the semi-axes is given by the ratio between the frequency of the excitation and the resonance frequency.

5.2 Experiments

5.2.1 *In-Situ* TEM Holder for Microwave Excitation

Although a rich variety of TEM holders have been developed to perform different *in-situ* experiments, to our best knowledge, none of these holders is suitable for delivering very high frequency signals in 100MHz to GHz range. We therefore designed and constructed a home-made holder using the machine shop facilities at the Brookhaven laboratory. The main function of our TEM specimen holder is to deliver a high frequency electrical signal (generated by a commercial signal source) into the sample region, with minimal power loss and waveform distortion.

There are three basic requirements that need to be considered for our holder design: holder geometry, vacuum seal, and electrical path.

First, the holder geometry must accommodate the existing column design of JEOL TEM. During operation, the tip of the specimen holder sits between the objective lens pole pieces, which usually has very narrow gap (about 3 mm for JEOL 3000F and 8 mm for JEOL 2100F-LM) in order to achieve high focusing strength. The vertical dimension of the tip must therefore be smaller than the pole piece gap to avoid mechanical contact. On the other hand, the geometry of the holder body, including the location of the pin and o-rings, must match exactly the corresponding parts of the goniometer, in order for the vacuum locking system to function properly. Since it’s very difficult for us to measure the critical dimension inside the goniometer, the aforementioned problem has been primarily addressed by reverse engineering: we measured instead the outer geometries of a handful of commercial JEOL TEM specimen holders, and use these data as reference for our instrumental design. The detailed design charts have been attached as Appendix C at the end of this dissertation.

Second, the holder has to be vacuum sealed. This is typically not a problem for conventional holders, which is nothing more than a metallic sample transfer rod and the vacuum sealing can be achieved simply by the double o-ring system. For our *in-situ* holder, however, the holder body is a hollow tube with a coax cable built in. When fully loaded into operational position, the holder is equivalent to an extended part of the TEM column chamber. In this case, the vacuum seal is achieved by the 2.75” Conflat flange located at the end of the holder assembly [Figure 5.1].

Third, we developed a three-stage electrical system for our holder. In the first stage, the external signal was transmitted from the outside signal generator to the tip part, by a UHV-compatible coax cable (50 Ohm impedance). A standard SubMiniature version A (SMA) vacuum feedthrough (Accuglass) is installed at the end of the holder, to provide both a connection port and vacuum sealing. In the second stage, signal is transmitted via the Cu coplanar waveguide on a printed circuit board (PCB). We used Rogers RO4000 series (Rogers) polymer as substrate of the PCB, due to its UHV and high frequency compatibility. The connection between PCB and coax cable was done by direct welding. In the third stage, a microscopic circuit is prepared on top of a Silicon Nitride Membrane, by e-beam lithography and lift-off technique. This is Cr/Au microstrip-type circuit, part of which is located on top of the electron-transparent Silicon Nitride window for TEM imaging. The micro-strip circuit is designed together with the specimen, and is reconfigurable depending on specific experiment requirements. The connection between Silicon Nitride membrane and PCB was done by wire bonding. The completed holder assembly, as well as location of each individual parts described above, is shown in Figure 5.2.

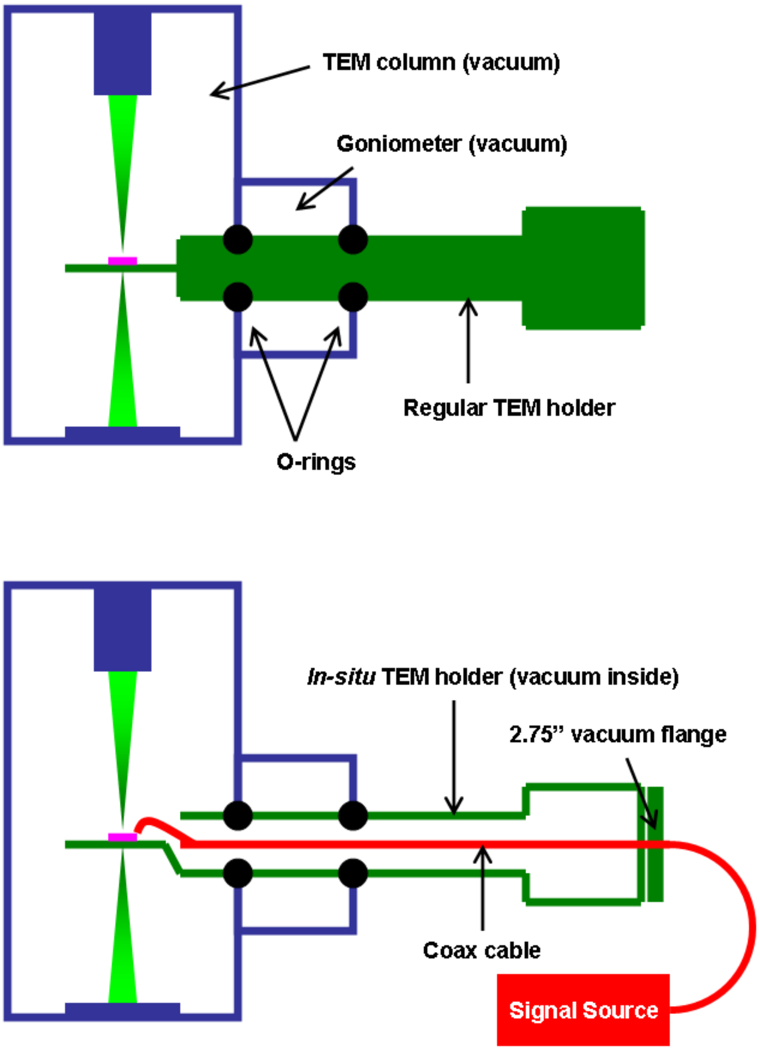

Figure 5.1 Comparison of the vacuum logic between a regular TEM holder (top panel) and our *in-situ* holder (bottom panel).

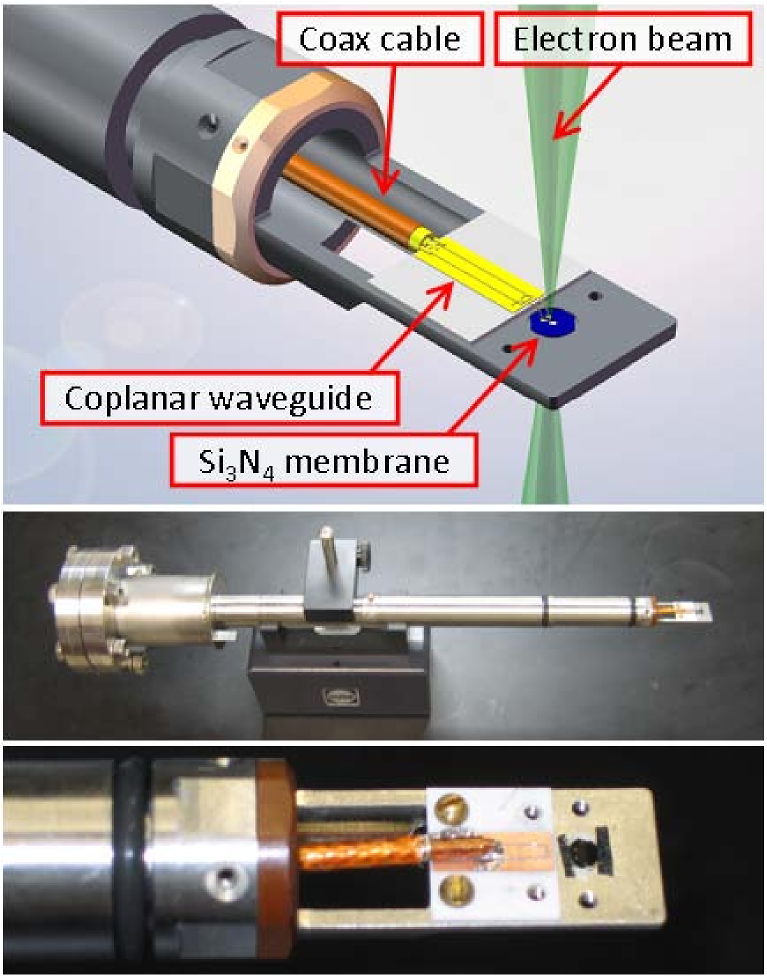

Figure 5.2 Computer graphics and photos of the *in-situ* TEM holder assembly

5.2.2 Device Fabrication

Microstructured Py squares were fabricated using two-step electron beam lithography and lift-off methods. We used a commercial silicon nitride membrane (200 nm) back deposited with Cr (3 nm) as substrate to ensure electron transparency. Each square was made with 2 micron planar size and 50 nm thickness. To excite the structures with alternating currents, they were contacted by Cr/Au (5 nm/ 100 nm) strip lines, and the contact resistance was measured using probe station. SEM images of our fabricated device were shown in Figure 5.3.

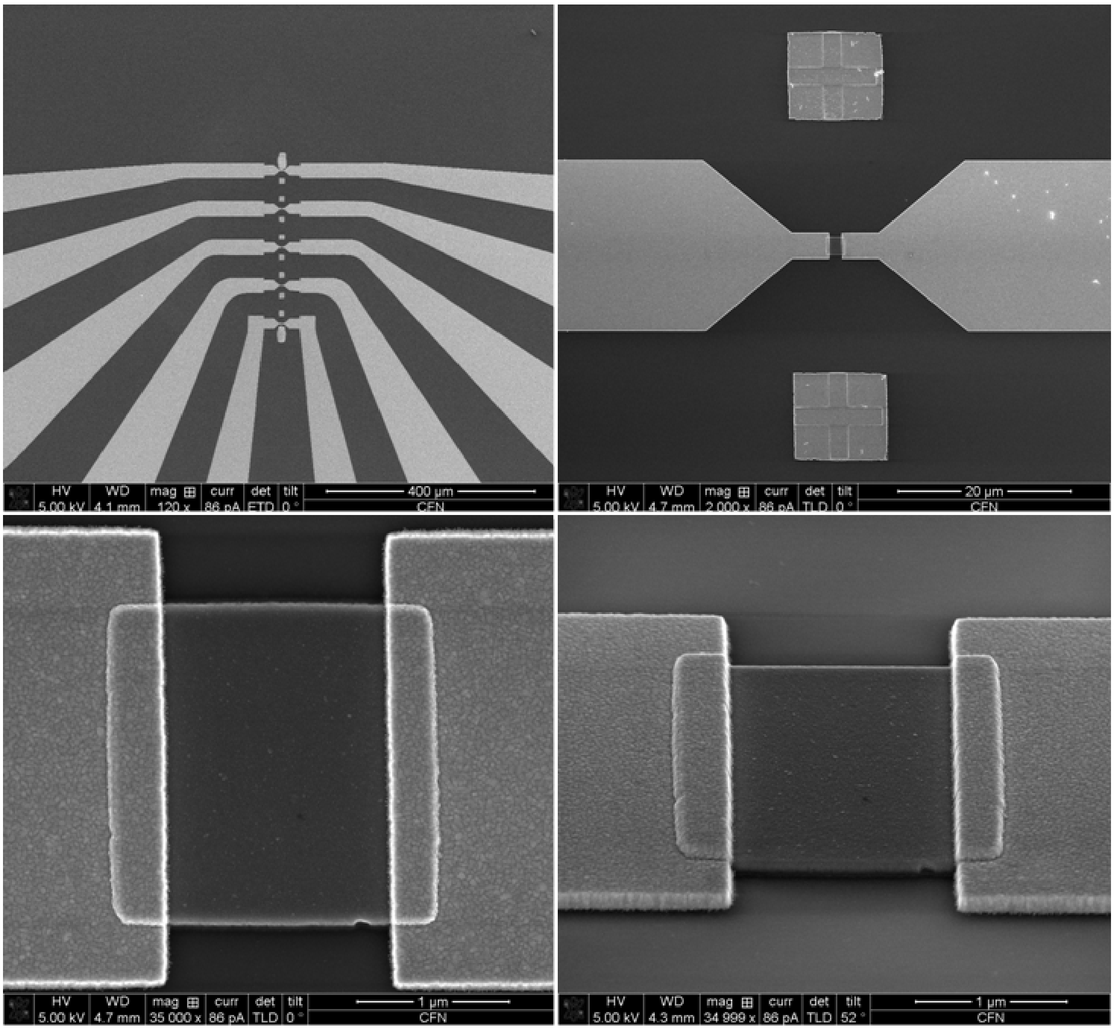

Figure 5.3 SEM images of the Py square and Cr/Au contacting pads fabricated on top of silicon nitride membranes.

5.2.3 Supporting Instruments

Due to the limited working space inside the narrow gap of objective lens pole pieces, all the supporting instruments were located outside the TEM column, and were connected as shown in Figure 5.4.

The high frequency continuous wave (CW) signal is provided by an Agilent N5181A MXG analog signal generator (100 to 1000 MHz, -110 dBm to 13 dBm). The signal is sampled by a Coaxial Directional Coupler (Mini-circuits ZFDC-20-4L, 50 Ohm, 10 to 1000 MHz), and the waveform is monitored by a Tektronics TDS 3052C Digital Phosphor Oscilloscope. For instrumental connections, we used flexible, triple-shield test cables with SMA connectors (Mini-circuits) to ensure high frequency compatibility.

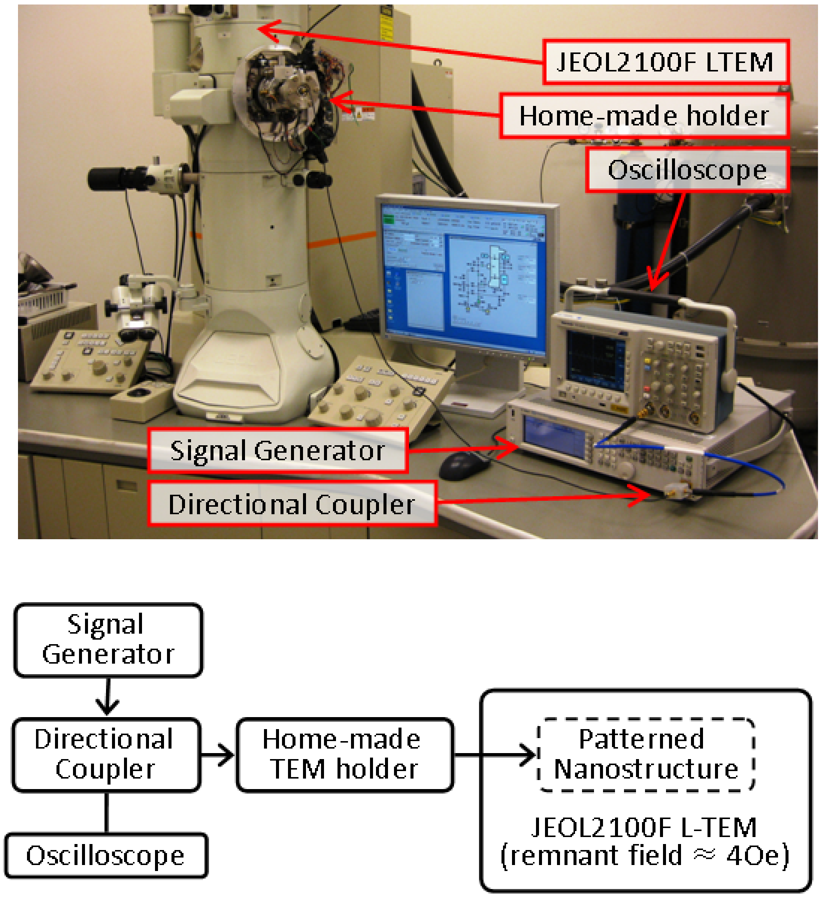

Figure 5.4 Supporting instruments and their connection diagram for *in-situ* high frequency TEM experiments.

5.3 Results and Discussion

Figure 5.5 shows a Lorentz micrograph of the remanent state domain configuration. A Landau structure, which features a bright vortex core and four well-defined domain walls, was clearly visible. The Py square was divided into four quadratic magnetic domains that form an overall flux-closure configuration.

Figure 5.6 shows a sequence of Lorentz images when the same element was excited by an alternating current with 180 MHz fixed frequency and increasing current density. The 180 MHz frequency was chosen because it is very close to the theoretically calculated resonant frequency, so that largest precession orbit can be expected with each current density. As an external AC current was applied, the image showed several notable changes. For example, the single bright spot at the center of remanent state image has transformed into a ring-shaped contrasts. Meanwhile, the four domain walls also changed into four triangle-shaped regions, with one end of the wall pinned to the corner of the square and the other end spread with the center ring.

These observations confirm the steady-state precession motion of vortex core, as illustrated by Figure 5.7. During each precession period, the vortex core travels along a well-defined orbit, which is given by equation 5.12. Each of the TEM micrograph was recorded with 4 seconds exposure time, compared with the precession period of about 5.5×10^{-9} seconds. Therefore, the ring contrast revealed in our observations corresponds to the overlapped trace of about 7.2×10^{8} precession periods.

We measured the size of the precession orbit as a function of current density, repeated with five different frequencies, as shown in Figure 5.8. According to Equation 5.12, the precession amplitude should be a linear function of current density. However, from our experimental data, we found that the actual relationship is non-linear and shows discontinuous steps. Take 180 MHz curve for example. At low current density (less than 6.1×10^{10} A/m^2), the amplitude remains small (about 50 nm). At 6.3×10^{10} A/m^2, the amplitude suddenly jumped, with an increase of about 50%. After that, the amplitude increase linearly with current density, until at 8.1×10^{10} A/m^2, the ring contrast becomes obscured. These observations strongly suggest that defect pinning played an important role in our experiments [82]. At low current densities, the vortex core gyrates about its equilibrium position, and the precession amplitude is suppressed by the defect pinning. At high current densities, the vortex core is energetic enough to overcome the local pinning potential, and the precession amplitude is determined by Equation 5.12. The sharp transition between these two regimes is due to the depinning of the vortex core from a local defect. Above certain critical current densities [83-84], the precession orbit becomes so large that the vortex core undergoes severe distortion, and the precession orbit was constantly destabilized by strong dynamical effects (such as polarity reversal and spin wave generation). At this point and beyond, ring contrast becomes obscured, as shown in the last image of Figure 5.6.

We also performed frequency sweeps to study the resonance behavior, as shown in Figure 5.9. The current density was fixed at 7.7×10^{10} A/m^2: strong enough to overcome the pinning potential but weak enough to remain a stable orbit. Figure 5.10 summarizes the measurement of precession orbit estimated from the Lorentz observations.

From Equation 5.12, we can calculate the precession amplitude as

$$A=\sqrt{\frac{(\tilde{j}\,\omega+\tilde{H}\Omega)(\tilde{H}\omega+\tilde{j}\,\Omega)}{\Gamma^4+(\omega^2-\Omega^2)^2+2\Gamma^2(\omega^2+\Omega^2)}} \tag{5-13}$$

With known current density, his equation can be used to fit experimental data. The parameters obtained by the fitting are:

$$\begin{aligned}&\frac{\omega}{2\pi}=181.26\,MHz,\\&\alpha=\frac{\Gamma}{\omega}\cdot\frac{G_0}{D}=0.016,\\&H=132\,A/m=1.7\,Oe\end{aligned} \tag{5-14}$$

According to the theory, as driving frequency is varied, the precession orbit not only changes its size, but also its shape. The precession orbit is only strictly circular at resonant frequency, while at other frequencies, the orbit is distorted to an elliptical shape. This is however not very prominent from our experimental observations: from Figure 5.9, we can see slight elongation of precession along vertical axis at frequencies lower than resonance, and elongation along horizontal axis at frequencies higher than resonance. Although this trend is indeed confirmed by the steady-state orbit [Figure 5.11] calculated using Equation 5.12 and the parameters estimated by above fitting results, further improvement in spatial resolution is needed before this small but important effect can be experimentally studied and quantitatively analyzed.

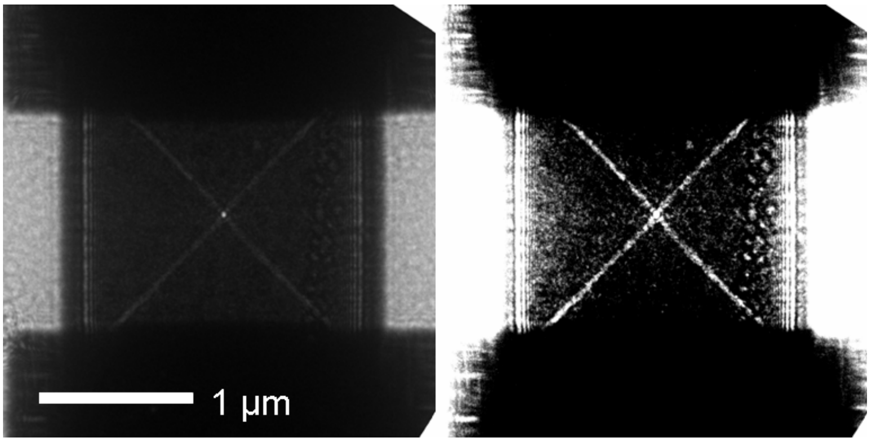

Figure 5.5 Lorentz micrograph of the Py square showing remanent state Landau domain structure.
Left: raw image. Right: image contrast has been enhanced to accentuate the location of domain wall and vortex core.

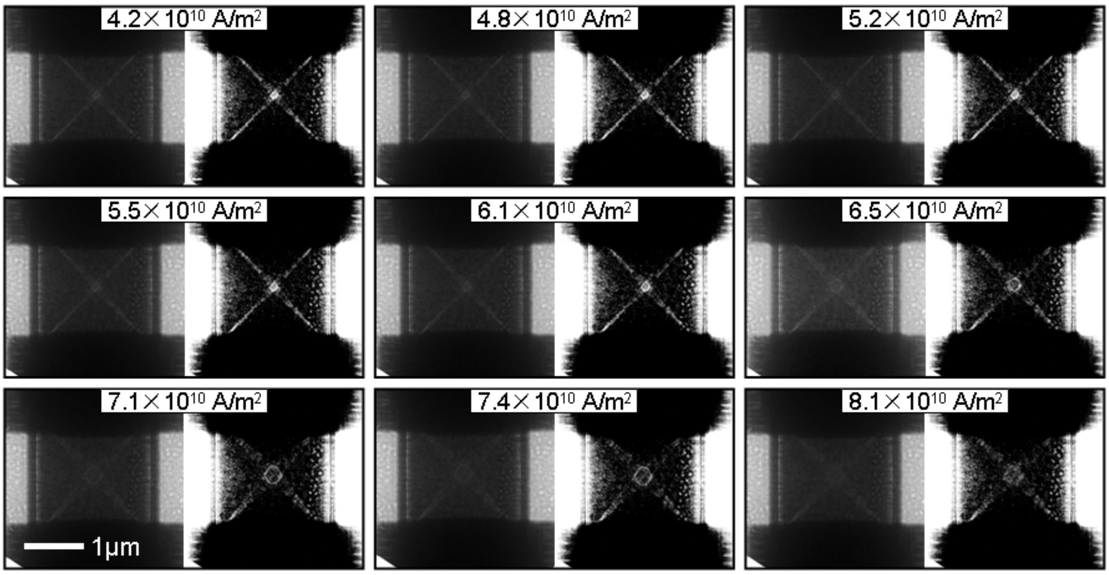

Figure 5.6 Lorentz micrographs of vortex core precession orbit vs. driving current density.
The AC current was applied along vertical direction, with frequency maintained at 180 MHz and current density varied as indicated. Each figure was recorded with about 5 micron defocus and 4 seconds exposure time. For each current density, left side corresponds to raw image, and right side corresponds to contrast-enhanced image.

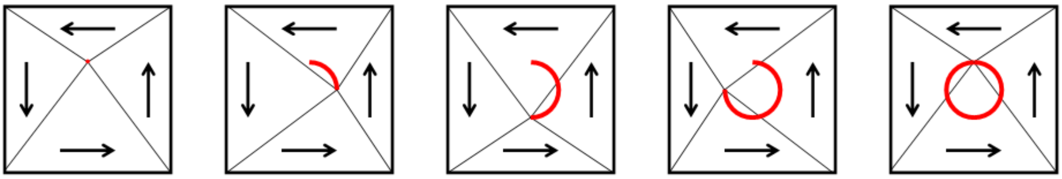

Figure 5.7 Explanation of the formation of ring-shaped contrast in Lorentz microscopy.

The black lines correspond to domain walls of Landau structure. The red solid line corresponds to the precession trace of vortex core.

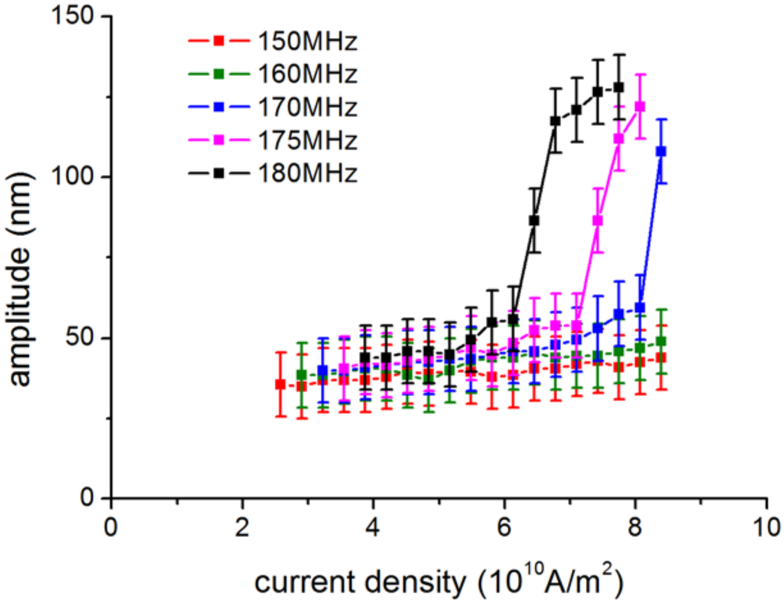

Figure 5.8 Precession amplitude vs. current density plots, with measurement repeated for five different frequencies.

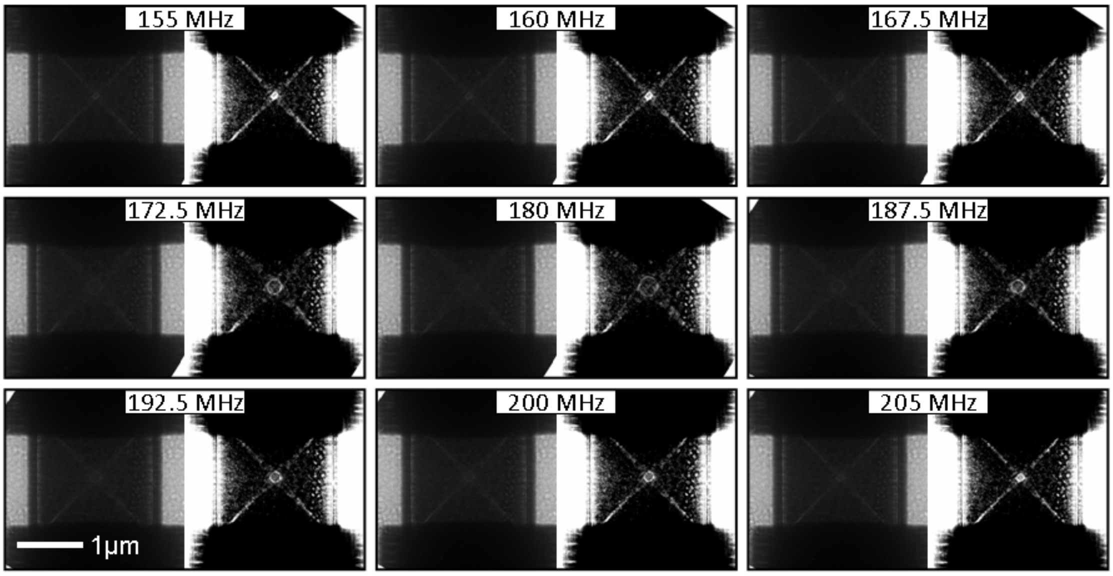

Figure 5.9 Lorentz micrographs of vortex core precession orbit vs. driving frequency. The AC current was applied along vertical direction, with current density maintained at 7.7×10^{10} A/m^2 and frequency varied as indicated. Each figure was recorded with about 5 micron defocus and 4 seconds exposure time.

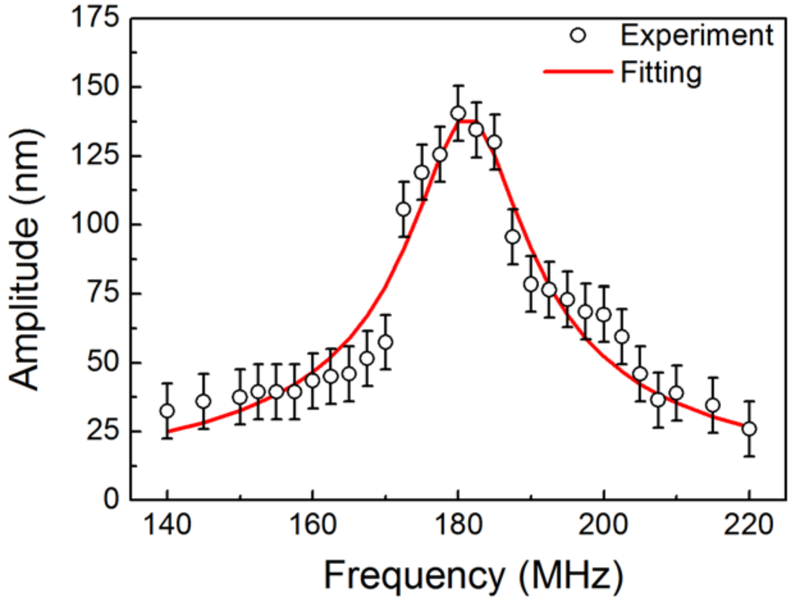

Figure 5.10 Precession amplitude vs. Frequency curve

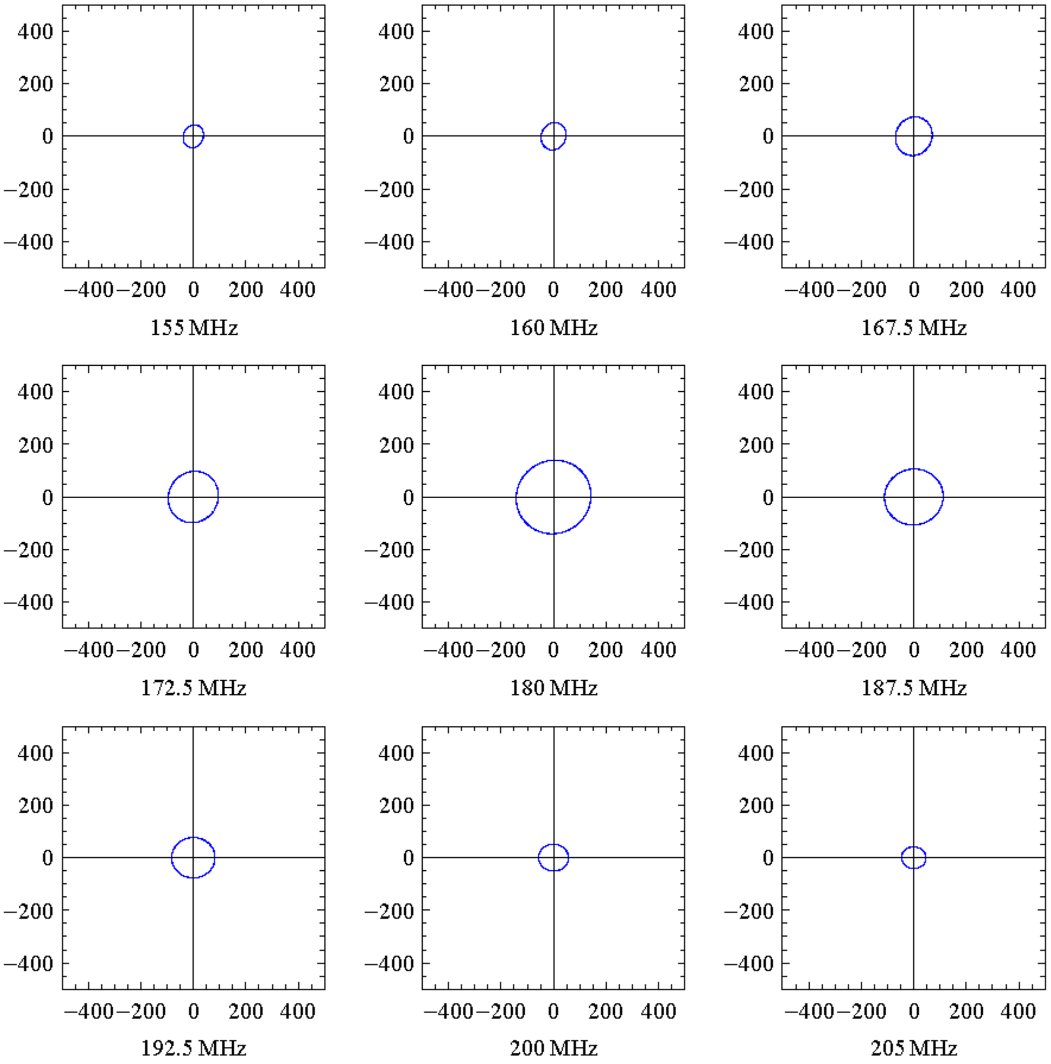

Figure 5.11 Numerically calculated vortex core precession orbit vs. driving frequency

5.4 Summary

In summary, we developed a novel sample stage to perform *in-situ* high frequency excitation experiment inside TEM. We observed for the first time the current-induced resonant precession of magnetic vortex core using Lorentz microscopy. We found very sharp ring-shaped contrast that directly corresponds to the precession orbit of vortex core. At very low current densities, precession movements were strongly suppressed by defect pinning; while at very high current densities, the precession orbit become unstable because of strong dynamical distortion of vortex core. At intermediate current densities, the resonance peaks at about 181 MHz. From the data fitting, the Gilbert damping coefficient was determined to be 0.016, and a 1.7 Oe alternating Oersted field was found coexist with (and perpendicular to) the alternating current. In addition, we also obtained first evidence of possible shape dependence of sweeping frequency, which is consistent with the overall trend suggested by numerical calculation.

Chapter 6. Outlook

In this dissertation, we have demonstrated that TEM can be very effectively used to reveal the inner spin microstructure of tiny magnetic objects, and explore various fundamental physics phenomena *in-situ* and in real time. Although having unarguably the highest spatial resolution attainable for all the imaging tools, further development of TEM-based magnetic imaging technique will largely depend on how successful we can overcome its fundamental limits. Two of the most important limitations are the projection problem and time resolution.

The projection problem comes naturally from the transmission geometry, and is a universal challenge that is not only restricted to magnetic imaging. TEM micrographs are recorded in two-dimensional fashion, but what really fascinates us is the overall structural information in all three dimensions. To include the missing dimension, tremendous efforts have been devoted to the development of tomography technique, in which the samples are progressively tilted at different angles, and the resulting image stacks are aligned and digitally processed to reconstruct three-dimensional information [85]. So far, regular TEM tomography has evolved into a fairly mature stage, where the whole image acquisition and processing operations can be fully automated by modern instrumentation and commercial software packages. Such technique has been adopted rapidly by materials scientists as an important microscopy tool for the three-dimensional study of morphologies and chemical compositions of nanostructures. For magnetic studies, however, the so-called vector-field tomography, which is able to reconstruct the three dimensional magnetic vector fields inside and around magnetic specimens of specific shapes, was only conceptually proposed. The basic idea of this method is the combination of electron holography with electron tomography to characterize electrostatic and magnetic fields inside nanostructured materials with nanometer spatial resolution in three dimensions. Although the theory underlying such measurements is well established, their experimental implantation is complicated by the fact that contribution of the mean inner potential to the measured total phase shift must be removed at each sample tilt angle. This requires additional tilting sequence to be performed. Whether or not this technique is in reality feasible, and to what level of precision one can achieve, needs more dedicated efforts and in-depth studies. But with the availability of better and faster program code as well as faster computers this seems to be a feasible task.

Another fundamental limitation of TEM technique is the time resolution. This is because the basic working principle of CCD involves charge accumulation, amplification and voltage-readouts, which are much slower processes compared with the operations of photodiode that is widely used in x-ray based ultrafast imaging techniques. Several different solutions have been proposed to circumvent this challenge. First approach is based on stroboscopic pump-probe principle, in which the pulsed electron source is activated by laser-driven photoemission, and a single region of the sample is excited and sampled periodically at a given instant of time after a defined delay [86]. This method allows temporal and spatial resolutions to be maintained at the optimal levels, but the fact that the specimen must be laser pumped millions of times means that the process being studied must be highly repeatable or that the sample must completely recover between shots. In this regard, a more promising approach is the single-shot method. In particular, encouraging progress has been achieved on the “Dynamic-TEM (DTEM)” instrument located at Lawrence Livermore National Laboratory (LLNL). Using this machine, dynamic experiments are performed by using a laser to “pump” a transient state in the specimen and another laser to produce a “packet” of electrons at the source that then travels down the column to “probe” the sample response. By varying the delay between pump and probe, ultrafast non-reversible processes created by the pump laser can be studied. Currently, the DTEM based on the JEOL 2000FX at LLNL can produce images with less than 20 nm spatial resolution and about 15 nanosecond temporal resolution [87]. Although still under intensive development, these first achievements already demonstrate the great applicability of this technique to the many non-equilibrium and transient magnetic phenomena.

Opportunities also reside in other fields. In recent publications, it was shown that it is possible to detect a dichroic behavior of magnetic materials with electrons which can be considered to be the electron analog for X-ray magnetic circular dichroism (XMCD) [88]. This effect is presently investigated and may in the future lead to new, element specific technique to image the magnetic moment distribution within a specimen. In analogy to XMCD, even a separation of orbital and spin magnetic moments seems possible, in principle.

In all, the electron beam has been, and will continue to be one of the most important experimental probes that can help scientists understand the magnetic structure, properties and manipulation on nanoscales, which are the first steps to develop future spintronics devices and bring the blueprint of nanotechnology to reality.

References

[1]. D. D. Awschalom and M. E. Flatte, Nat. Phys. **3** (3), 153-159 (2007).

[2]. S. A. Wolf, D. D. Awschalom, R. A. Buhrman, J. M. Daughton, S. von Molnar, M. L. Roukes, A. Y. Chtchelkanova and D. M. Treger, Science **294** (5546), 1488-1495 (2001).

[3]. I. Zutic, J. Fabian and S. Das Sarma, Rev. Mod. Phys. **76** (2), 323-410 (2004).

[4]. H. J. Richter, A. Y. Dobin, R. T. Lynch, D. Weller, R. M. Brockie, O. Heinonen, K. Z. Gao, J. Xue, R. J. M. van der Veerdonk, P. Asselin and M. F. Erden, Appl. Phys. Lett. **88** (22), 3 (2006).

[5]. R. P. Cowburn, J. Phys. D: Appl. Phys **33** (1), R1-R16 (2000).

[6]. C. L. Chien, F. Q. Zhu and J. G. Zhu, Phys. Today **60** (6), 40-45 (2007).

[7]. Y. Zhu, *Modern Techniques for Characterizing Magnetic Materials*. (Springer, New York, 2005).

[8]. J. Zweck, S. Braundl, S. Henzelmann, M. Schneider, S. Otto, M. Heumann and T. Uhlig, Scr. Mater. **48** (7), 967-973 (2003).

[9]. J. N. Chapman and M. R. Scheinfein, J. Magn. Magn. Mater. **200** (1-3), 729-740 (1999).

[10]. J. Cumings, E. Olsson, A. K. Petford-Long and Y. Zhu, MRS Bull. **33** (Feburary), 101-106 (2008).

[11]. Y. Aharonov and D. Bohm, Phys. Rev. **115** (3), 485-491 (1959).

[12]. A. Hubert and R. Schafer, *Magnetic Domains: the analysis of magnetic microstructures*. (Springer, 1998).

[13]. M. De Graef and Y. M. Zhu, J. Appl. Phys. **89** (11), 7177-7179 (2001).

[14]. M. R. McCartney and D. J. Smith, Ann. Rev. Mater. Res. **37**, 729-767 (2007).

[15]. R. E. Dunin-Borkowski, M. R. McCartney, D. J. Smith and S. S. P. Parkin, Ultramicroscopy **74** (1-2), 61-73 (1998).

[16]. J. W. Lau, M. A. Schofield and Y. Zhu, Ultramicroscopy **107** (4-5), 396-400 (2007).

[17]. P. Rai-Choudhury, in *SPIE Press Monograph* (SPIE publications, 1997), Vol. 1.

[18]. M. R. Scheinfein, pp. LLG Micromagnetics Simulator Ver. 2.61.

[19]. K. Y. Guslienko, V. Novosad, Y. Otani, H. Shima and K. Fukamichi, Appl. Phys. Lett. **78** (24), 3848-3850 (2001).

[20]. K. Y. Guslienko, V. Novosad, Y. Otani, H. Shima and K. Fukamichi, Phys. Rev. B **65** (2), 024411 (2002).

[21]. P. J. Grundy and R. S. Tebble, Adv. in Phys. **17**, 153-242 (1968).

[22]. H. Horst, J. Appl. Phys. **35**, 1790-1798 (1964).

[23]. H. W. Fuller and M. E. Hale, J. Appl. Phys. **31** (2), 238 (1960).

[24]. K. J. Harte, J. Appl. Phys. **39** (3), 1503 (1968).

[25]. T. Shinjo, T. Okuno, R. Hassdorf, K. Shigeto and T. Ono, Science **289** (5481), 930-932 (2000).

[26]. M. Schneider, H. Hoffmann and J. Zweck, Appl. Phys. Lett. **77** (18), 2909-2911 (2000).

[27]. M. R. McCartney, R. E. Dunin-Borkowski, M. R. Scheinfein, D. J. Smith, S. Gider and S. S. P. Parkin, Science **286** (5443), 1337-1340 (1999).

[28]. M. Mansuripur, J. Appl. Phys. **69** (4), 2455-2464 (1991).

[29]. T. Haug, S. Otto, M. Schneider and J. Zweck, Ultramicroscopy **96** (2), 201-206 (2003).

[30]. S. McVitie and G. S. White, J. Phys. D-Appl. Phys. **37** (2), 280-288 (2004).

[31]. C. A. Ross, F. J. Castano, W. Jung, B. G. Ng, I. A. Colin and D. Morecroft, J. Phys. D: Appl. Phys. **41** (11), 113002 (2008).

[32]. J. G. Zhu, Y. F. Zheng and G. A. Prinz, J. Appl. Phys. **87**, 6668-6673 (2000).

[33]. M. Beleggia, J. W. Lau, M. A. Schofield, Y. Zhu, S. Tandon and M. De Graef, J. Magn. Magn. Mater. **301** (1), 131-146 (2006).

[34]. F. Q. Zhu, G. W. Chern, O. Tchernyshyov, X. C. Zhu, J. G. Zhu and C. L. Chien, Phy. Rev. Lett. **96** (2), 027205 (2006).

[35]. K. He, D. J. Smith and M. R. McCartney, Appl. Phys. Lett., 172503 (172503 pp.) (2009).

[36]. T. J. Hayward, J. Llandro, R. B. Balsod, J. A. C. Bland, D. Morecroft, F. J. Castano and C. A. Ross, Phys. Rev. B **74**, 134405 (2006).

[37]. K. S. Buchanan, K. Y. Guslienko, S. B. Choe, A. Doran, A. Scholl, S. D. Bader and V. Novosad, J. Appl. Phys. **97** (10), 10H503 (2005).

[38]. X. B. Zhu, P. Grutter, V. Metlushko, Y. Hao, F. J. Castano, C. A. Ross, B. Ilic and H. I. Smith, J. Appl. Phys. **93** (10), 8540-8542 (2003).

[39]. M. Beleggia, M. A. Schofield, Y. Zhu, M. Malac, Z. Liu and M. Freeman, Appl. Phys. Lett. **83** (7), 1435-1437 (2003).

[40]. L. Heyderman, M. Klaui, R. Schaublin, U. Rudiger, C. A. F. Vaz, J. A. C. Bland and C. David, J. Magn. Magn. Mater. **290**, 86-89 (2005).

[41]. T. Kasama, P. Barpanda, R. E. Dunin-Borkowski, S. B. Newcomb, M. R.

McCartney, F. J. Castano and C. A. Ross, J. Appl. Phys. **98** (1), 013903 (2005).

[42]. T. Uhlig and J. Zweck, Phys. Rev. Lett. **93** (4), 047203 (2004).

[43]. R. E. Dunin-Borkowski, M. R. McCartney, B. Kardynal, S. S. P. Parkin, M. R. Scheinfein and D. J. Smith, J. Microsc.-Oxford **200**, 187-205 (2000).

[44]. R. D. McMichael and M. J. Donahue, IEEE. Trans. Magn. **33**, 4167-4169 (1997).

[45]. F. Cheynis, A. Masseboeuf, O. Fruchart, N. Rougemaille, J. C. Toussaint, R. Belkhou, P. Bayle-Guillemaud and A. Marty, Phys. Rev. Lett. **102** (10), 107201 (2009).

[46]. F. Cheynis, N. Rougemaille, R. Belkhou, J. C. Toussaint and O. Fruchart, J. Appl. Phys. **103** (7), 07D915 (2008).

[47]. R. Hertel, O. Fruchart, S. Cherifi, P. O. Jubert, S. Heun, A. Locatelli and J. Kirschner, Phys. Rev. B **72** (21), 214409 (2005).

[48]. A. S. Arrott and R. Hertel, J. Appl. Phys. **103** (7), 07E739 (2008).

[49]. C. Chappert, A. Fert and F. N. Van Dau, Nat. Mater. **6** (11), 813-823 (2007).

[50]. P. Vavassori, N. Zaluzec, V. Metlushko, V. Novosad, B. Ilic and M. Grimsditch, Phys. Rev. B **69** (21), 214404 (2004).

[51]. J. W. Lau, M. Beleggia and Y. Zhu, J. Appl. Phys. **102** (4), 043906 (2007).

[52]. J. D. Jackson, *Classic Electrodynamics*, 3rd Edition ed. (John Wiley & Sons, Inc., New York, 1999).

[53]. R. Antos, Y. Otani and J. Shibata, J. Phys. Soc. Jpn. **77** (3), 8 (2008).

[54]. J. Shibata, Y. Nakatani, G. Tatara, H. Kohno and Y. Otani, Phys. Rev. B **73** (2), 020403 (2006).

[55]. B. Van Waeyenberge, A. Puzic, H. Stoll, K. W. Chou, T. Tyliszczak, R. Hertel, M. Fahnle, H. Bruckl, K. Rott, G. Reiss, I. Neudecker, D. Weiss, C. H. Back and G. Schutz, Nature **444** (7118), 461-464 (2006).

[56]. T. Kasama, R. E. Dunin-Borkowski, M. R. Scheinfein, S. L. Tripp, J. Liu and A. Wei, Adv. Mater. **20** (22), 4248-4252 (2008).

[57]. S. Kasai, Y. Nakatani, K. Kobayashi, H. Kohno and T. Ono, Phys. Rev. Lett. **97** (10), 107204 (2006).

[58]. K. S. Buchanan, K. Y. Guslienko, A. Doran, A. Scholl, S. D. Bader and V. Novosad, Phys. Rev. B **72** (13), 134415 (2005).

[59]. T. Yang, A. Hirohata, L. Vila, T. Kimura and Y. Otani, Phys. Rev. B **76** (17), 172401 (2007).

[60]. M. A. Schofield, M. Beleggia, Y. Zhu and G. Pozzi, Ultramicroscopy **108** (7), 625-634 (2008).

[61]. M. Heumann, T. Uhlig and J. Zweck, Phys. Rev. Lett. **94** (7), 077202 (2005).

[62]. J. W. Lau, R. D. McMichael, M. A. Schofield and Y. Zhu, J. Appl. Phys. **102** (2), 023916 (2007).

[63]. J. W. Lau, R. D. McMichael, S. H. Chung, J. O. Rantschler, V. Parekh and D. Litvinov, Appl. Phys. Lett. **92** (1), 012506 (2008).

[64]. J. C. Slonczewski, J. Magn. Magn. Mater. **159** (1-2), L1-L7 (1996).

[65]. I. N. Krivorotov, N. C. Emley, R. A. Buhrman and D. C. Ralph, Phys. Rev. B **77** (5), 054440 (2008).

[66]. T. Devolder, C. Chappert, J. A. Katine, M. J. Carey and K. Ito, Phy. Rev. B **75** (6), 064402 (2007).

[67]. L. Thomas, M. Hayashi, X. Jiang, R. Moriya, C. Rettner and S. Parkin, Science **315** (5818), 1553-1556 (2007).

[68]. Y. T. Cui, J. C. Sankey, C. Wang, K. V. Thadani, Z. P. Li, R. A. Buhrman and D. C. Ralph, Phys. Rev. B **77** (21), 214440 (2008).

[69]. K. Y. Guslienko, B. A. Ivanov, V. Novosad, Y. Otani, H. Shima and K. Fukamichi, J. Appl. Phys. **91** (10), 8037-8039 (2002).

[70]. B. A. Ivanov and C. E. Zaspel, Phys. Rev. Lett. **94** (2) (2005).

[71]. C. E. Zaspel, B. A. Ivanov, J. P. Park and P. A. Crowell, Phys. Rev. B **72** (2) (2005).

[72]. L. Ki-Suk and K. Sang-Koog, Appl. Phys. Lett. **91** (13), 132511 (2007).

[73]. B. Kruger, A. Drews, M. Bolte, U. Merkt, D. Pfannkuche and G. Meier, J. Appl. Phys. **103** (7) (2008).

[74]. V. Novosad, F. Y. Fradin, P. E. Roy, K. S. Buchanan, K. Y. Guslienko and S. D. Bader, Phys. Rev. B **72** (2) (2005).

[75]. K. Y. Guslienko, X. F. Han, D. J. Keavney, R. Divan and S. D. Bader, Phys. Rev. Lett. **96** (6) (2006).

[76]. K. W. Chou, A. Puzic, H. Stoll, D. Dolgos, G. Schutz, B. Van Waeyenberge, A. Vansteenkiste, T. Tyliszczak, G. Woltersdorf and C. H. Back, Appl. Phys. Lett. **90** (20) (2007).

[77]. M. Bolte, G. Meier, B. Kruger, A. Drews, R. Eiselt, L. Bocklage, S. Bohlens, T. Tyliszczak, A. Vansteenkiste, B. Van Waeyenberge, K. W. Chou, A. Puzic and H. Stoll, Phy. Rev. Lett. **100** (17) (2008).

[78]. S. Kasai, P. Fischer, M. Y. Im, K. Yamada, Y. Nakatani, K. Kobayashi, H. Kohno and T. Ono, Phys. Rev. Lett. **101** (23) (2008).

[79]. R. Moriya, L. Thomas, M. Hayashi, Y. B. Bazaliy, C. Rettner and S. S. P. Parkin, Nat. Phys. **4** (5), 368-372 (2008).

[80]. B. Kruger, A. Drews, M. Bolte, U. Merkt, D. Pfannkuche and G. Meier, Phys. Rev. B **76** (22) (2007).

[81]. A. Thiaville, Y. Nakatani, J. Miltat and Y. Suzuki, Europhys. Lett. **69** (6), 990-996 (2005).

[82]. R. L. Compton and P. A. Crowell, Phys. Rev. Lett. **97** (13), 137202 (2006).

[83]. K. S. Lee, S. K. Kim, Y. S. Yu, Y. S. Choi, K. Y. Guslienko, H. Jung and P. Fischer, Phy. Rev. Lett. **101** (26), 4 (2008).

[84]. A. Vansteenkiste, K. W. Chou, M. Weigand, M. Curcic, V. Sackmann, H. Stoll, T. Tyliszczak, G. Woltersdorf, C. H. Back, G. Schutz and B. Van Waeyenberge, Nat. Phys. **5** (5), 332-334 (2009).

[85]. P. A. Midgley and R. E. Dunin-Borkowski, Nat. Mater. **8** (4), 271-280 (2009).

[86]. A. H. Zewail, Philos T R Soc. A **363** (1827), 315-329 (2005).

[87]. J. S. Kim, T. LaGrange, B. W. Reed, M. L. Taheri, M. R. Armstrong, W. E. King, N. D. Browning and G. H. Campbell, Science **321** (5895), 1472-1475 (2008).

[88]. P. Schattschneider, S. Rubino, C. Hebert, J. Rusz, J. Kunes, P. Novak, E. Carlino, M. Fabrizioli, G. Panaccione and G. Rossi, Nature **441**, 486-488 (2006).

[89]. M. A. Schofield and Y. M. Zhu, Opt. Lett. **28** (14), 1194-1196 (2003).

Appendix A

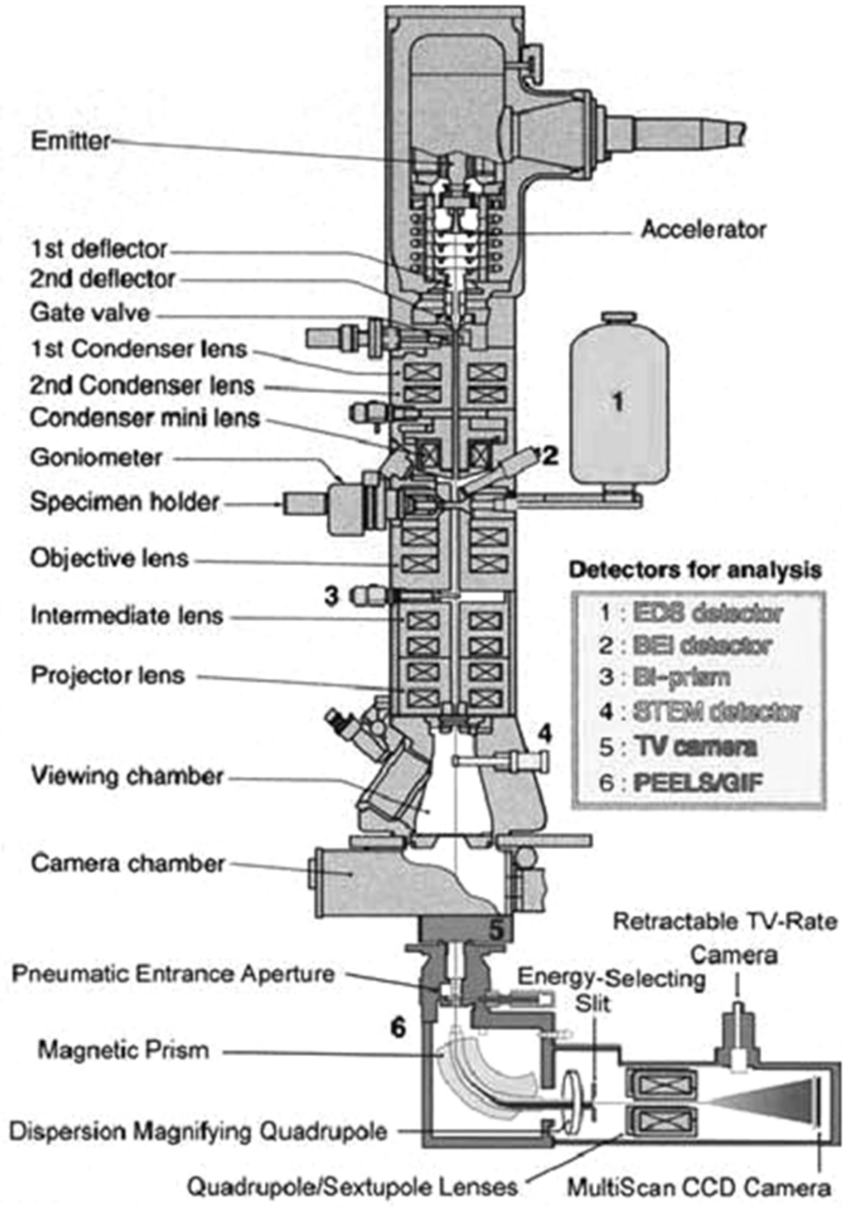

Figure A.0.1 Column diagram of JEOL 3000F

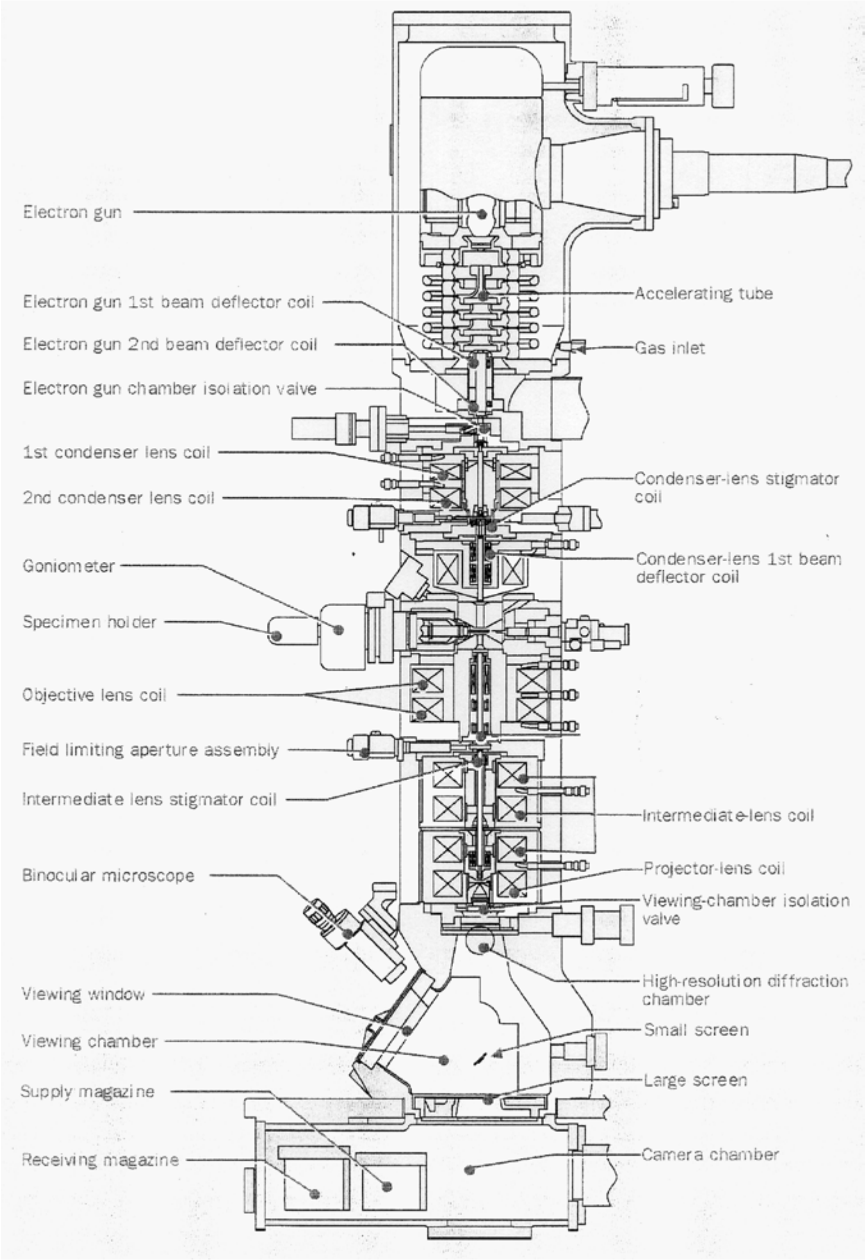

Figure A.0.2 Column diagram of JEOL 2100F-LM

Note that diagram is only for standard model of JEOL 2100F. For the instrument in Brookhaven, the objective lens pole pieces have been replaced to the special field-free Lorentz lens, as shown in Figure 2.3

Appendix B

Post Processing of Recorded Holograms

At each specified applied field in Figure 4.12 and Figure 4.14, holograms with the element in the field-of-view, and reference holograms under the same instrumental conditions without the element, were recorded. The electron-optical phase shift was reconstructed by Fourier-transform-based routines and subsequently unwrapped [89]. The electrostatic (mean inner potential, MIP) part of the unwrapped phase shift was subtracted through the following procedure: first, we saturated the sample at two opposite tilt directions; after alignment, the two reconstructed phase shift maps were averaged (thereby eliminating the mutual magnetostatic contributions) to obtain the MIP map [15]. The MIP was then subsequently subtracted from all measured phase shift maps at various fields. The remaining magnetic component of the phase shift is quantitatively proportional to the projected induction distribution. Amplifying the phase shift 4× and taking the cosine of the amplified phase provides a quantitative contour map showing the spatial distribution of the projected induction. Such contour maps are convenient to visualize the induction distribution especially by superimposing a weak mask function to highlight the specimen region [Figure B.0.1].

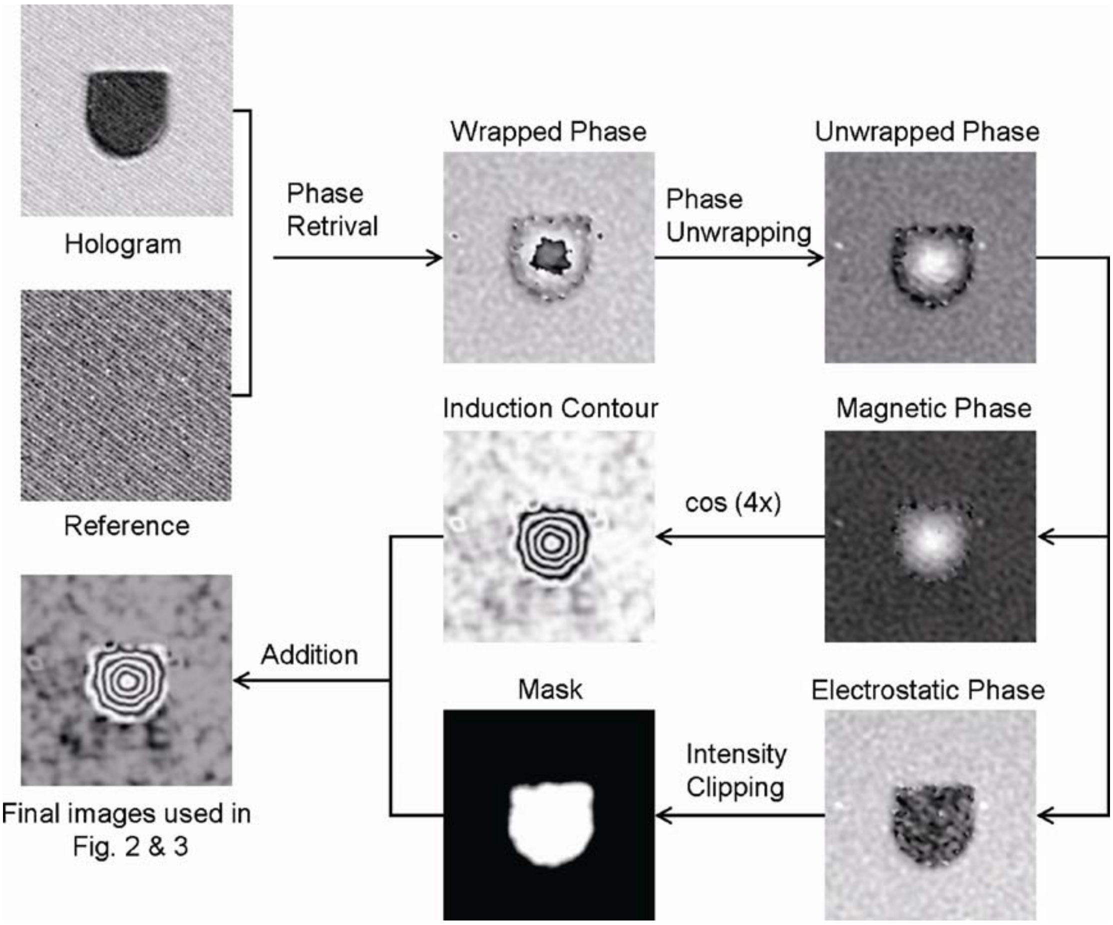

Figure B.0.1 Flow chart of post-processing of recorded images.

Appendix C

Design Drawings for *in-situ* TEM holder (unit: inch)

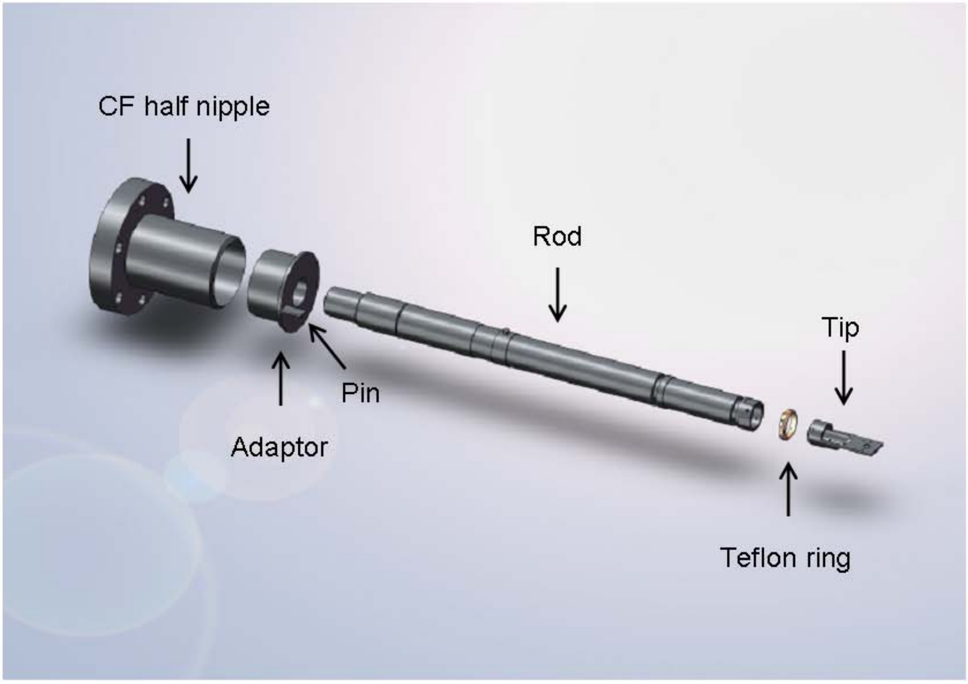

Figure C.0.1 Explosive chart of the holder assembly

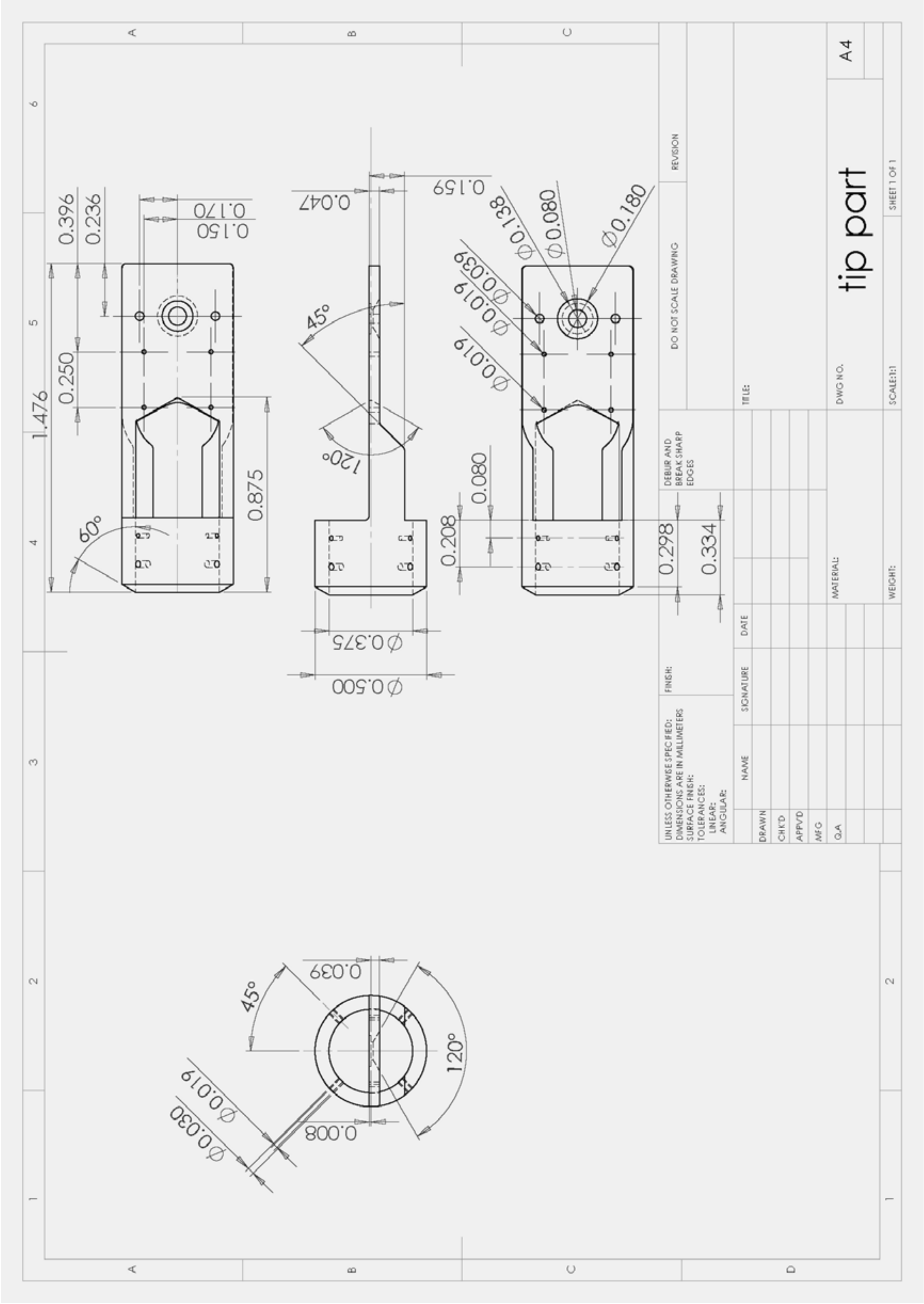
tip part
A4
DWG NO.
SCALE:1:1
SHEET 1 OF 1
TITLE:
MATERIAL:
WEIGHT:
DO NOT SCALE DRAWING
REVISION
DEBUR AND BREAK SHARP EDGES
FINISH:
UNLESS OTHERWISE SPECIFIED: DIMENSIONS ARE IN MILLIMETERS SURFACE FINISH: TOLERANCES: LINEAR: ANGULAR:
NAME
SIGNATURE
DATE
DRAWN
CHK'D
APPV'D
MFG
Q.A
0.396
0.236
0.170
0.150
1.476
0.250
0.875
60°
0.047
0.159
45°
120°
Ø0.375
Ø0.500
Ø0.138
Ø0.080
Ø0.180
Ø0.039
Ø0.019
Ø0.019
0.080
0.208
0.298
0.334
45°
0.039
120°
Ø0.019
Ø0.030
0.008
A
B
C
D
1
2
3
4
5
6

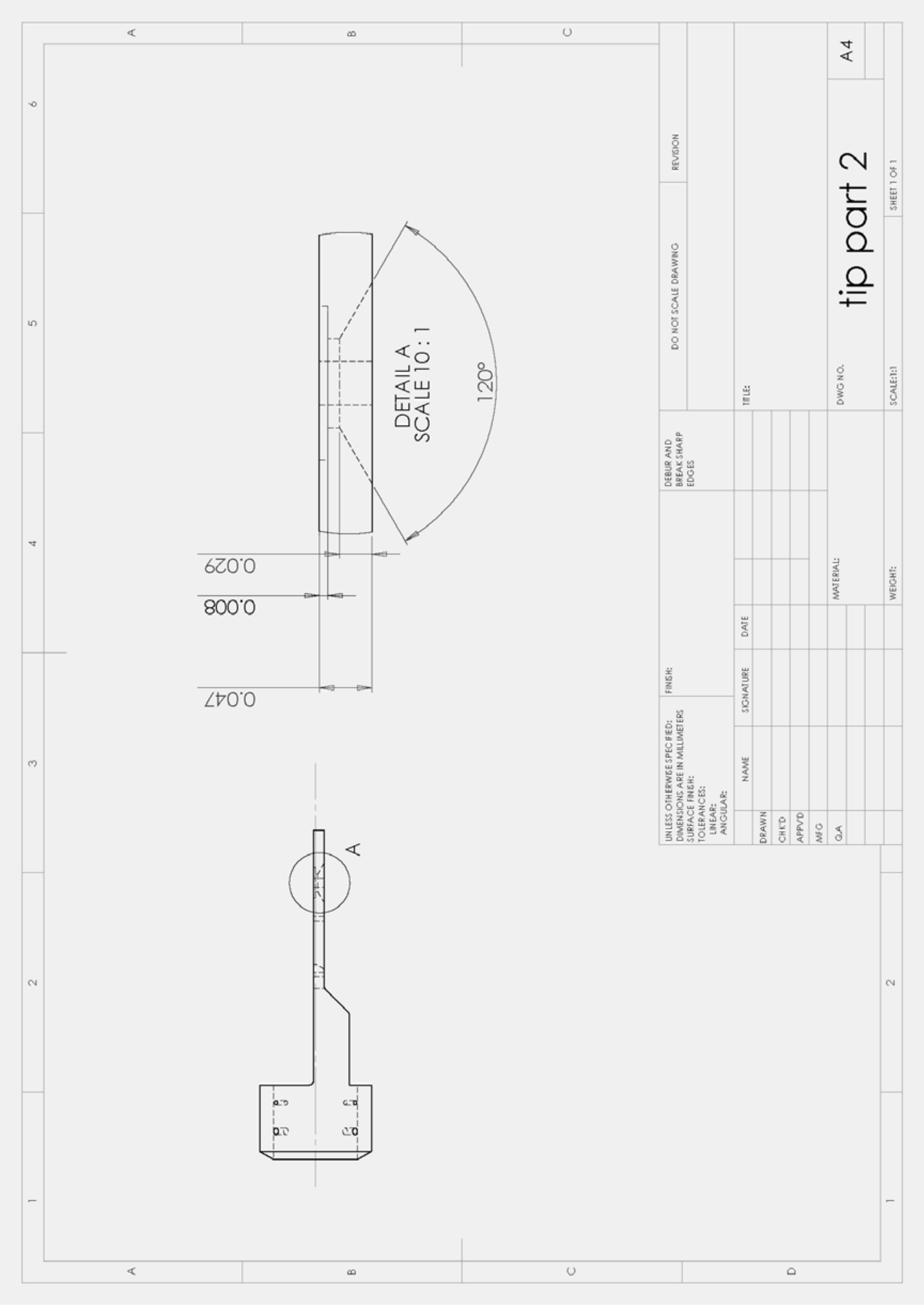
A
DETAIL A
SCALE 10 : 1
120°
0.029
0.008
0.047
UNLESS OTHERWISE SPECIFIED:
DIMENSIONS ARE IN MILLIMETERS
SURFACE FINISH:
TOLERANCES:
LINEAR:
ANGULAR:
FINISH:
DEBUR AND BREAK SHARP EDGES
DO NOT SCALE DRAWING
REVISION
NAME
SIGNATURE
DATE
DRAWN
CHK'D
APPV'D
MFG
Q.A
TITLE:
MATERIAL:
DWG NO.
tip part 2
A4
WEIGHT:
SCALE:1:1
SHEET 1 OF 1
1
2
3
4
5
6
A
B
C
D

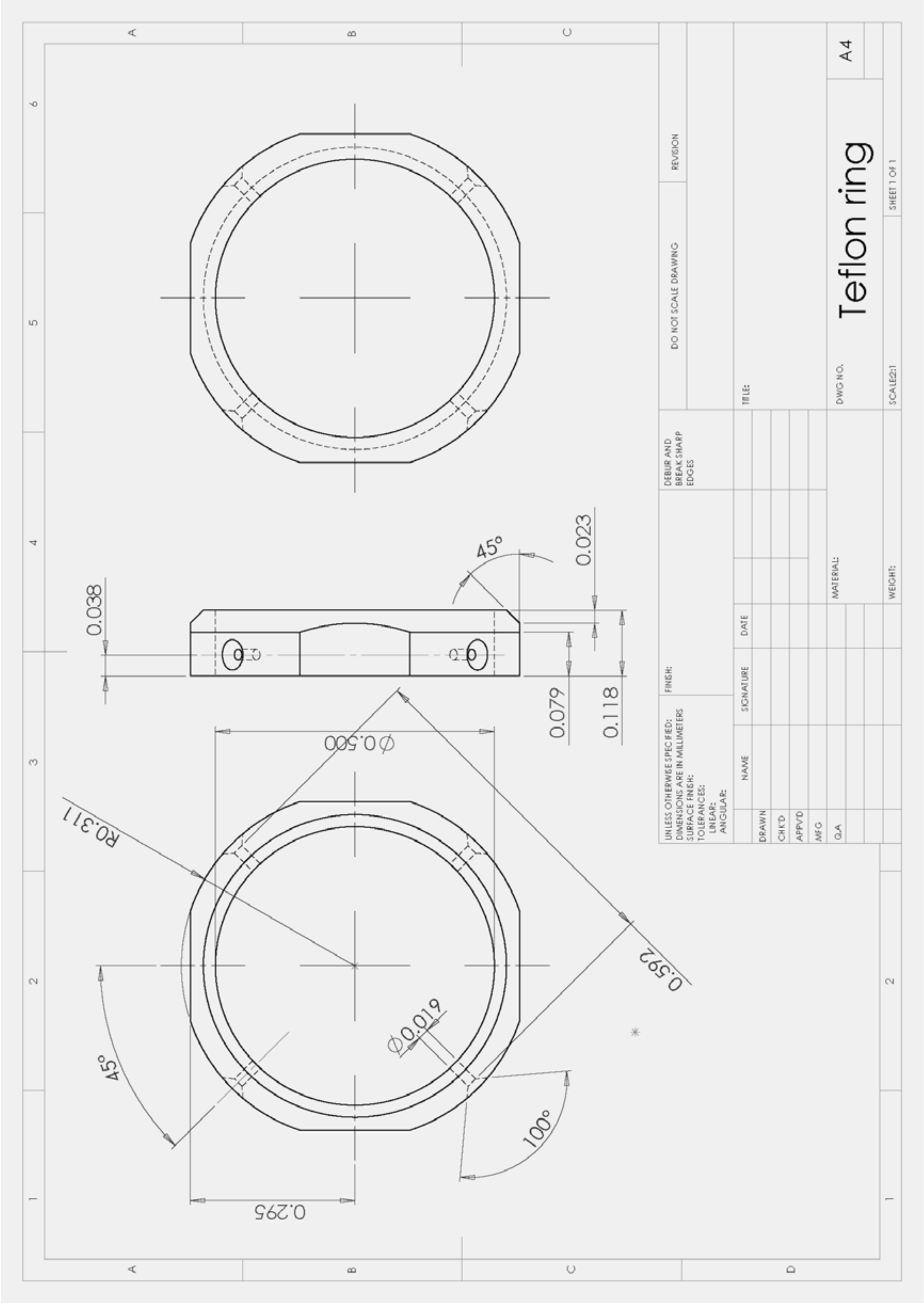
0.038
0.023
45°
0.079
0.118
Ø0.500
R0.311
0.592
Ø0.019
45°
100°
0.295
A
B
C
D
1
2
3
4
5
6
DO NOT SCALE DRAWING
REVISION
UNLESS OTHERWISE SPECIFIED:
DIMENSIONS ARE IN MILLIMETERS
SURFACE FINISH:
TOLERANCES:
LINEAR:
ANGULAR:
FINISH:
DEBUR AND BREAK SHARP EDGES
NAME
SIGNATURE
DATE
DRAWN
CHK'D
APPV'D
MFG
Q.A
TITLE:
MATERIAL:
DWG NO.
Teflon ring
A4
WEIGHT:
SCALE2:1
SHEET 1 OF 1

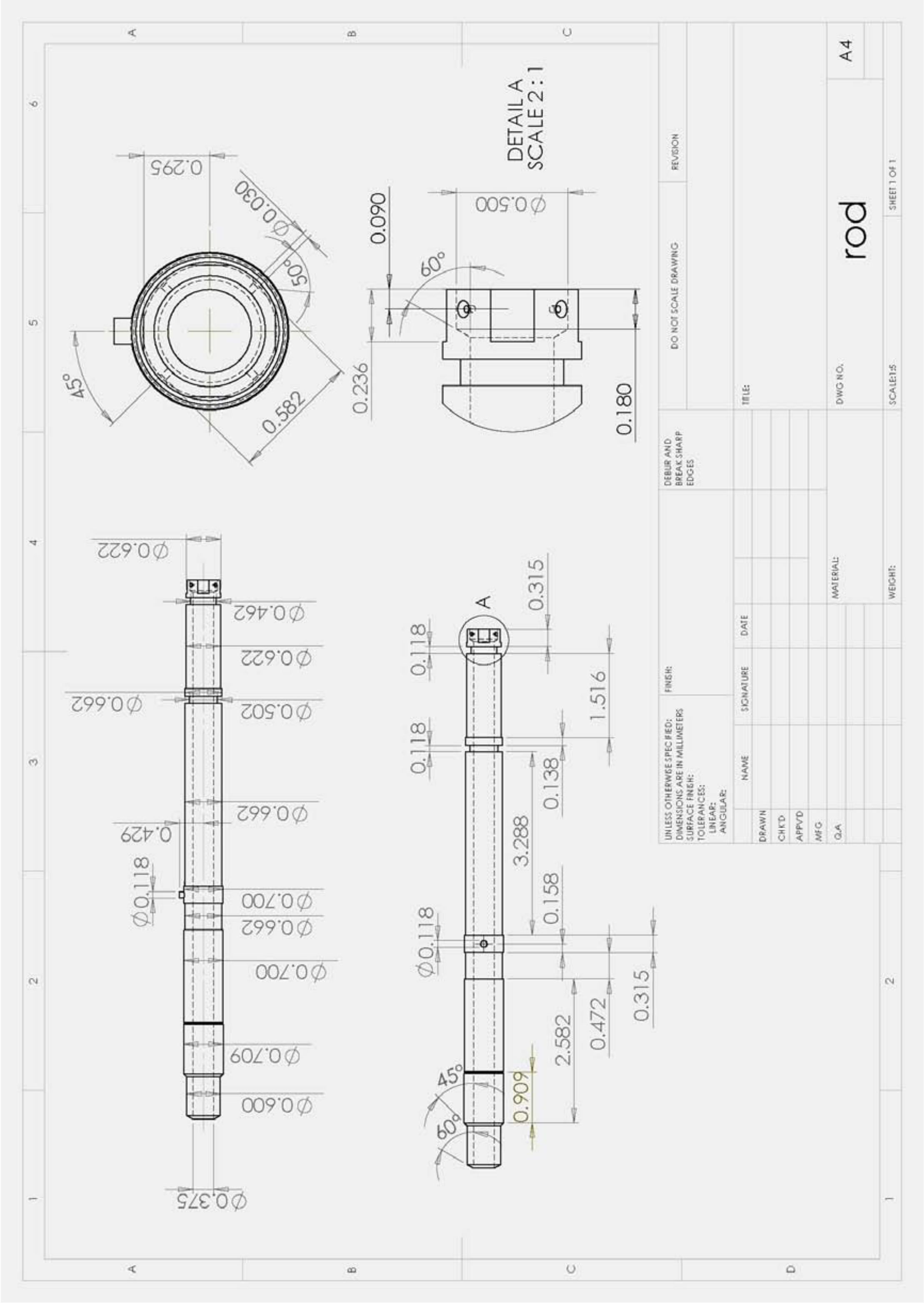
DETAIL A
SCALE 2 : 1
0.295
Ø0.030
50°
45°
0.582
0.090
60°
Ø0.500
0.236
0.180
Ø0.622
Ø0.462
Ø0.622
Ø0.662
Ø0.502
Ø0.662
0.429
Ø0.118
Ø0.700
Ø0.662
Ø0.700
Ø0.709
Ø0.600
Ø0.375
A
0.315
0.118
0.118
1.516
0.138
3.288
0.158
Ø0.118
0.315
0.472
2.582
0.909
45°
60°
DO NOT SCALE DRAWING
REVISION
UNLESS OTHERWISE SPECIFIED:
DIMENSIONS ARE IN MILLIMETERS
SURFACE FINISH:
TOLERANCES:
LINEAR:
ANGULAR:
FINISH:
DEBUR AND BREAK SHARP EDGES
NAME
SIGNATURE
DATE
DRAWN
CHK'D
APPV'D
MFG
Q.A
TITLE:
MATERIAL:
WEIGHT:
DWG NO.
rod
A4
SCALE:1:5
SHEET 1 OF 1

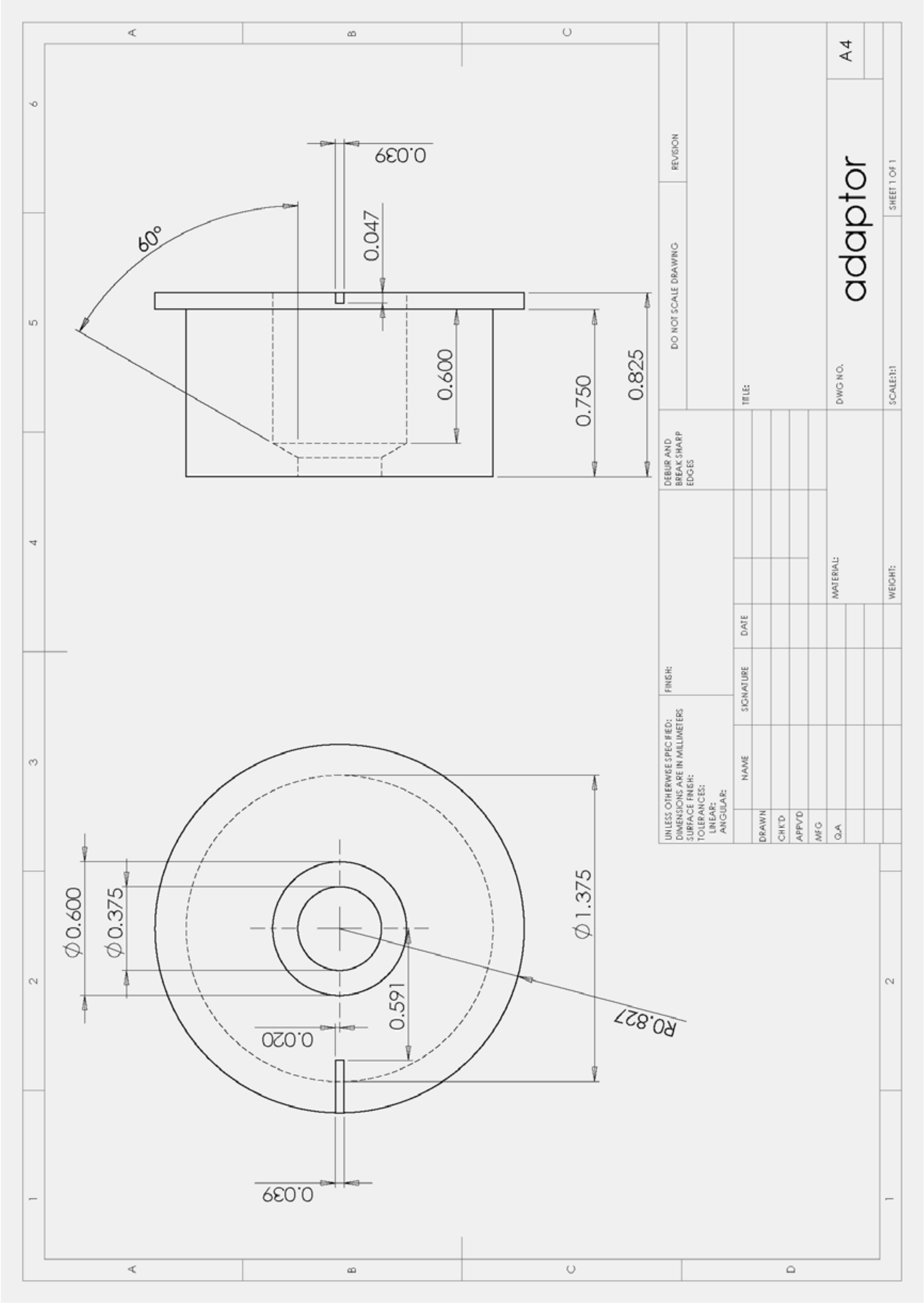
0.039
0.047
60°
0.600
0.750
0.825
Ø0.600
Ø0.375
Ø1.375
0.591
0.020
0.039
R0.827
UNLESS OTHERWISE SPECIFIED:
DIMENSIONS ARE IN MILLIMETERS
SURFACE FINISH:
TOLERANCES:
LINEAR:
ANGULAR:
FINISH:
DEBUR AND BREAK SHARP EDGES
DO NOT SCALE DRAWING
REVISION
NAME
SIGNATURE
DATE
DRAWN
CHK'D
APPV'D
MFG
Q.A
MATERIAL:
WEIGHT:
TITLE:
DWG NO.
SCALE:1:1
SHEET 1 OF 1
adaptor
A4
A
B
C
D
1
2
3
4
5
6

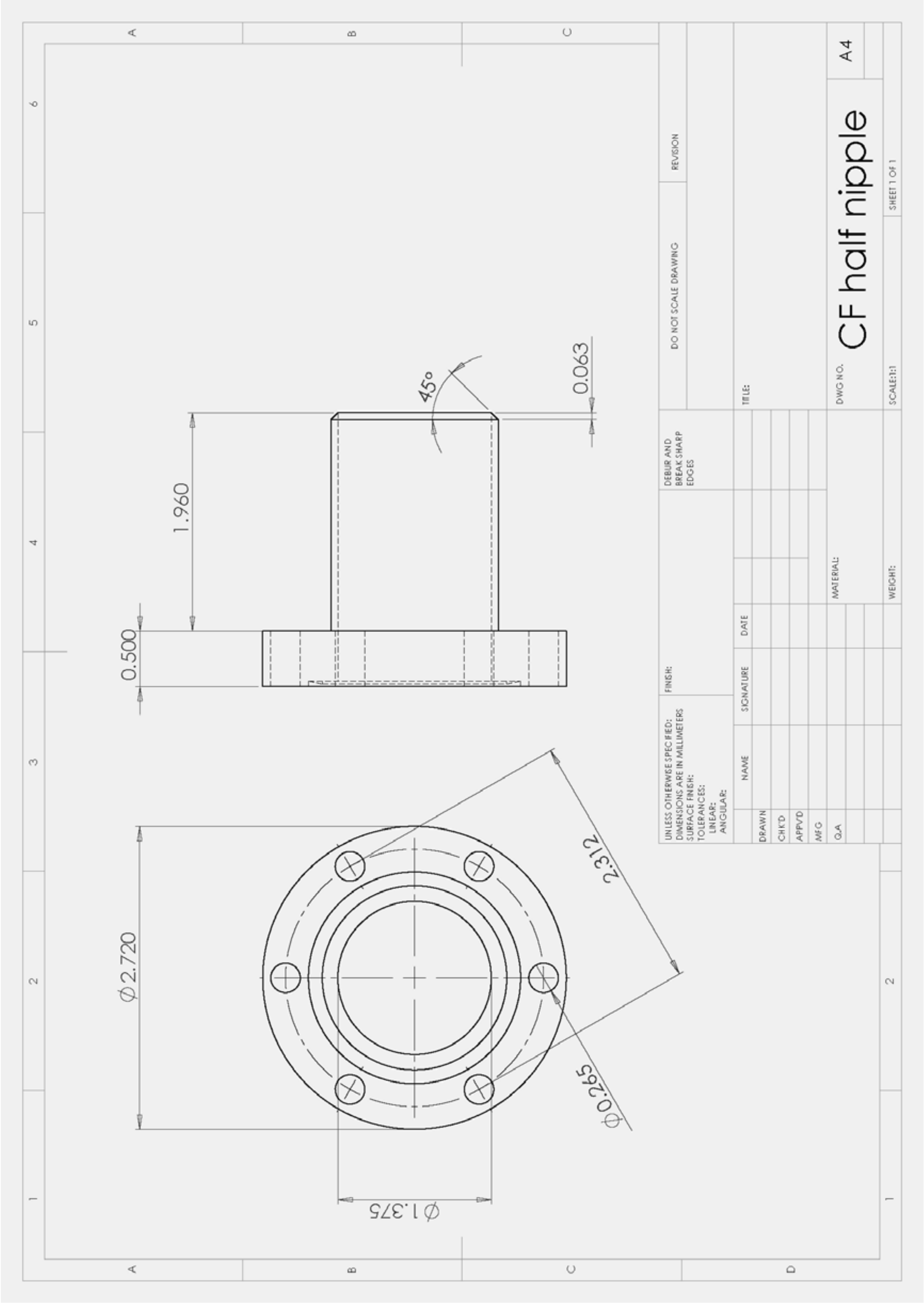
CF half nipple
A4
DO NOT SCALE DRAWING
REVISION
DEBUR AND BREAK SHARP EDGES
UNLESS OTHERWISE SPECIFIED:
DIMENSIONS ARE IN MILLIMETERS
SURFACE FINISH:
TOLERANCES:
LINEAR:
ANGULAR:
FINISH:
NAME
SIGNATURE
DATE
DRAWN
CHK'D
APPV'D
MFG
Q.A
TITLE:
MATERIAL:
DWG NO.
WEIGHT:
SCALE:1:1
SHEET 1 OF 1
1.960
0.500
45°
0.063
⌀2.720
⌀1.375
2.312
⌀0.265
A
B
C
D
1
2
3
4
5
6

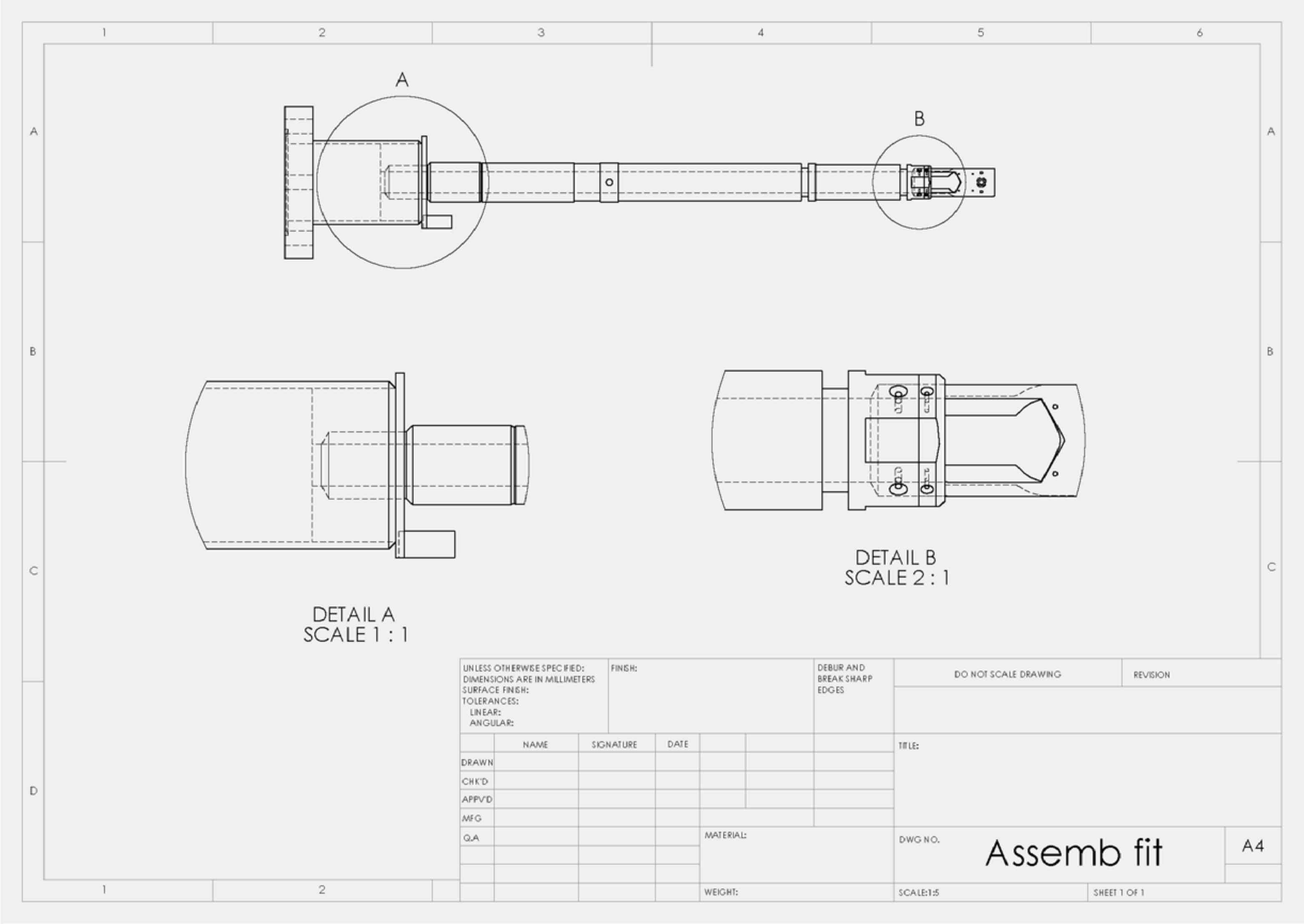
A
B
DETAIL A
SCALE 1 : 1
DETAIL B
SCALE 2 : 1
UNLESS OTHERWISE SPECIFIED:
DIMENSIONS ARE IN MILLIMETERS
SURFACE FINISH:
TOLERANCES:
LINEAR:
ANGULAR:
FINISH:
DEBUR AND BREAK SHARP EDGES
DO NOT SCALE DRAWING
REVISION
NAME
SIGNATURE
DATE
DRAWN
CHK'D
APPV'D
MFG
Q.A
MATERIAL:
WEIGHT:
TITLE:
DWG NO.
Assemb fit
A4
SCALE:1:5
SHEET 1 OF 1